TIME-RESOLVED STAGNATION TEMPERATURE AND PRESSURE MEASUREMENTS IN THE VORTEX STREET BEHIND A CYLINDER

by

Walid Chakroun

Thesis submitted to the Faculty of the Virginia Polytechnic Institute and State University in partial fulfillment of the requirements for the degree of

MASTER OF SCIENCE

in

Mechanical Engineering

APPROVED:

Dr. W. F. Ng, Chairman

Dr. H. L. Moses

Dr. J. R. Thomas

May 1987

Blacksburg, Virginia

TIME-RESOLVED STAGNATION TEMPERATURE AND PRESSURE MEASUREMENTS IN THE VORTEX STREET BEHIND A CYLINDER

by

Walid M. Chakroun

Committee Chairman: Dr. W. F. Ng
Mechanical Engineering

ABSTRACT

Recent theoretical and numerical investigations revealed the prospect that the instantaneous total temperature is nonuniform around vortices. For low Mach number flows, the instantaneous total pressure was also shown to become nonuniform in such a similar manner that the near-wake patterns of instantaneous total pressure exhibit almost exact facsimiles of these of total temperature. Here, the time-accurate measurements of the fluctuating total temperature and pressure are presented by placing an aspirating probe in the vortex street behind a cylinder. The data, obtained at a uniform upstream Mach number of 0.4 and with the vortex street in its natural (unexcited) state, show a significant fluctuation of total temperature and pressure. In addition, their time-traces taken in the near-wake are qualitatively similar.

TABLE OF CONTENTS

ACKNOWLEDGEMENTS

There are many people to thank for aiding me in the great amount of research and experimentation necessary in a project such as this. I wish to express my sincere appreciation and gratitude to the following for their unselfish time and patience:

Professor Wing-fai Ng of Virginia Polytechnic Institute and State University, who gave me both information and inspiration and played an invaluable role as my academic advisor. It is acknowledged that without his expertise on the subject, completion of this thesis would have been impossible;

Air Force Office of Scientific Research and Virginia Polytechnic Institute and State University, which supported me financially throughout my education;

Dr. M. Kurosaka and Mr. J. R. Goodman, who aided me tremendously during experimental research procedures at the University of Tennessee Space Institute;

Sarah Whitlock, who helped in repairing the hot wires and performing the probe calibration;

My parents, who by their unfaltering faith gave me the confidence and encouragement to continue my education and career,

And to my girlfriend, who gave me the time and endless love to achieve this work.

My brother, Hassan Chakroun, did not live to see the completion of this work and to his memory, I dedicate this work.

LIST OF FIGURES

LIST OF FIGURES (cont.)

LIST OF FIGURES (cont.)

LIST OF FIGURES (cont.)

LIST OF FIGURES (cont.)

LIST OF FIGURES

LIST OF TABLES

NOMENCLATURE

A_c	aspirating probe channel area at hot-wire plane
A^*	aspirating probe sonic throat area
a	hot-wire calibration constant
C_p	specific heat at constant pressure
D	cylinder diameter
d	hot-wire diameter
div	divergence
grad	gradient
k_w	hot-wire thermal conductivity at operating temperature
ℓ	hot-wire sensing length
M	Mach number
m	hot-wire calibration constant
Nu	Nusselt number
P	static pressure
Pr	Prandtl number
P_t	stagnation pressure
$P_{t\infty}$	mean free-stream stagnation temperature
Q_c	conductive heat loss at hot-wire ends
R	ideal gas constant
R_a	hot-wire room temperature resistance
Re	Reynolds number based on cylinder diameter
R_s	anemometer bridge resistance in series with hot-wire
R_w	hot-wire operating resistance
r	ratio of static to stagnation temperature

Re_d	Reynolds number based on hot-wire diameter
S	entropy
T	static temperature
t	time
T_t	stagnation temperature
$T_{t\infty}$	mean free-stream stagnation temperature
T_w	hot-wire operating temperature
U	velocity
U_∞	free-stream velocity
V	voltage

Greek Symbols

κ	fluid thermal conductivity
γ	ratio of specific heats
μ	fluid viscosity
ρ	fluid density
ϕ	dissipation function
λ	second coefficient of viscosity

1.0 INTRODUCTION

A recent investigation on some thermo-fluid phenomena of Karman vortex street has revealed hitherto unforeseen features of its temperature field: total (stagnation) temperature (T_t) becomes separated within and around a vortex, with higher T_t occupying a semi-circular, half region of the vortex, and lower T_t in the other half. Each vortex convected in the downstream direction carries within itself this thermally separated flow field. Both theoretical prediction and results of numerical simulation based on computational fluid dynamics calculations have produced the unmistakable presence of these thermal characteristics [1]. A recent experiment also demonstrates the existence of such a temperature field in which the vortex street shed from the circular cylinder is intensified by resonance of shedding frequency with acoustic wave standing in the cross-section of the wind tunnel [2]. This resonance amplifies the thermal separation in the flow field and gives a better signal to noise ratio in the measurements.

However, since both theoretical prediction and results of numerical simulation are based on the vortex street in its natural state, a follow-up experiment was conducted to measure the stagnation temperature and pressure fluctuation without acoustic resonance. The results of the experiment are documented in this report.

The present experiment has important implications in the following areas: Firstly, it validates the studies of separation of stagnation temperature within and around a vortex. Furthermore, as will be shown in chapter 6 (DISCUSSION OF THE RESULTS), for low subsonic Mach number

stagnation pressure (P_t) is predicted to become separated in a manner similar to T_t. Thus, the well-known defect of the time-averaged P_t behind a bluff body may be re-interpreted as the superposition of unsteadily separated structures [1]. Secondly, vortex shedding found in compressor and turbine blades may occur without acoustic resonance. The definitive identification of thermal separation without acoustic resonance is important in the context of the puzzling issue of over 100 percent efficiency found in advance fans, which originally motivated the investigation. Thirdly, recent theoretical and numerical studies [3] have shown the presence of time-averaged, localized negative entropy in the vortex street. The present experiment is an attempt to validate this conclusion. Finally, the measurements of stagnation temperature fluctuation with the vortex street in its natural state can provide valuable information for future experimental effort in mapping the detailed velocity field in the near wake of a circular cylinder at high speed.

The scope of this research, for ready comparison with theoretical and numerical results, includes conduction the experiment, reduction of the data, and presentation in terms of fluctuating stagnation pressure, stagnation temperature, and entropy. The corresponding frequency spectrum is also documented. No serious attempt has been made here for a back-to-back comparison of the experimental results with numerical studies. Detailed interpretation of the data in term of the fluid physics is not included either. Both of these are reserved for a further effort.

This report begins with an experimental background in chapter 2. Chapter 3 offers an explanation on the calibration of the aspirating probe and an error analysis of the experiment. A brief description of the experiment follows in chapter 4. The results are presented in chapter 5, followed by discussion of results in chapter 6. Chapter 7 gives a summary and conclusion of the overall effort.

2.0 EXPERIMENTAL BACKGROUND

In this chapter, two unique instruments used in the experiment will be described. The first instrument is a high-frequency aspirating probe for measuring fluctuating stagnation temperature and pressure. The other one is a high-frequency Kulite total pressure probe which gives an independent measurement of the stagnation pressure for comparison with the aspirating probe measurement. Following this, the test facility and data acquisition system will be described.

2.1 High-Frequency Aspirating Temperature and Pressure Probe

Because a conventional slow reponse probe such as a thermocouple cannot distinguish a rapid succession of high and low T_t flow, only the time-resolved measurement, using such advanced instruments as an aspirating probe, can detect its existence. This is the dual-wire aspirating probe shown in Fig. 1.

Conventional hot-wires measure the thermal energy lost by convection to the fluid. Thus, they are sensitive to the wire-fluid temperature difference ($T_w - rT_t$) and the mass flux (ρU) normal to the wire plane, where T_w is the wire temperature and is held constant, T_t the fluid stagnation temperature, r the ratio of static and stagnation temperature, ρ the fluid density, and U the fluid velocity. For a constant temperature hot-wire in a flow of uniform composition, the square of the anemometer bridge voltage (V) is proportional to the power dissipated to the fluid,

$$V^2 = f(\rho U)(T_w - rT_t) + Q_c \quad , \tag{2.1}$$

where Q_c is the conductive heat loss at the wire ends.

In an unsteady compressible flow field, all the flow quantities fluctuate temporarily. Thus, ρ, U, and T_t are all strong functions of time, making conventional hot wire data exceedingly difficult to interpret. To overcome this problem, two coplanar hot-wires operating at different temperatures are placed in the 1.5 mm (0.0595 inch) channel of the aspirating probe, the convergent exit of which is choked. The continuity equation can be written for one-dimensional channel flow as

$$\rho U = \left(\frac{P_t}{\sqrt{T_t}}\right) \sqrt{\frac{\gamma}{R}}\, M \left(1 + \frac{\gamma-1}{2} M^2\right)^{-\frac{\gamma+1}{2(\gamma-1)}} \quad , \tag{2.2}$$

where R is the gas constant, γ the ratio of specific heat, M the channel Mach number, T_t the stagnation temperature, and P_t the stagnation pressure. When the flow is sonic at the channel exit, Eq. (2.2) reduces to

$$(\rho U)^* = \left(\frac{P_t}{\sqrt{T_t}}\right) \sqrt{\frac{\gamma}{R}} \left(\frac{2}{\gamma+1}\right)^{\frac{\gamma+1}{2(\gamma-1)}} \quad , \tag{2.3}$$

where the asterisk refers to the condition at the sonic orifice. When the flow in the channel is one-dimensional, the mass flow at any axial station (ρUA) equals the mass flow at the choked orifice $(\rho UA)^*$. The mass flux at the wire plane can be written as

$$\rho U = \left(\frac{P_t}{\sqrt{T_t}} \right) \sqrt{\frac{\gamma}{R}} \quad \frac{A^*}{A_c} \left(\frac{2}{\gamma + 1} \right)^{\frac{\gamma+1}{2(\gamma-1)}} , \tag{2.4}$$

where A^* is the sonic area and A_c is the channel area at the wire plane. For a fixed geometry, A^*/A_c is constant, and for a gas of uniform composition, γ and R are constant, so that the channel mass flux (ρU) is only a function of free-stream stagnation temperature (T_t) and stagnation pressure (P_t). Equation (2.1) can now be written as

$$V^2 = f\left(P_t / \sqrt{T_t}\right)\left(T_w - rT_t\right) + Q_c \quad . \tag{2.5}$$

Equation (2.5) may be written in the more classical form for a constant temperature hot-wire

$$V^2 = \frac{\left(R_s + R_w\right)^2}{R_w} \quad \pi \, \ell \, \kappa \, Nu \, \left(T_w - rT_t\right) + Q_c \quad , \tag{2.6}$$

where R_s is the anemometer bridge resistance in series with the wire, R_w the hot-wire resistance at operating temperature (Fig. 2), κ the fluid thermal conductivity, Nu the Nusselt number and ℓ the wire length. The proper form of Nu as a function of Reynolds number has been of concern to many investigators. Here, the form

$$Nu = a(Re_d)^m \quad , \tag{2.7}$$

is used where Re_d is the Reynolds number based on the hot-wire diameter and a and m are empirically derived constants from calibration. By

substituting Eq. (2.7) into Eq. (2.6) and writing the Reynolds number $Re_d = (d/\mu)\rho U$ in terms of the compressible flow parameters of Eq. (2.4), we have

$$V^2 = \frac{(R_s+R_w)^2}{R_w}\,\pi\,\ell\,\kappa\,\left\{a\left[\frac{d}{\mu}\,\frac{P_t}{\sqrt{T_t}}\,\frac{A^*}{A_c}\sqrt{\frac{\gamma}{R}}\left(\frac{2}{\gamma+1}\right)^{\frac{\gamma+1}{2(\gamma-1)}}\right]^m\right\}$$

$$\times\,(T_w - rT_t) + Q_c\ , \tag{2.8}$$

where d is the wire diamter, μ the fluid viscosity, and A^*/A_c the ratio of sonic area to wire plane area. The conductive heat loss at the wire ends can be found by knowing the ratio of the conductive heat loss to the convective heat transfer to the fluid using

$$\left(\frac{d}{\ell}\right)\frac{1}{\sqrt{Nu}}\left(\frac{R_a}{R_w}\,\frac{k_w}{k}\right)^{1/2}\ , \tag{2.9}$$

where R_w/R_a is the overheat ratio, and k_w is the thermal conductivity of the wire [5].

Once the probe geometry and gas composition are fixed, the constants a and m can be determined by calibration. By operating the wires at different temperatures in separate anemometer circuits, two simultaneous voltage measurements are made from which the two unknowns P_t and T_t can be uniquely determined. Further detail on this will be given in Chapter 3.

This probe has an important advantage over conventional hot-wire measurements: the number of free-stream variables is reduced to only

two, stagnation temperature (T_t) and stagnation pressure (P_t). More detailed description of the aspirating probe can be found in Refs. [4] and [5].

2.2 High-Frequency Kulite Total Pressure Probe

As a consistency check on the aspirating probe performance, a 2.3-mm diam (0.093 inch) semiconductor pressure transducer (Kulite Model XCQ-093), incorporated into a conventional impact probe arrangement, was mounted adjacent to the aspirating probe. This provides a simultaneous measurement of the time-resolved total pressure for comparison with that from the aspirating probe. Although the diameter of the Kulite transducer is 2.3 mm (0.093 inch), the pressure sensing area is only 1.0 mm (0.038 inch) diameter. However, the smaller distance (0.51 mm) between the hot-wire sensors in the aspirating probe allows the aspirating probe to have better spatial resolution compared to the Kulite total pressure probe. Figure 3 shows a picture of the mounting arrangement for the combined probe.

2.3 Test Facility and Model

The test facility used in the experiment is the University of Tennessee Space Institute's high-speed, low-background-noise wind tunnel described in Ref. [1]. The facility is capable of supplying five lb/sec of air at ambient exit condition. The facility is also acoustically treated to reduce background noise level. As shown in Fig. 4, the interior of a settling tank, 0.508 m in diameter and 3.050 m in length, to which compressed air is introduced first, is covered with specially formed acoustic foams: starting from the inlet, the internal surface of acoustic foams is shaped as a diffuser. This provides an effective reduction of background noise to such an extent that in the test-section, the sound level at a free-stream Mach number in the test section of 0.5 is less than 100 db for frequency over 500 Hz. In addition to acoustic foams, three fine-meshed screens are installed in the settling tank to make the flow uniform.

The cross-section of the test-section is a square, 15.25 cm x 15.25 cm. The tunnel was originally designed so that the vortex street shed from the cylinder can be intensified by resonance of shedding frequency with acoustic wave standing in the cross-section of the wind tunnel [1]. Measurements were taken using the aspirating probe with the vortex street in the excited state. This work was reported in ref [2]. For the present investigation, it was decided to investigate the vortex street in its natural state without the acoustic enhancement of the tunnel. To accomplish this, one inch acoustic foams are added to the tunnel wall in the test-section. It was found that the foams are

sufficient to damp out the acoustic resonance. The cross-section of the modified test section remains as a square of 15.25 cm x 15.25 cm. Within the test section, the uniformity of velocity and temperature profiles outside the boundary layers is confirmed. Aft of the test section, the air is discharged directly to the atmosphere.

The time-averaged total temperature is monitored by a thermocouple installed within the settling tank, the free-stream Mach number by a calibrated total and static pressure probe inserted in the test section and located upstream of the cylinder at X/D = -5.75.

The test model is a cylinder of 2.54 cm in diameter (D) and 15.24 cm in its effective length. The cylinder is made of Polyvinyl Chloride (PVC), a thermally insulating material. The origin of the x-coordinate, aligned along the free-stream direction, is located at the center of the cylinder, the y- and z-coordinates, being, as shown in Fig. 4, perpendicular and parallel to the cylinder, respectively.

2.4 Data Acquisition and Processing

The data acquisition system used in the experiment coupled accurate channel-to-channel time synchronization with low system noise. A schematic of the data acquisition system is shown in Fig. 5. Three channels of 1200 data points were taken simultaneously. Two channels were used for the voltage of each hot-wire and one for the voltage from the Kulite pressure transducer. A LeCroy 8210 10-bit digitizer sampled the data at a rate set by a seven speed clock. The resolution of the A/D is 10 mv/count. The data were sampled at 25 kHz with a frequency

cutoff filter at 12 kHz. From the digitizer, the signals passed through a LeCroy, 8910A CAMAC to GPIB interface and were stored in LeCroy 8800 Memory modules. Directed by LeCroy CATALYST software, the data were transferred from the memory modules onto an IBM PC diskette automatically.

On the flexible disks, the signals were encoded in unformatted binary code in a serial fashion. A series of steps were needed to transfer the data from the diskette up to the IBM 3090 mainframe computer. To put the data in a usable format, the LeCroy program, which was written in FORTRAN, converts the binary code into the corresponding voltages. The output of the program is a file containing the relative time that the data were taken (seconds) and the corresponding voltages on the three channels. The file is immediately written on a blank flexible diskette for storage. The data were then uploaded from the PC to the mainframe where all the data reduction was done.

3.0 CALIBRATION AND ERROR ANALYSIS

According to Eq. (2.8) the aspirating probe responds to stagnation temperature and pressure fluctuations and it is not otherwise affected by gas velocity. To be able to retrieve an accurate dc level of the measurements, steady-state calibrations of the dual hot-wire aspirating probe were performed before and after each run. This brackets the dc shift due to aging and drifting of the hot-wire sensor during the experiment.

In a prior stage of the experiment, steady-state calibration of the aspirating probe was accomplished using a small, portable pressure vessel: 0.23 m diam x 0.30 m (9 in diam x 12 in). The probe was mounted inside the vessel and pressure change was achieved using suction from a vacuum pump and high pressure shop air. Temperature change was accomplished by immersing the apparatus in a water bath. The temperature range covered was from 10 C to 32 C (50 F to 90 F) whereas the pressure range was from 0.67 atm to 1.33 atm. However, it was found that a drift in the wire's resistance occurred when the probe was moved from the tunnel to the vessel. To prevent this problem, the entire tunnel was then used as a pressure vessel for on-site calibration of the probe. The pressure in the tunnel could be increased from 1 atm to 1.2 atm. The calibration of the probe was accomplished by varying the stagnation pressure at constant room temperature, since it was noticed that small variations in temperature have no effect on the calibration constants.

A functional relationship of the form of Eq. (2.8) can be fitted to the measured voltage versus pressure, and the empirical constants a and m can be derived. A least-square fit method was used to minimize the error between the correlation Eq. (2.8) and the calibration data. Figure 6 is a typical single hot-wire calibration of the aspirating probe.

The two platinum-coated tungsten wires mounted on the probe were of 3.8 and 8.9 μm-diameter, operating at a constant temperature of 475 K and 404 K, respectively. The calibration of the two wires can be combined to yield the overall probe response as a function of the anemometer bridge voltage for the two wires (Fig. 7).

After finding the calibration constants a and m for both wires, the correlation of Eq. (2.8) can be used to solve two equations for the two unknowns P_t and T_t. Utilizing the correlation should prove more accurate than interpolation or any curve fitting technique.

The temperature and pressure sensitivities of the aspirating probe are set by the difference in temperature of the two wires, but the resolution is limited by the system noise. This noise is about 4 mv peak-to-peak based on the hot-wire anemometer noise level with suction applied to the aspirating probe. The noise level is consistent with the resolution of the data acquisition system. An error analysis of the probe correlation Eq. (2.8) showed that a 4 mv uncertainty on each wire yields a 0.5 K uncertainty in gas stagnation temperature and 0.7 Kpa uncertainty in stagnation pressure. Based on the tunnel operating condition, this corresponds to uncertainties of 0.25 percent for stagnation temperature and 0.5 percent for stagnation pressure.

4.0 DESCRIPTION OF THE EXPERIMENT

The experiment conducted at the University of Tennessee Space Institute can be divided into two parts. In the first part, the flow upstream of the cylinder was uniform. Measurements were taken downstream from the cylinder at different X/D and Y/D, where X is the horizontal distance measured from the centerline of the cylinder to the probe tip, Y is the vertical distance between the cylinder and the probe tip, and D is the diameter of the cylinder (2.54 cm). Z/D is kept at a constant of 0.0, corresponding to the midspan of the cylinder. These measurements were taken at a free-stream Mach number of 0.4. Reynolds number based on the cylinder diameter is 234000. Using a Strouhal number of 0.2, the calculated vortex shedding frequency is at 1080 Hz. Table 1 summarizes the data taken during this part of the experiment.

In the second part of the experiment, attempting to search for the time-averaged, localized negative entropy, a shear flow was created upstream of the cylinder. It is believed that this will enhance the signal due to spanwise transport of fluid in the wake of the cylinder [6]. The variation in flow field velocity is linear across the span of the cylinder as shown in Fig. 8. This profile is maintained in the y-direction of the tunnel. The shear flow was created by placing upstream of the cylinder a screen composed of grid rods unevenly spaced. Two "washers" were located at the ends of the cylinder to eliminate the effect of the endwall boundary layers. The free-stream Mach number upstream of the screen was 0.6. Measurements were taken at different X/D and Z/D, where Z is the longitudinal distance measured along the

centerline of the cylinder. For all measurements in this part of the experiment, Y/D is held constant at 0.0. Table 2 summarizes the data taken during the second part of the experiment.

In addition, data were taken upstream of the cylinder, where the Karman vortex street does not exist. In this region the ac fluctuations, as expected, were very small due only to the noise level in the tunnel. The measured free-stream turbulence intensity in the tunnel upstream of the cylinder in terms of RMS fluctuations is 0.6 K in stagnation temperature and 1.0 Kpa in stagnation pressure. Furthermore, as expected, the dc components of the measured P_t and T_t from the aspirating probe agree very well with other steady-state conventional instruments placed upstream of the cylinder. Measuring the data upstream was only a consistency check of the equipment.

5. EXPERIMENTAL RESULTS

In this chapter, the reduced data of the experiment are presented. The comparison between measured stagnation pressures from the aspirating probe and the Kulite total pressure probe will be given first, followed by a presentation of the stagnation temperature, stagnation pressure and entropy. The corresponding frequency spectrum is also documented. For convenience, the presentation of data is divided into two parts: uniform flow and shear flow, as described in the previous chapter. Detailed discussion of the results will not be given here, but will be presented in the next chapter.

5.1 Comparison of the Kulite Total Pressure Probe and Aspirating Probe

As mentioned previously, the mounting arrangement of the Kulite total pressure probe and aspirating probe allows a comparison to be made of the measured stagnation pressure from the two probes. The limitation of the Kulite probe is that it is more sensitive to free-stream flow angle fluctuation than the aspirating probe. The comparison of the sensitivities of the two probes to flow angle change was obtained by testing the probe in a 2.54 cm (1 inch) free-jet at a Mach number of 0.4. By changing the orientation of the probe relative to the free-jet, the change in the output voltages from the probe was recorded at different angular settings. The corresponding changes in stagnation pressure were then calculated. It was concluded that, when the angle of

flow increased from 0 to 45, the reading of the Kulite total pressure probe became increasingly less than the actual free-stream stagnation pressure, whereas the reading of the aspirating probe did not change significantly. Because flow angle fluctuation of 45 degrees is expected in the near wake of the cylinder, the stagnation pressure measured from the Kulite total pressure probe will be less than that from the aspirating probe.

A detailed comparison between the measurements using the Kulite total pressure probe and aspirating probe is given in Ref. [2] and it will not be repeated here.

In summary, from Ref.[2] it was found that the measured stagnation pressures from the aspirating probe and Kulite total pressure probe compared very well, except in regions where the large flow angle fluctuation was expected. This is an important conclusion since the design of the two probes is based on completely different principles: The Kulite total pressure probe used a semi-conductor strain-gage pressure transducer, whereas the aspirating probe is a dual hot-wire sensor operated with a choked orifice downstream. Because of the sensitivity of the Kulite total pressure probe to flow angle fluctuations, it was not a suitable instrument to be used in the near wake of the cylinder.

For the present experiment, comparison between the two probes will only be given at X/D = 4 and Y/D = 1.5 location. The data compared were taken from the case with uniform upstream condition in the tunnel. The result is presented in Figs. 9a,b,c. In Fig. 9a, the measured

stagnation pressures from the Kulite total pressure probe and aspirating probe are plotted against time. The same data are plotted on Fig. 9b on an expanded time-scale with the two traces on top of each other. The corresponding comparison of the frequency spectra is shown in Fig. 9c. Figures 9a,b,c show compatibility agreement between the two instruments. At X/D = 4 and Y/D = 1.5, the probes are in the wake of the cylinder and are subjected to flow angle variation from the vortex. This may account for some of the discrepancies between the measurements. Since the Kulite total pressure probe is not a suitable instrument for this experiment and is mainly used as a consistency check for the aspirating probe, the data from the Kulite total pressure probe will not be discussed further.

5.2 Time-Resolved Data in the Wake of the Cylinder

In this section, the complete set of data taken during the experiment is presented. The results from the uniform flow will be given first, followed by the results from the shear flow. In each part, the dc components of the data will be summarized in a composite figure, and then the individual time-resolved data for different locations in the wake of the cylinder will be given. Finally, the time-resolved data will be summarized and presented in terms of their root-mean-square (RMS) values.

5.2.1 Uniform Flow

As mentioned earlier, steady-state calibration was performed before

and after each run to retrieve an accurate dc level of the measurements. In Fig. 10, the dc values for the nondimensionalized total pressure $\left(\frac{P_t}{P_{t\infty}}\right)$, total temperature $\left(\frac{T_t}{T_{t\infty}}\right)$, and entropy $(\Delta S/C_p)$ were plotted versus Y/D at X/D = 2 and 4 for the case of uniform upstream flow. The values are based on the average of the calibration before and after each run with an uncertainty band marked on the plot. The uncertainty band is based on the difference between the values calculated using the calibration before and after each run. Although measurements were also taken at X/D = 1, excessive hot-wire breakage prevented the after-test calibration. Therefore the dc component at X/D = 1 is not presented in Fig. 10.

The nondimensionalized entropy is not a direct measurement, but is calculated from the measured stagnation temperature and stagnation pressure using the following relation:

$$\frac{\Delta S}{C_p} = \frac{S_2 - S_1}{C_p} = \ln\left(\frac{T_{t2}}{T_{t1}}\right) - \frac{\gamma-1}{\gamma} \ln\left(\frac{P_{t2}}{P_{t1}}\right) \quad , \tag{5.1}$$

where subscripts 1 and 2 denote the upstream and downstream stations from the cylinder, respectively. The dc component of the entropy is obtained by time-averaging the instantaneous entropy, which itself is calculated from the time-resolved measurements of the stagnation temperature and pressure. It can be seen from Eq. (5.1) that the calculated entropy is the difference between two small numbers, and it is very difficult to achieve a high level of accuracy in the calculated entropy.

The plot shows a similarity between the total temperature and pressure curves. This observation will be elaborated further in the next chapter. Notice that the existence of the negative entropy in the vortex street can not be validated from Fig. 10 due to the large uncertainty band.

Figures 11 through 20 represent the reduced data for the fluctuating ac component in terms of stagnation pressure ratio $(\frac{P_t}{P_{t\infty}})$, stagnation temperature ratio $(\frac{T_t}{T_{t\infty}})$, nondimensionalized entropy $(\frac{\Delta S}{C_p})$, and the corresponding frequency spectrum. In Figs. 11a through 20a, the entire data set of 1200 points is presented. Figures 11b through 20b are a segment of the same data plotted on an expanded time scale. Figures 11c through 20c are the corresponding frequency spectra. All figures have the same axis and so it is easy to make comparisons.

Figures 11 through 13 are the data at X/D = 1. This is the closest X/D station to the cylinder. Data are presented for three different Y/D stations 0.0 (center of the cylinder), 0.25 and 0.5 (edge of the cylinder).

Figures 11b through 13b show the same data on an expanded time scale. It can be seen that the fluctuations in stagnation temperature and pressure have similar shapes and the positions of large T_t correspond to large P_t and small T_t to small P_t. The significance of this will be discussed in the next chapter.

Figures 17 through 20 are the data at X/D = 4, which is the station farthest downstream. Data were taken at four stations ranging from Y/D

= 0.0 to 1.5. There is a small reduction in the amplitudes of the fluctuating stagnation temperature and pressure compared to the corresponding Y/D station at X/D = 1.

Data were also taken at X/D = 2 and are presented in Figs. 14 through 16. They correspond to Y/D stations of 0.0, 0.25, and 0.5. Since it is believed that the vortex is more developed at this location, it can be observed that the corresponding fluctuation in stagnation temperature and pressure become larger than that at X/D = 1 and X/D = 4. The frequency spectra of Figs. 14c through 16c clearly show the vortex shedding frequency at 1080 Hz which agrees with the calculated shedding frequency based on a Strouhal number of 0.2.

The results of Figs. 11 through 20 are summarized in Fig. 21 which represents the plot for the root-mean-square (RMS) values of the stagnation pressure, stagnation temperature and nondimensionalized entropy $(\frac{\Delta S}{C_p})$ at each station. As noticed earlier, at X/D = 2 the RMS magnitude of the stagnation temperature and pressure is larger than that at X/D = 1 and 4. It is believed that at X/D = 1 the vortex is not as well developed as that at X/D = 2, and it has diminished at X/D = 4.

5.2.2 Shear Flow

For the shear flow, data are only taken at X/D = 1 and 4. In Fig. 22 the dc values for the total pressure $(\frac{P_t}{P_{t\infty}})$, total temperature $(\frac{T_t}{T_{t\infty}})$ and nondimensionalized entropy $(\frac{\Delta S}{C_p})$ were plotted versus Z/D at X/D = 1 and 4. Again, because of a large uncertainty band in the calculated entropy, Fig. 22 can not be used to validate the existence of

localized time-averaged negative entropy. It is also possible that the presence of the "washer" at the end of the cylinder (Fig. 8) changes the flowfield to the extent that the time-averaged negative entropy is not found. Further work is needed in order to detect the presence of localized negative entropy in the wake of the cylinder.

Figures 23 through 28 represent the ac fluctuations for the stagnation pressure $(\frac{P_t}{P_{t\infty}})$, stagnation temperature $(\frac{T_t}{T_{t\infty}})$, and non-dimensionalized entropy $(\frac{\Delta S}{C_p})$ at X/D = 1 and 4. At each X/D station, data corresponding to Z/D stations of -2, 0, 2 are presented. The amplitudes of the fluctuating stagnation temperature and pressure at X/D = 1 are greater than the corresponding Z/D station at X/D = 4. Figures 23c through 28c are the corresponding frequency spectrum.

The results of Figs. 23 to 28 are summarized in Fig. 29, which represents the plot for the root-mean-square (RMS) values of the stagnation pressure, stagnation temperature and nondimensionalized entropy $(\frac{\Delta S}{C_p})$ at each station.

6.0 DISCUSSION OF THE RESULTS

The results of the reduced data show a correlation between the stagnation temperature and pressure. In the ac and dc plots, the stagnation temperature and pressure have almost a similar shape and the position of large T_t correspond to large P_t and small T_t to small P_t.

For completeness, the mechanism of dynamic separation of total pressure around vortices presented in Ref. [1] are reproduced here. According to Ref. [1], central to the dynamic interpretation of the correlation between the stagnation temperature and pressure is the following form of the energy equation,

$$C_p \frac{DT_t}{Dt} = \frac{1}{\rho} \frac{\partial p}{\partial t} \quad , \tag{6.1}$$

where DT_t/Dt is the substantial derivative of stagnation temperature, C_p is the specific heat at constant pressure, ρ is the fluid density, and all other notation is standard. Equation (6.1) is an approximate equation, where the flow is assumed to be inviscid and also adiabatic. The exact counterpart of the equation could be written in the following non-dimensional form:

$$\frac{DT_t^*}{Dt^*} = \frac{1}{\rho^*} \frac{\partial P^*}{\partial t^*} + \frac{1}{Re} \left(\frac{\tau\ U_\infty}{D}\right) \left[\phi^* + \frac{1}{Pr} \nabla^{*2} T^* + \vec{U}^* \cdot \vec{F}_f^{\,*}\right] \quad ,$$

where Pr is the Prandtl number, Re the Reynolds number based on the diameter of the cylinder and starred quantities denote their dimensionless values; T_t and T are nondimensionalized by U_∞^2/C_p, P

by ρU_∞^2, ρ by ρ_∞, t by τ, which is a characteristic time-scale, the time required for a fluid particle to travel across one full wavelength for a trochoidal pathline or to traverse the wake for a cross-over pathline [1]. The first term inside the square bracket (ϕ) is the dissipation function, and is nondimensionalized by $\mu U_\infty^2/D^2$. $\vec{F}_f$ is a stress tensor and is equal to div[μ(def $\vec{u}$)] + grad (λ div $\vec{u}$), where def is the deformation tensor, λ, the second coefficient of viscosity. $\vec{F}_f$ is nondimensionalized by $\mu U_\infty/D^2$.

The time-scale, τ, is of the order of the vortex shedding period and an estimate yields $\tau U_\infty/D \sim 5$; thus for a flow with a large Reynolds number, the center of interest, the second term may be discarded. As far as the dynamics of instantaneous change in total temperature is concerned, dissipative effects are then of negligible importance. (However, they of course exert a cumulatively decided effect upon the far downstream T_t.)

For an incompressible flow, under the same condition where Eq. (6.1) holds, the internal energy does not vary along pathlines. Then Eq. (6.1) is reduced to

$$\frac{DP_t}{Dt} = \frac{\partial P}{\partial t} \quad , \tag{6.2}$$

where P_t is the total pressure. Combining Eq. (6.1) and (6.2) we get

$$\rho C_p \frac{DT_t}{Dt} = \frac{DP_t}{Dt} \quad . \tag{6.3}$$

For flows at low Mach number, such as in the wake of the cylinder, the instantaneous measurements should show that the position of high T_t correspond to high P_t, low T_t to low P_t. In fact by integrating Eq. (6.3) along a pathline starting from far upstream, we obtain

$$\frac{\rho C_p T_{t\infty}}{P_{t\infty}} \left(\frac{T_t}{T_{t\infty}} - 1\right) = \frac{P_t}{P_{t\infty}} - 1 \quad . \tag{6.4}$$

Thus in the near wake the pattern of the instantaneous distribution of $P_t/P_{t\infty}$ must be almost a facsimile of those of $T_t/T_{t\infty}$ (except for a scaling factor of $\rho C_p T_{t\infty}/P_{t\infty}$, which is equal to $(\gamma/(\gamma-1))$. Further detail of the derivation presented here is given in Ref. [1].

Figures 30 through 36 show comparison between the stagnation temperature $\left(\frac{T_t}{T_{t\infty}}\right)$ as measured in the experiment for the uniform flow and the stagnation temperature as inferred using Eq. (6.4) and the measured $(P_t/P_{t\infty})$. Comparisons were given at X/D = 2 and 4, and for different Y/D locations.

At all locations, these figures indeed confirm the correlation between the stagnation temperature and pressure and prove that the separation of total temperature leads to similar separation of total pressure in the near wake of the cylinder. The difference in the measured temperature and inferred temperature may be due to viscous effect, which is not accounted for in Eq. (6.4).

It is worth mentioning that Eq. (6.4) is the limiting case of the isentropic relation

$$\left(\frac{T_t}{T_{t\infty}}\right)^{\frac{\gamma}{\gamma-1}} = \frac{P_t}{P_{t\infty}} \,. \tag{6.5}$$

By assuming incompressible flow, Eq. (6.5) can be shown to reduce to Eq. (6.4).

7.0 SUMMARY AND CONCLUSION

An experiment was conducted using an aspirating probe to measure the fluctuating stagnation temperature and pressure in the vortex street shed from a cylinder in its natural state. The tests were run in a high-speed, low-background-noise wind tunnel. The first part of the experiment was performed with a uniform upstream flow at a free-stream Mach number of 0.4. A shear flow with a linear velocity profile along the span of the cylinder was created for the second part of the experiment.

Three conclusions can be drawn from this experiment:

First, the experiment demonstrates the existence of a temperature field in the wake of the cylinder where a significant stagnation temperature fluctuation is observed. This validates the recent theoretical and numerical investigations on the separation of the instantaneous total temperature around the vortices.

Secondly, the data from the time-resolved measurement appear to confirm the spatial separation of and the correlation between the stagnation temperature and the stagnation pressure. These data confirm that the ac and dc components of the total pressure and total temperature have an almost similar shape and the position of high T_t corresponds to high P_t and low T_t to low P_t.

Finally, the calculated entropy using the measured stagnation temperature and pressure has a large uncertainty band, and the existence of the time-averaged negative entropy for both the uniform flow and the shear flow can not be validated from this set of measurements.

REFERENCES

1. Kurosaka, M., Gertz, J. B., Graham, J. E., Goodman, J. R., Sundaram, P., Riner, W. C., and Kuroda, H., "Energy Separation in a Vortex Street," accepted for publication in Journal of Fluid Mechanics.

2. Watts, M. E., Ng, W. F., and Kurosaka, M., "Time-Resolved Stagnation Temperature and Pressure Measurements in the Vortex Street Behind a Cylinder," Interim Report 85-147-05 #1, Virginia Polytechnic Institute and State University, Prepared for the Office of Scientific Research, February 1986.

3. Kurosaka, M., "Anatomy of an Unsteady Viscous Vortex," in preparation.

4. Ng, W. F., and Epstein, A. H., "High Frequency Temperature and Pressure Probe for Unsteady Compressible Flows," Review of Scientific Instrument, Vol. 54, No. 12, December 1983, pp. 1678-1683.

5. Ng, W. F., "Review - Simultaneous Measurements of Stagnation Temperature and Pressure Using an Aspirating Probe," ASME Winter Annual Meeting, December 1986, Anaheim, California.

6. Kurosaka, M., Private Communication, September, 1986.

Table 1. Summary of UTSI/VPI Experiment #1 (Uniform Flow)

Mach Number	X/D	Y/D
0.40	1.00	0.00 0.25 0.50
0.40	2.00	0.00 0.25 0.50
0.40	4.0	0.00 0.50 0.75 1.50

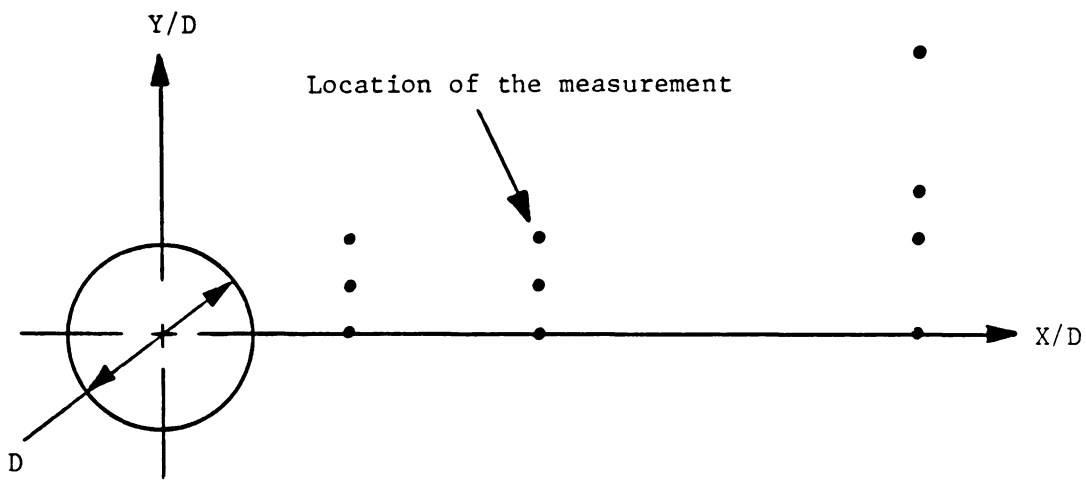

Table 2. Summary of UTSI/VPI Experiment #2 (Shear Flow)

Mach Number	X/D	Z/D
0.6	1.00	-2 0 2
0.6	4.00	-2 0 2

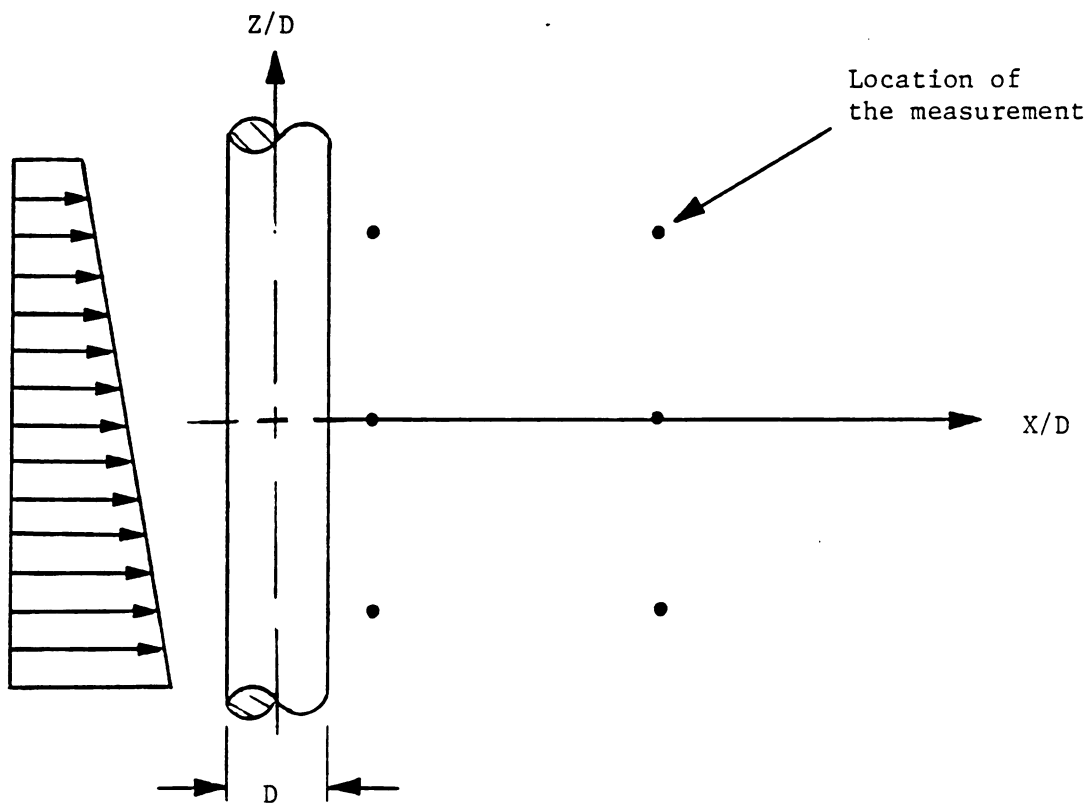

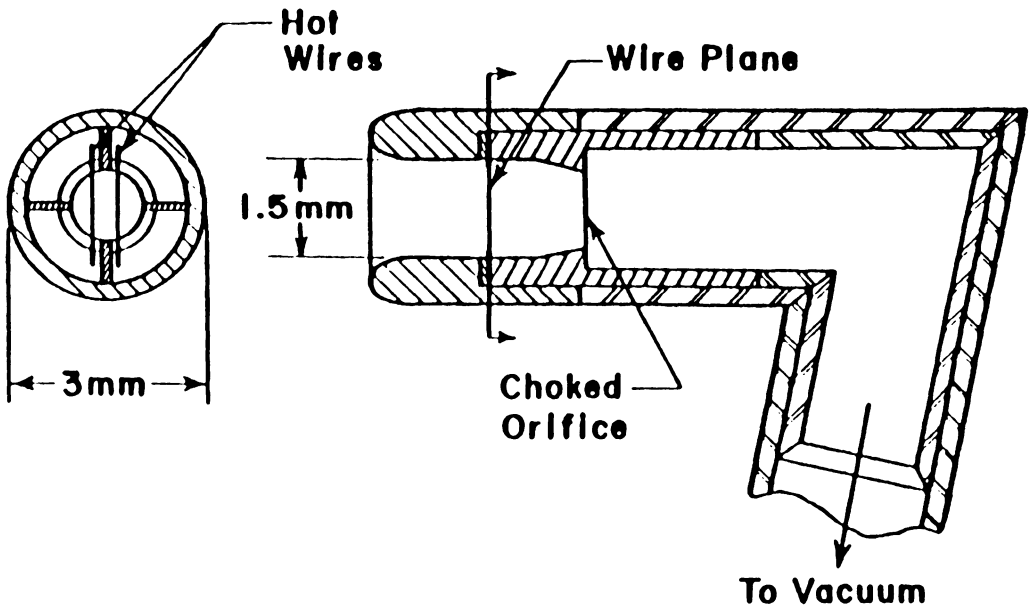

Figure 1. Cutaway of High Frequency Response Total Temperature, Total Pressure Aspirating Probe.

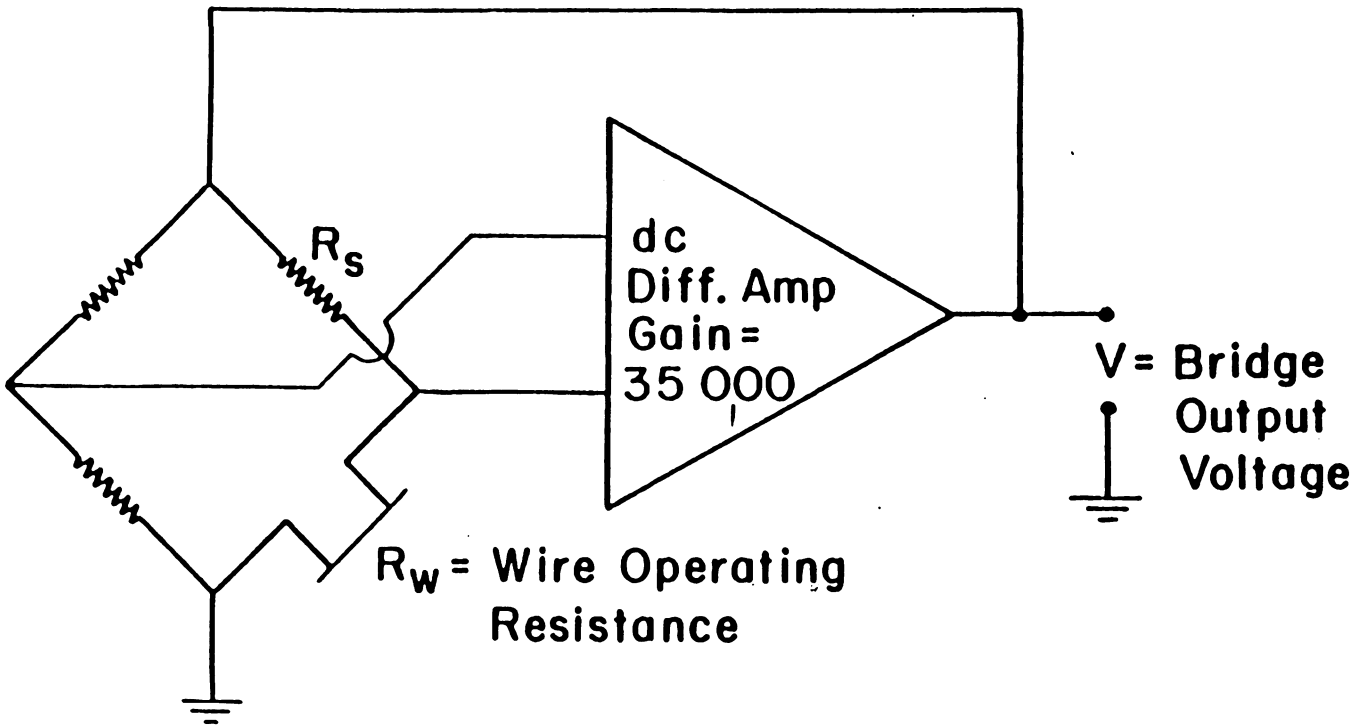

Figure 2. Schematic of Constant Temperature Hot-Wire Circuit.

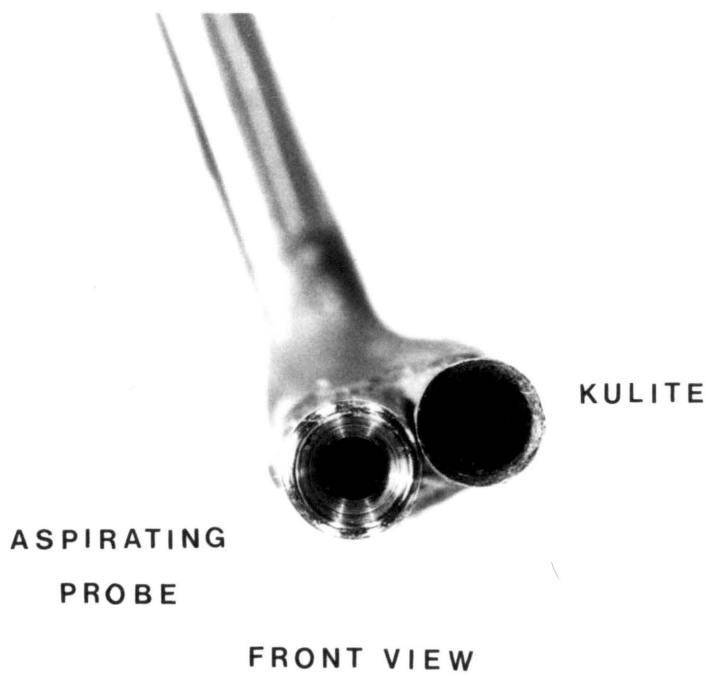

Figure 3. Picture Showing Mounting Arrangement of Aspirating Probe and Kulite Total Pressure Probe.

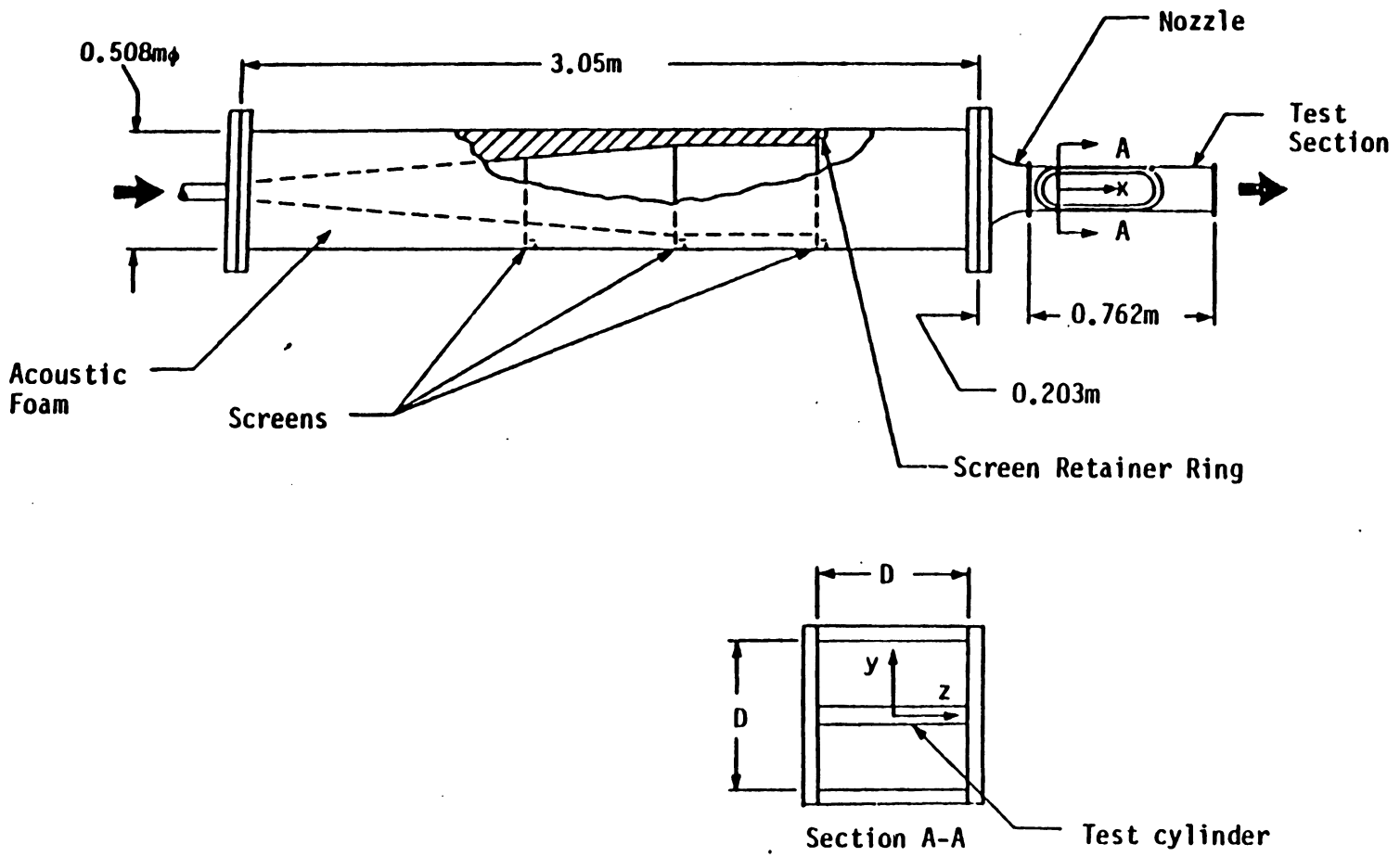

Figure 4. The UTSI High-Speed, Low-Background Noise Wind Tunnel.

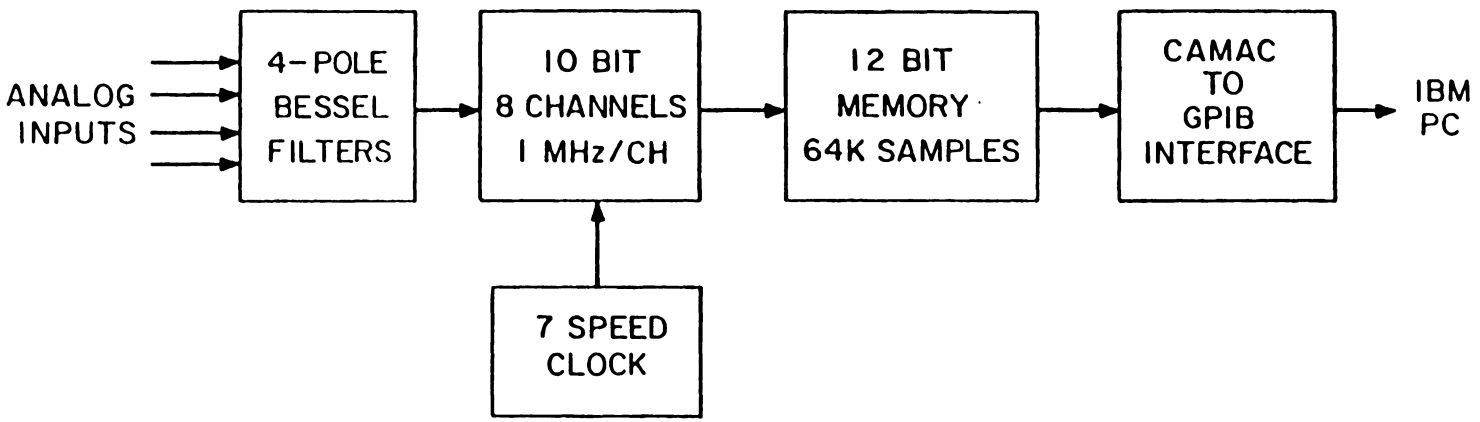

Figure 5. Schematic of the Data Acquisition System.

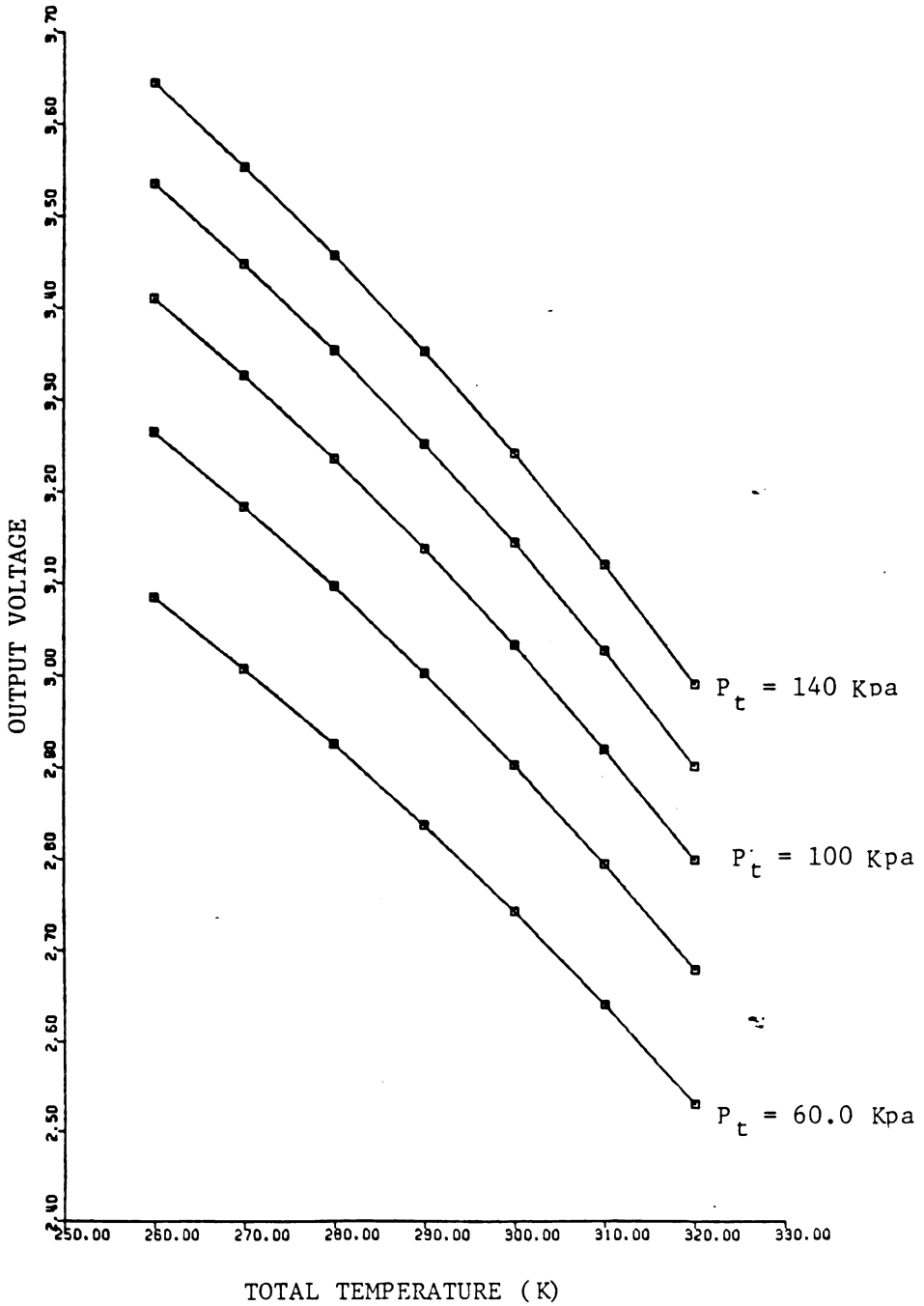

Figure 6. Typical Aspirating Probe Wire Calibration.

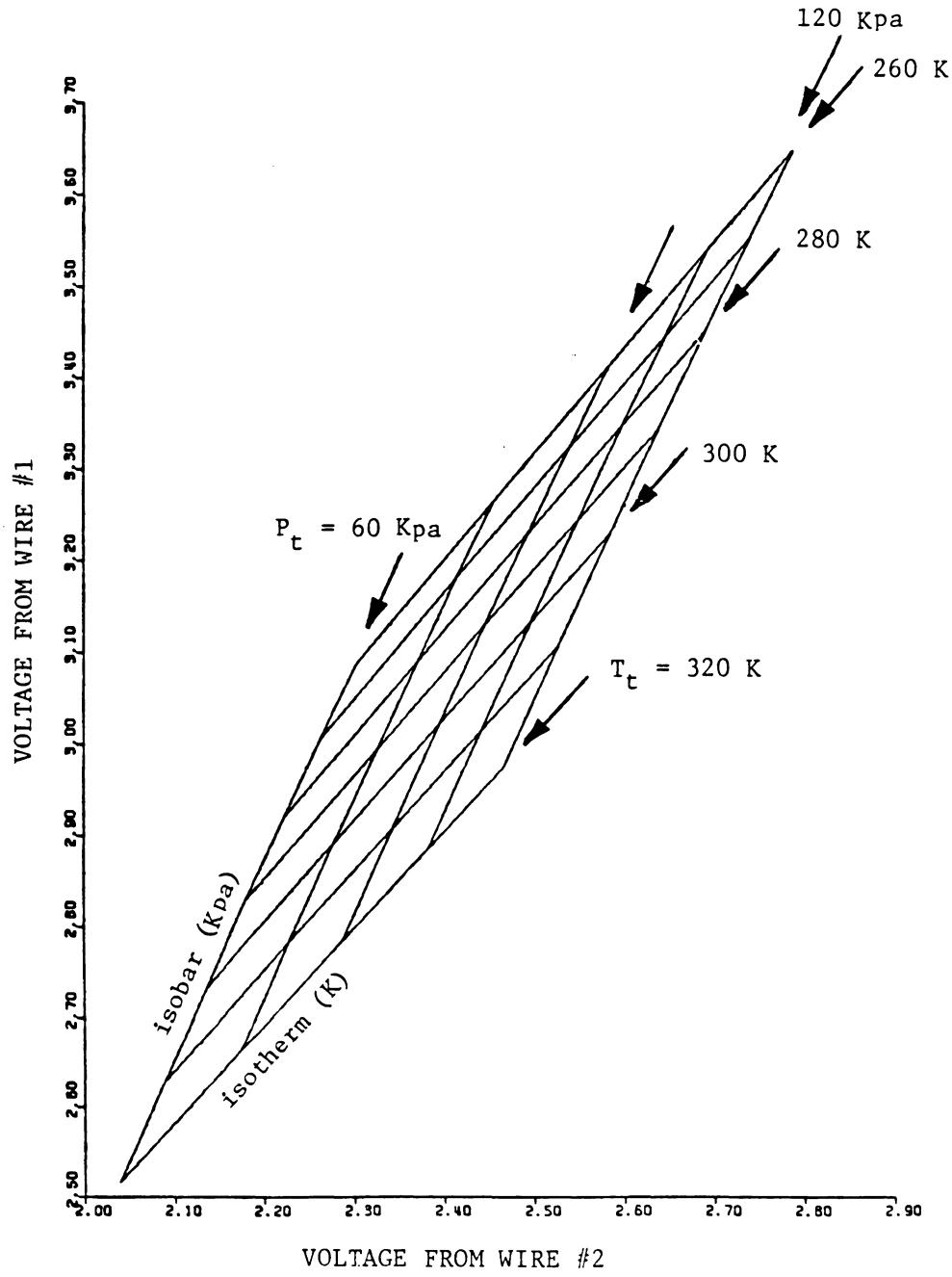

Figure 7. Dual Hot-Wire Aspirating Probe Calibration.

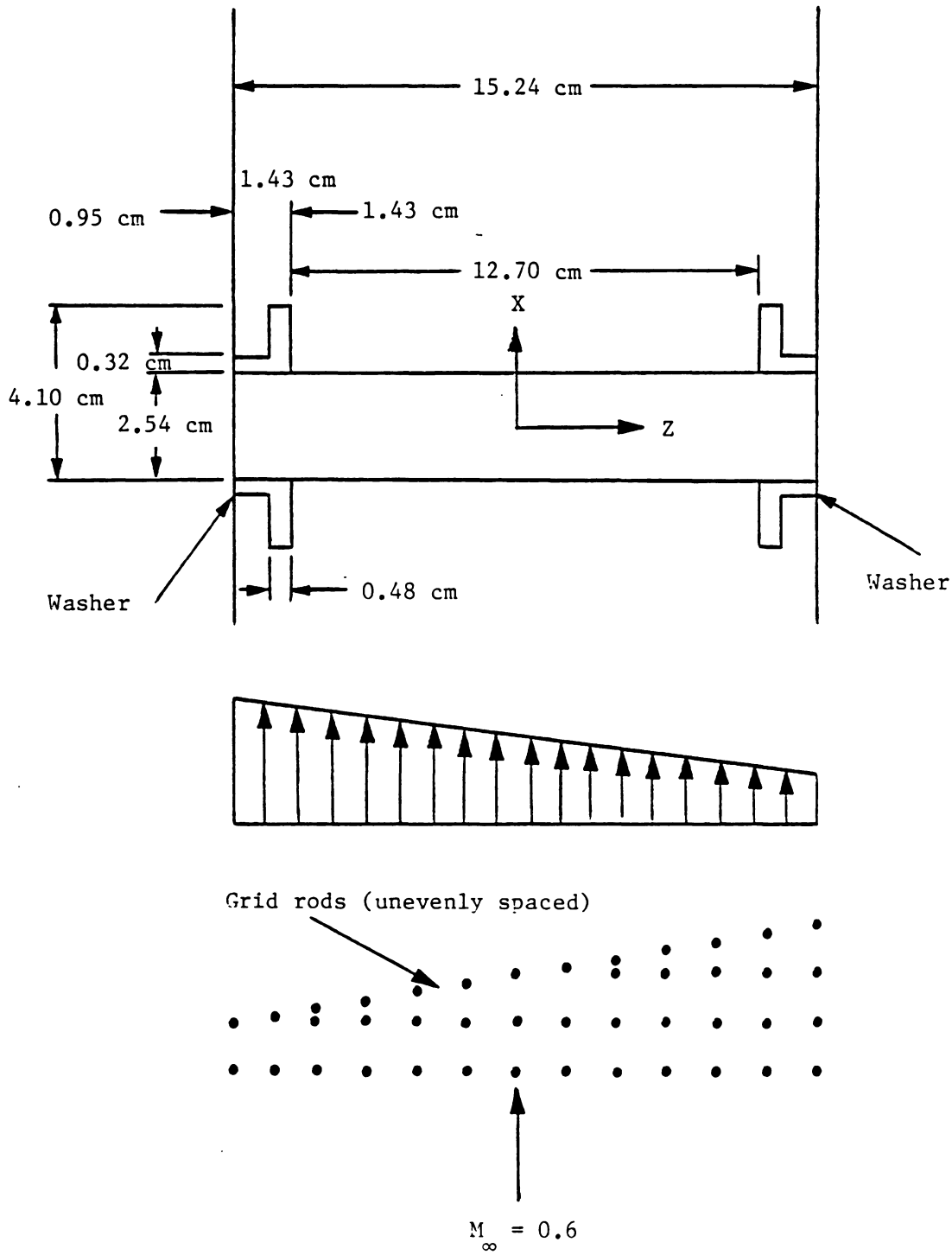

Figure 8. Schematic of the Shear Flow Passing the Cylinder.

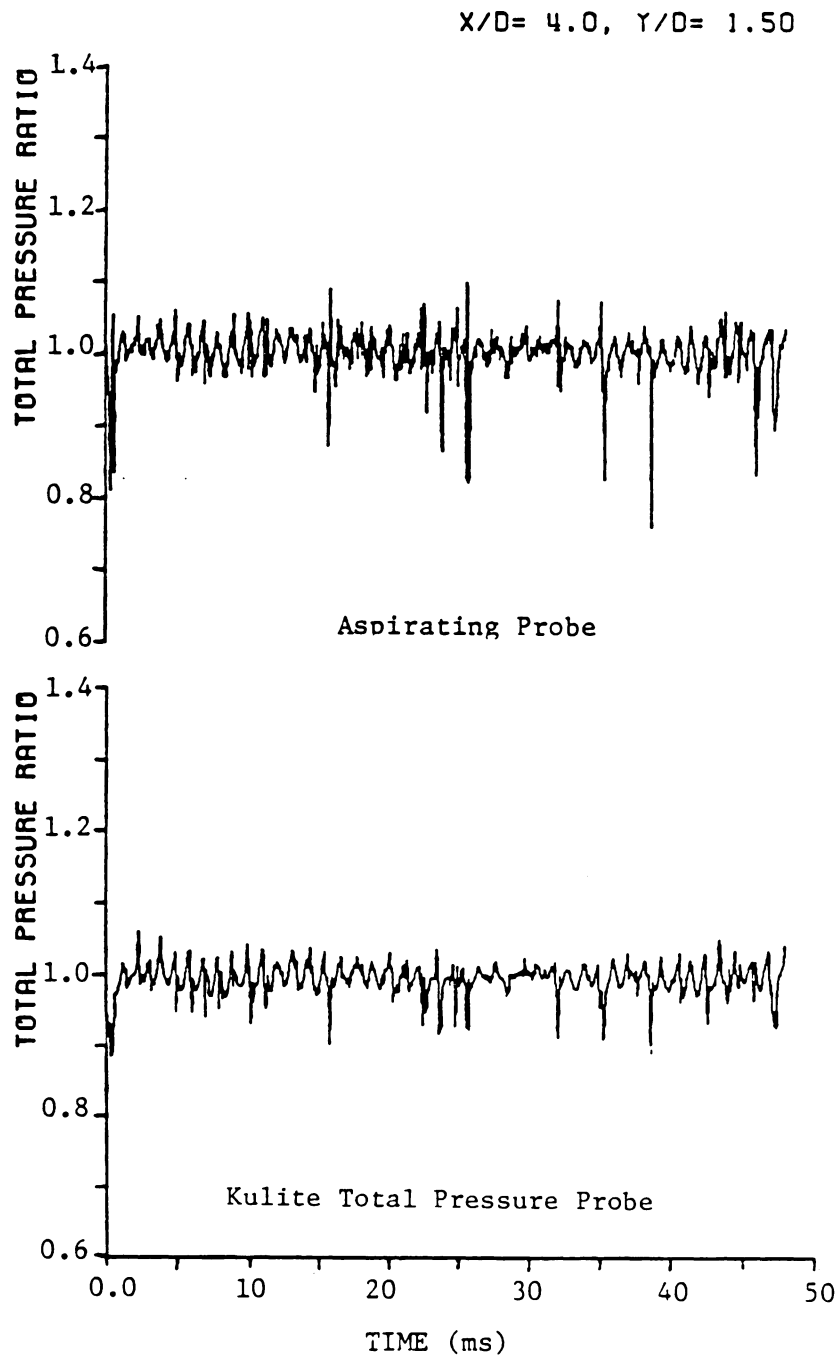

Figure 9a. Comparison of Aspirating Probe and Kulite Total Pressure Probe at X/D = 4.0, Y/D = 1.5, Complete Time Trace.

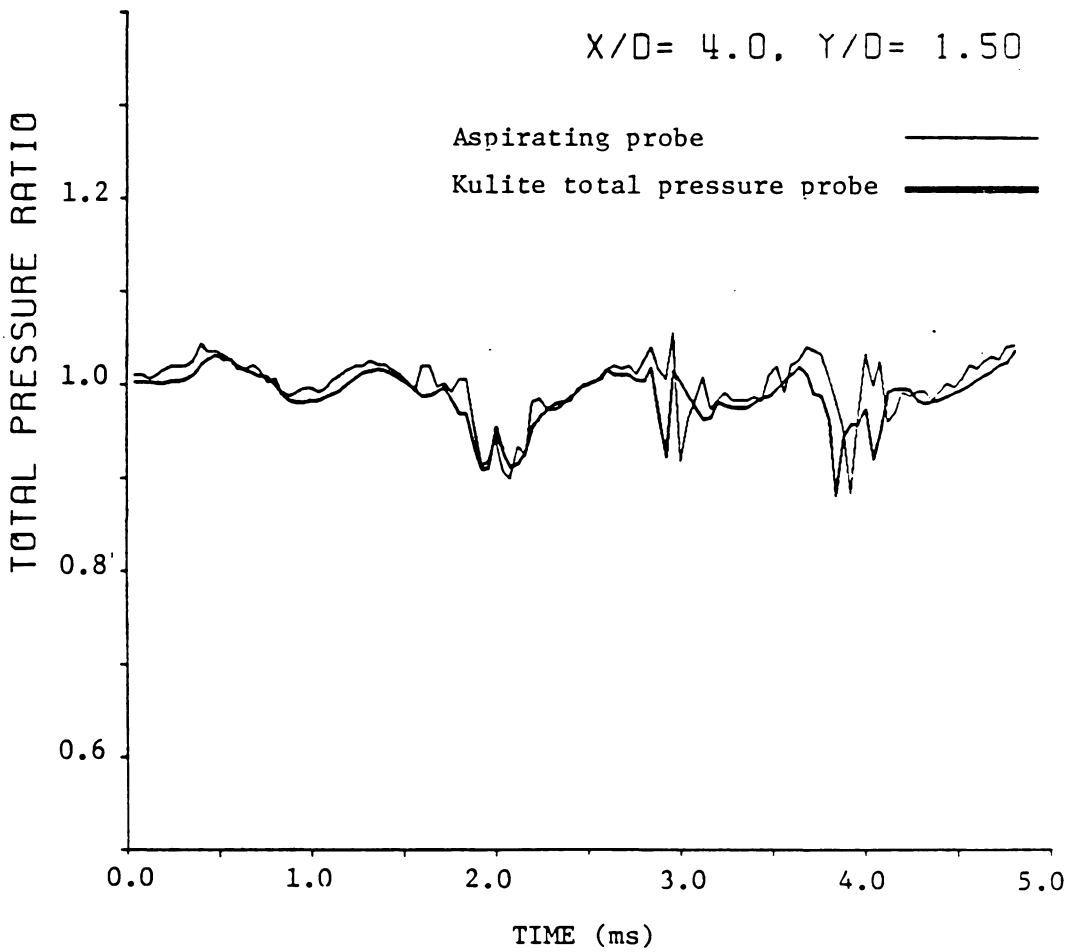

Figure 9b. Comparison of Aspirating Probe and Kulite Total Pressure Probe at X/D = 4.0, Y/D = 1.5, Expanded Time Scale.

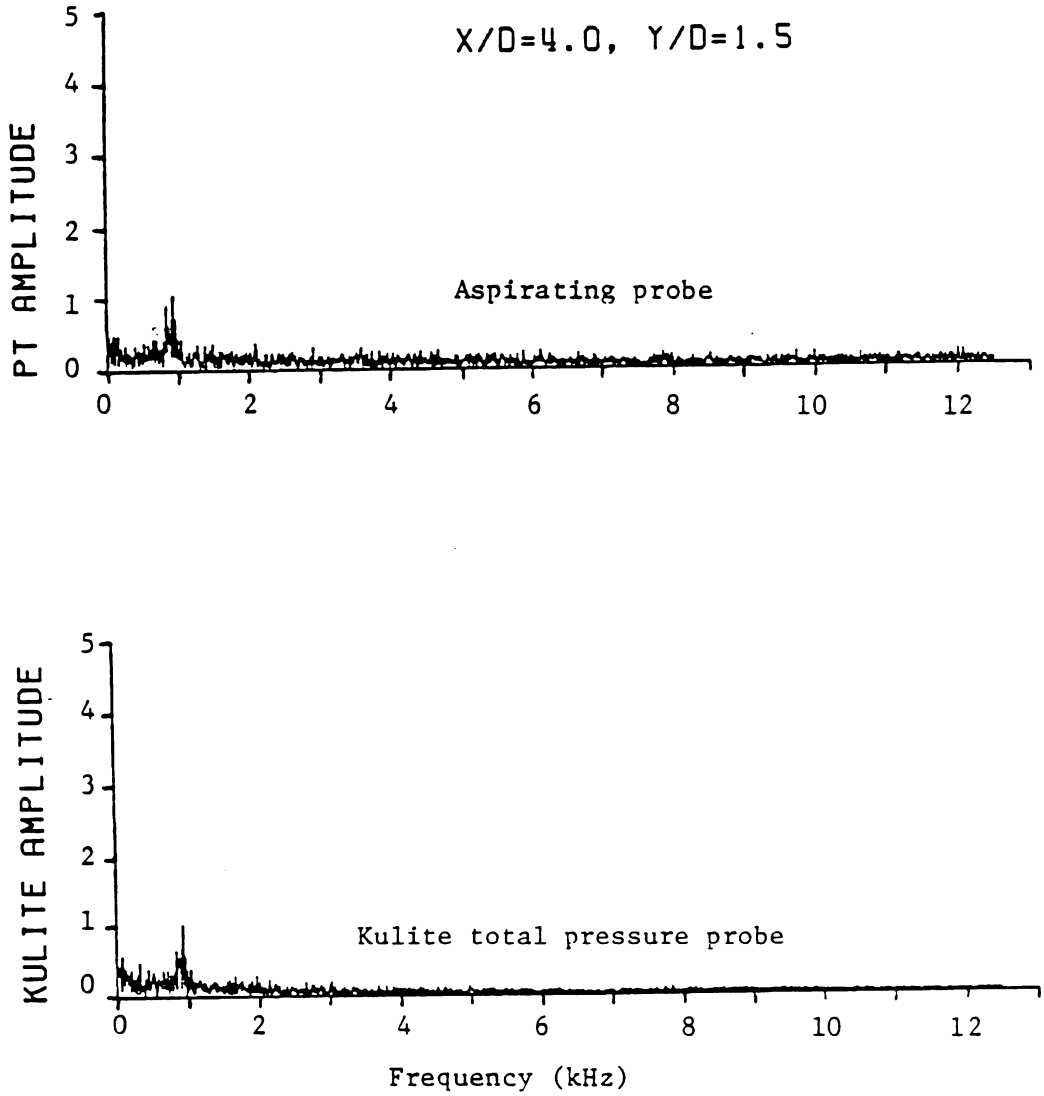

Figure 9c. Comparison of Aspirating Probe and Kulite Total Pressure Probe at X/D = 4.0, Y/D = 1.5, Frequency Spectra.

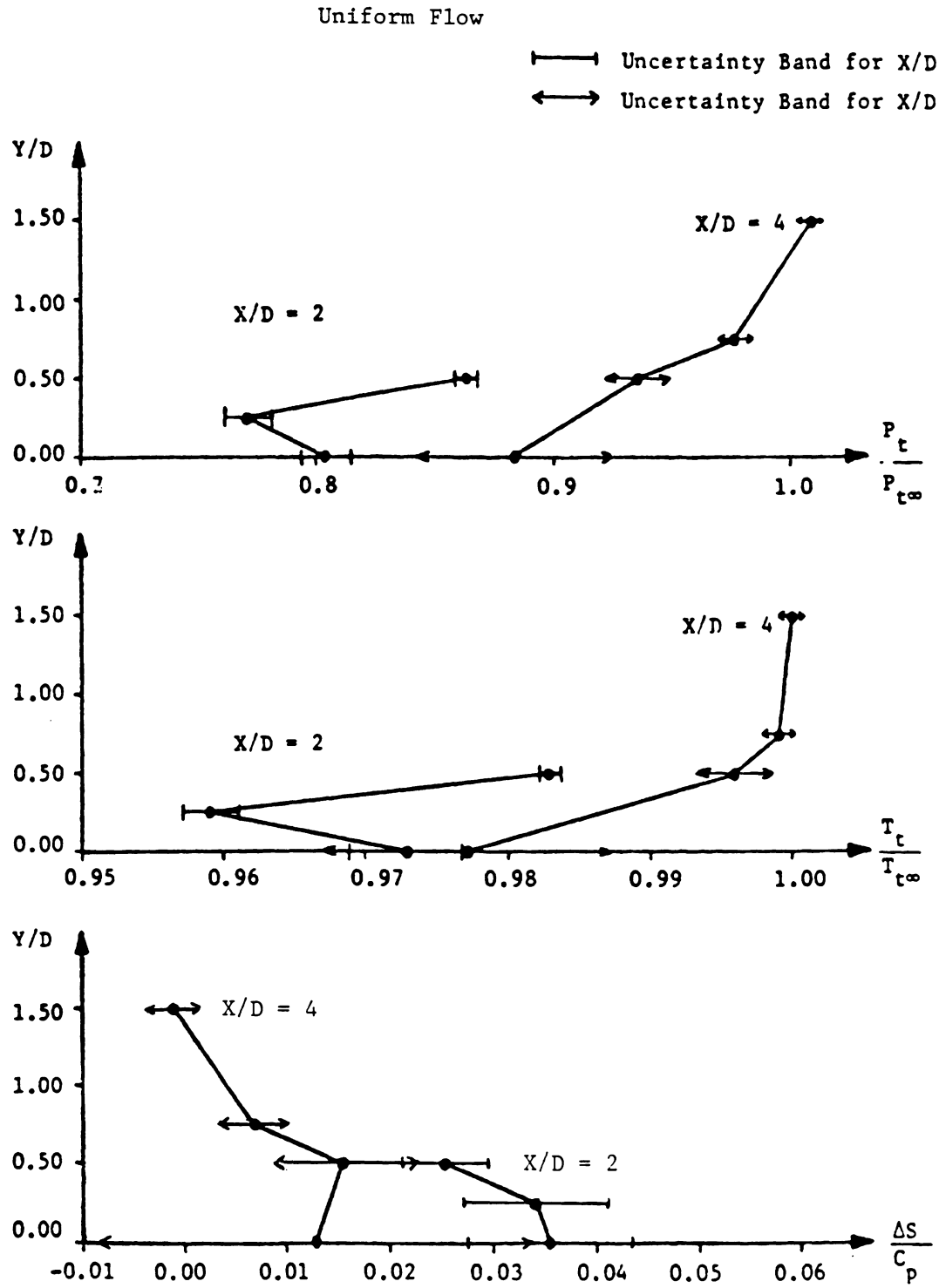

Figure 10. dc Plot for the Nondimensionalized Stagnation Pressure ($P_t/P_{t\infty}$), Stagnation Temperature ($T_t/T_{t\infty}$) and entropy ($\Delta S/C_p$) at X/D = 2 and 4; uniform flow.

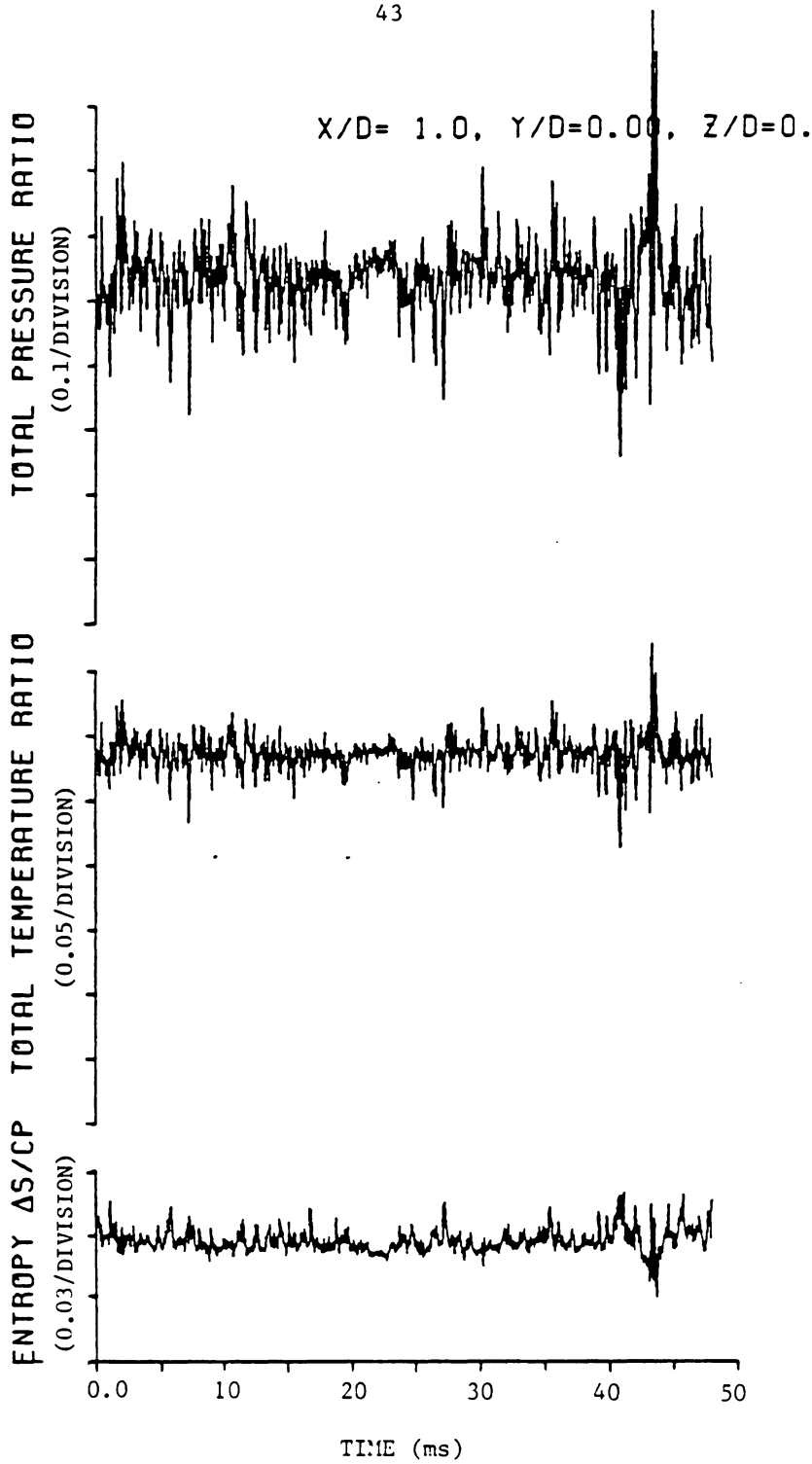

Figure 11a. Time-Resolved Stagnation Pressure, Stagnation Temperature and Entropy at X/D = 1.0, Y/D = 0.0, and Z/D = 0.0; Uniform Flow, Complete Time Trace.

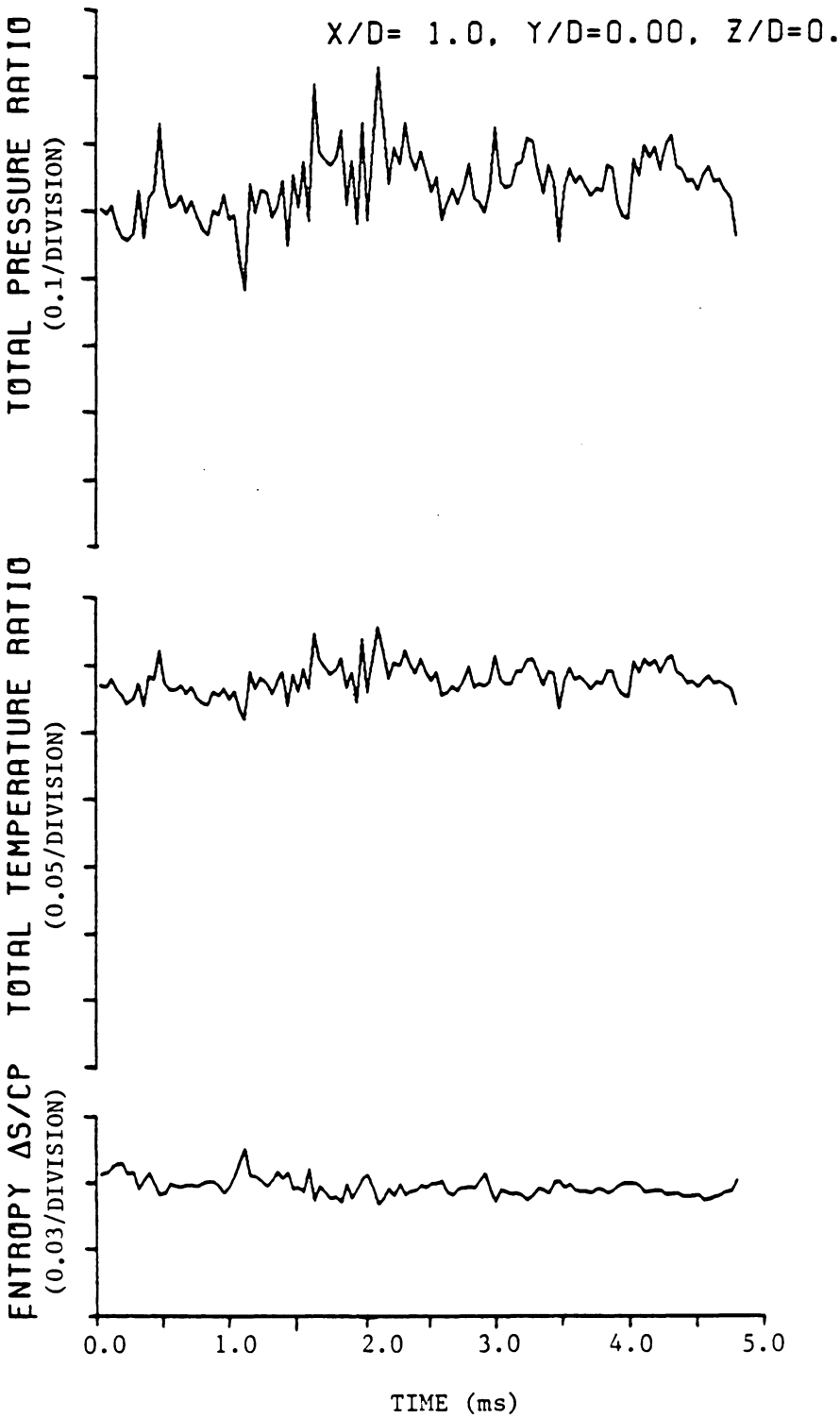

Figure 11b. Time-Resolved Stagnation Pressure, Stagnation Temperature and Entropy at X/D = 1.0, Y/D = 0.0, and Z/D = 0.0; Uniform Flow, Expanded Time Scale.

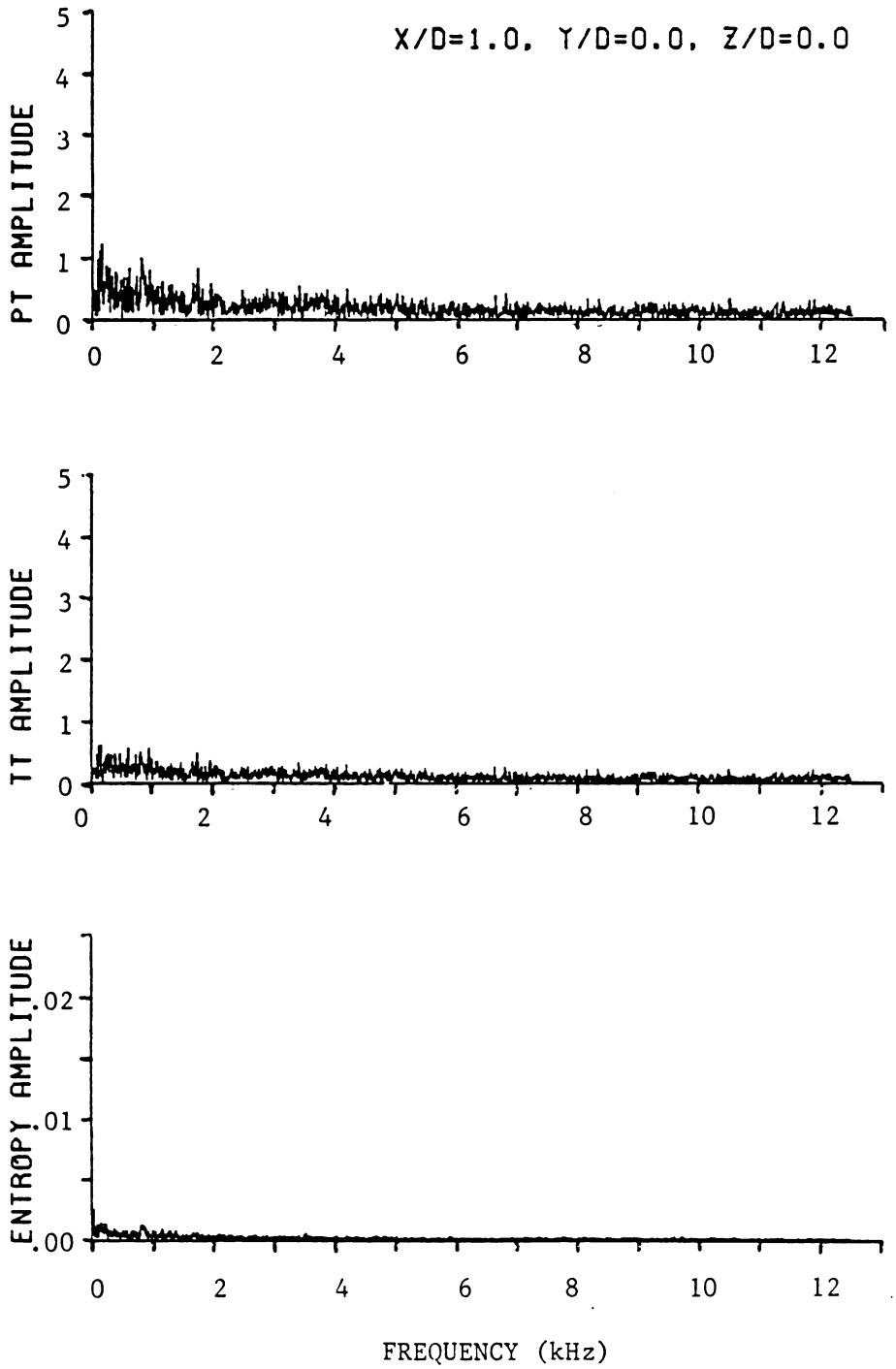

Figure 11c. Time-Resolved Stagnation Pressure, Stagnation Temperature and Entropy at X/D = 1.0, Y/D = 0.0, and Z/D = 0.0; Uniform Flow, Frequency Spectra.

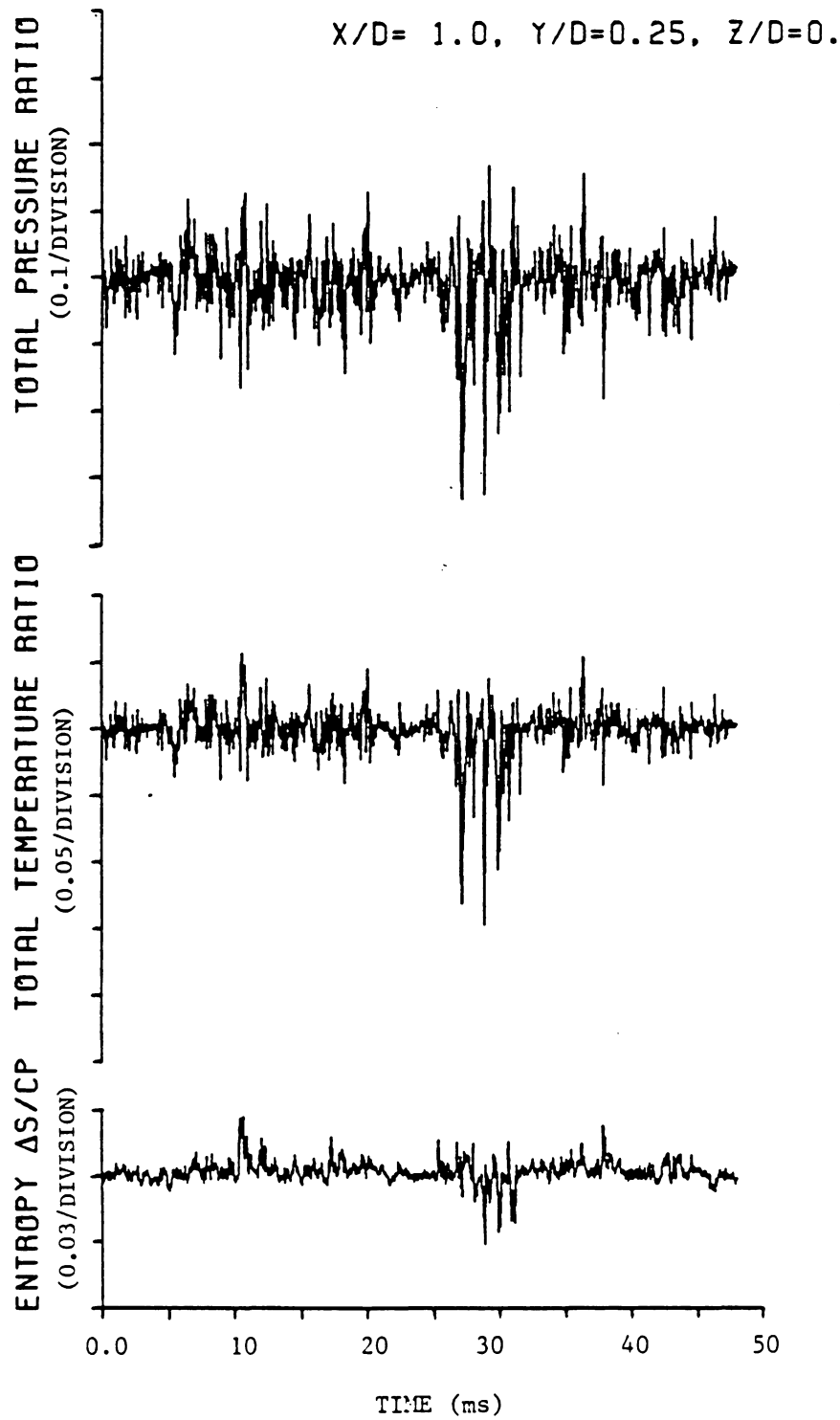

Figure 12a. Time-Resolved Stagnation Pressure, Stagnation Temperature and Entropy at X/D = 1, Y/D = 0.25, and Z/D = 0.0; Uniform Flow, Complete Time Trace.

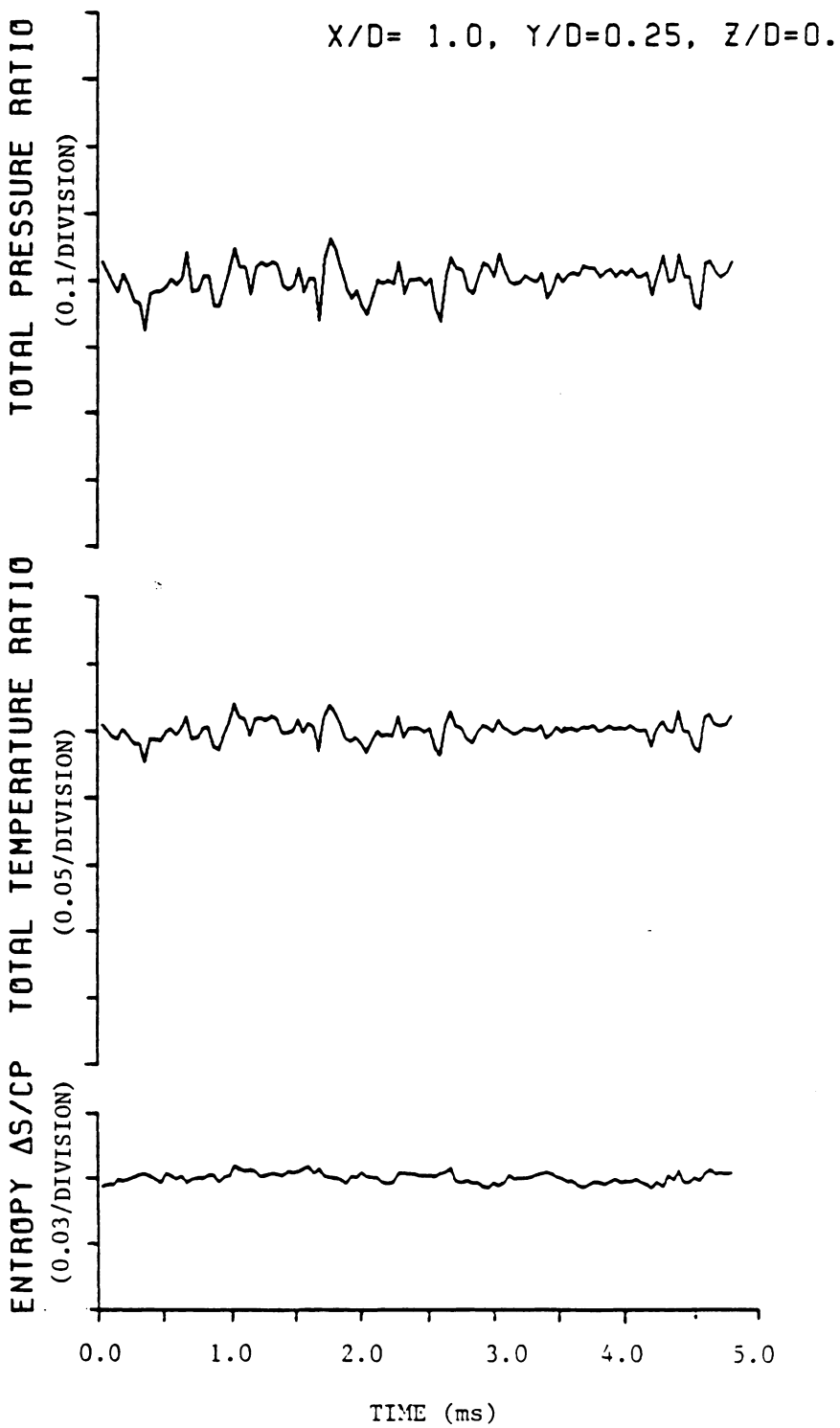

Figure 12b. Time-Resolved Stagnation Pressure, Stagnation Temperature and Entropy at X/D = 1, Y/D = 0.25, and Z/D = 0.0; Uniform Flow, Expanded Time Scale.

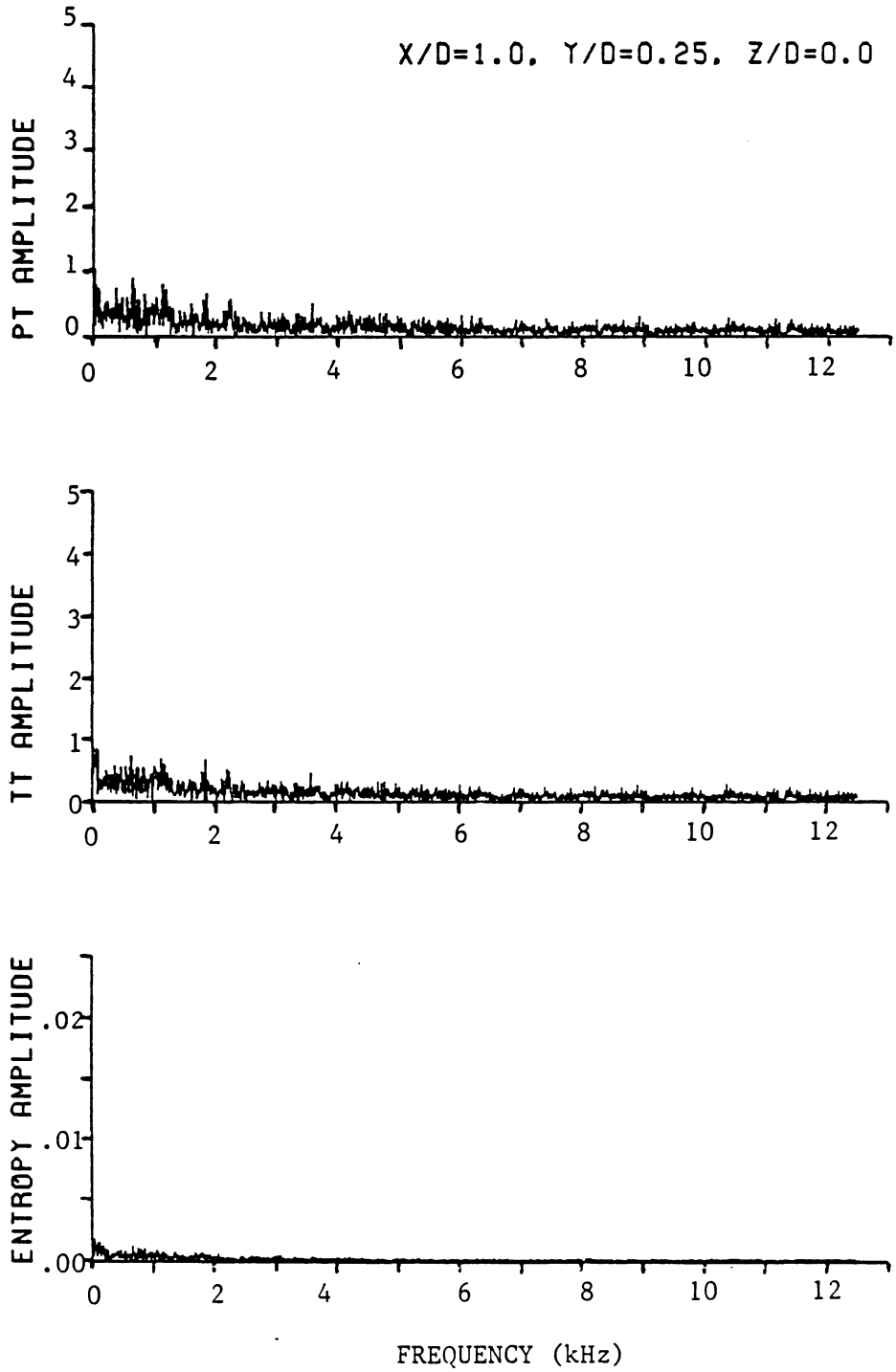

Figure 12c. Time-Resolved Stagnation Pressure, Stagnation Temperature and Entropy at X/D = 1, Y/D = 0.25, and Z/D = 0.0; Uniform Flow, Frequency Spectra.

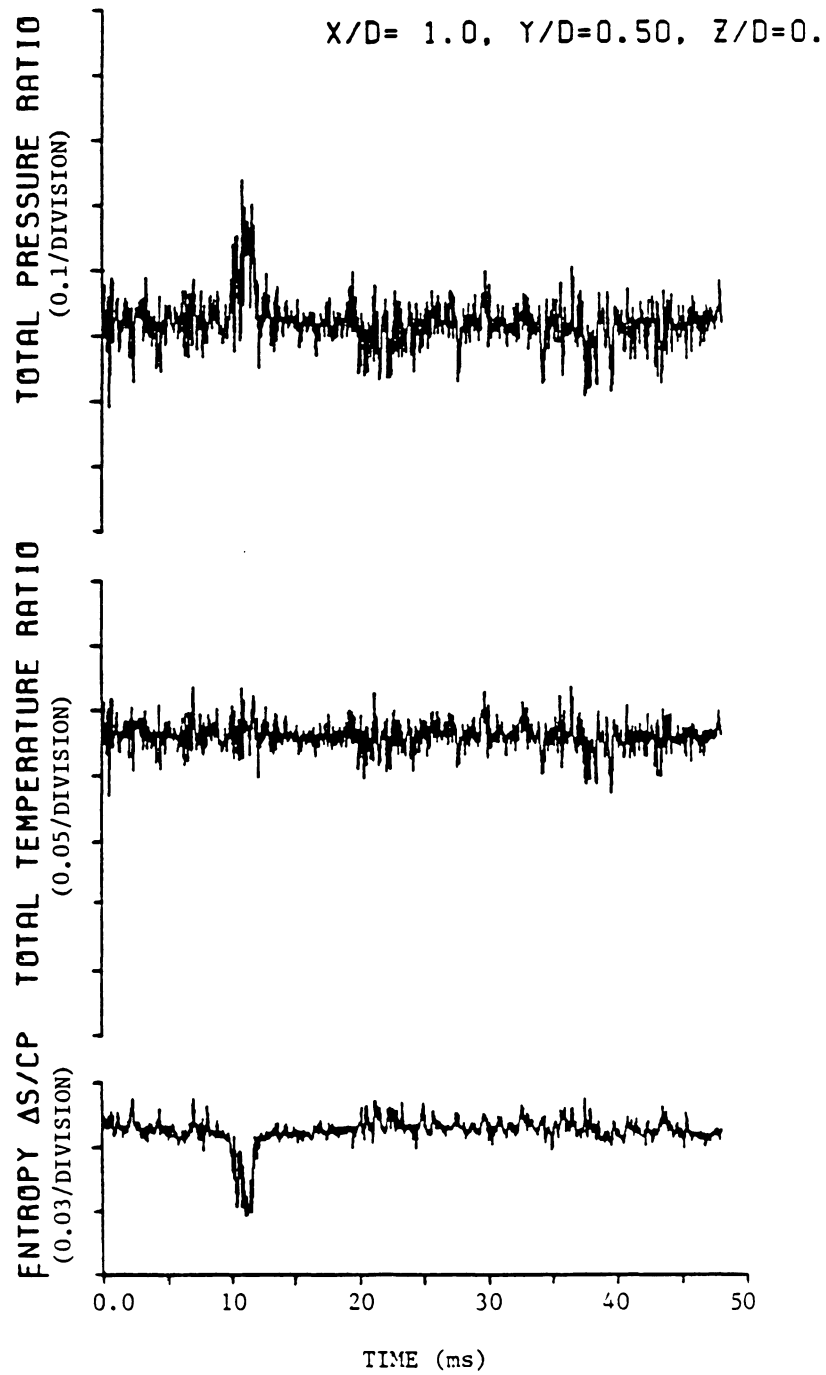

Figure 13a. Time-Resolved Stagnation Pressure, Stagnation Temperature and Entropy at X/D = 1, Y/D = 0.5, and Z/D = 0.0; Uniform Flow, Complete Time Trace.

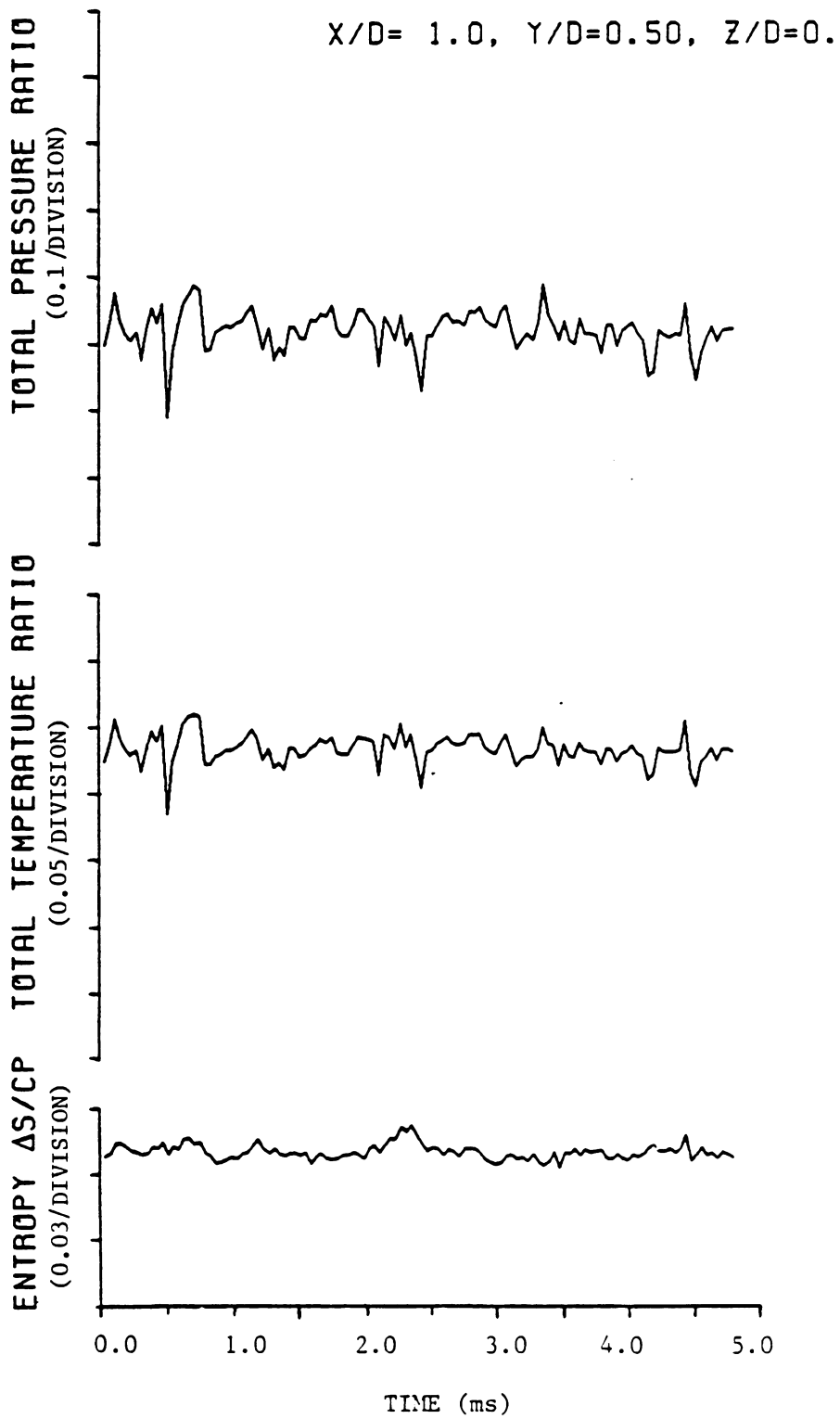

Figure 13b. Time-Resolved Stagnation Pressure, Stagnation Temperature and Entropy at X/D = 1, Y/D = 0.5, and Z/D = 0.0; Uniform Flow, Expanded Time Scale.

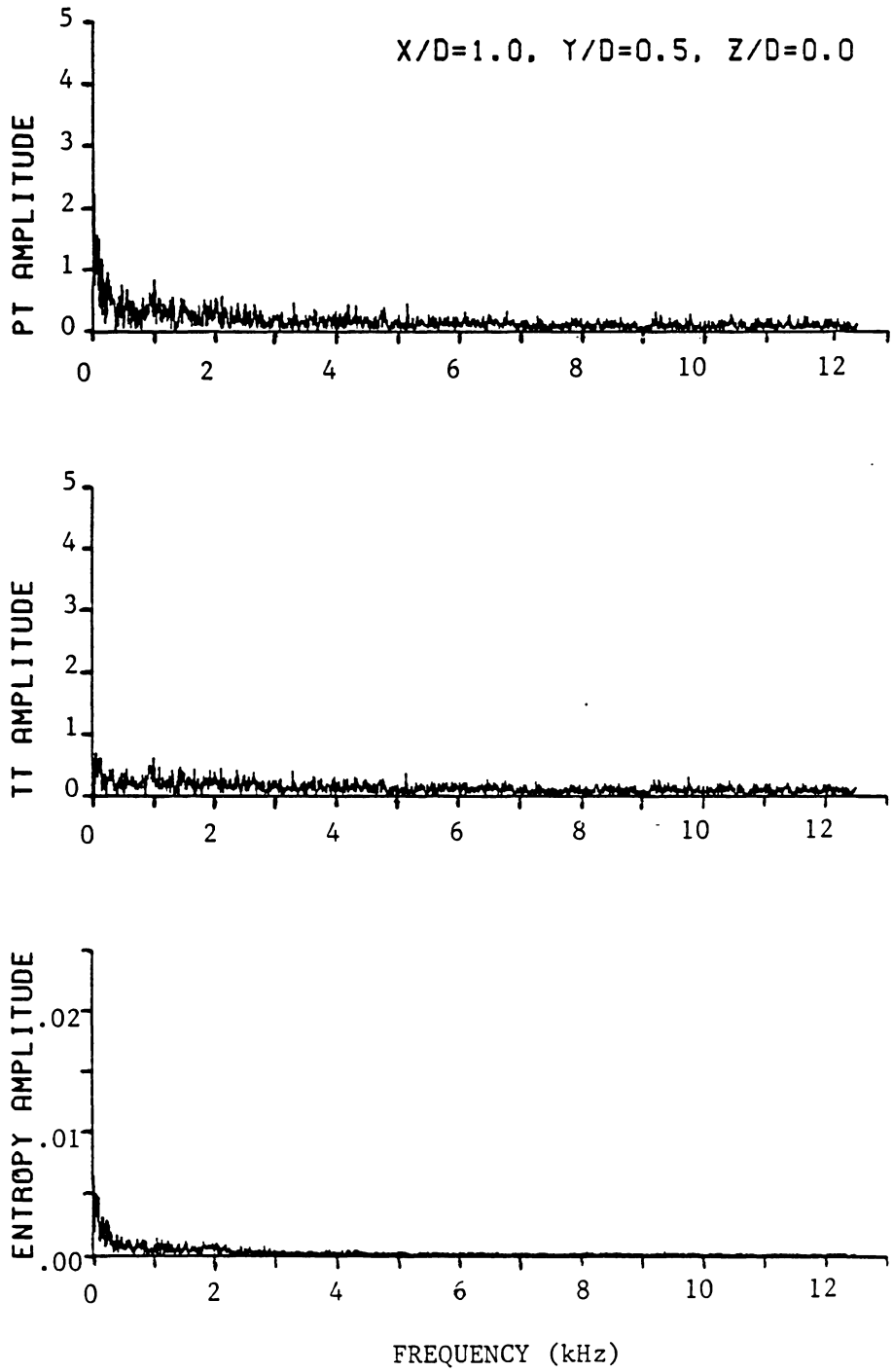

Figure 13c. Time-Resolved Stagnation Pressure, Stagnation Temperature and Entropy at X/D = 1, Y/D = 0.5, and Z/D = 0.0; Uniform Flow, Frequency Spectra.

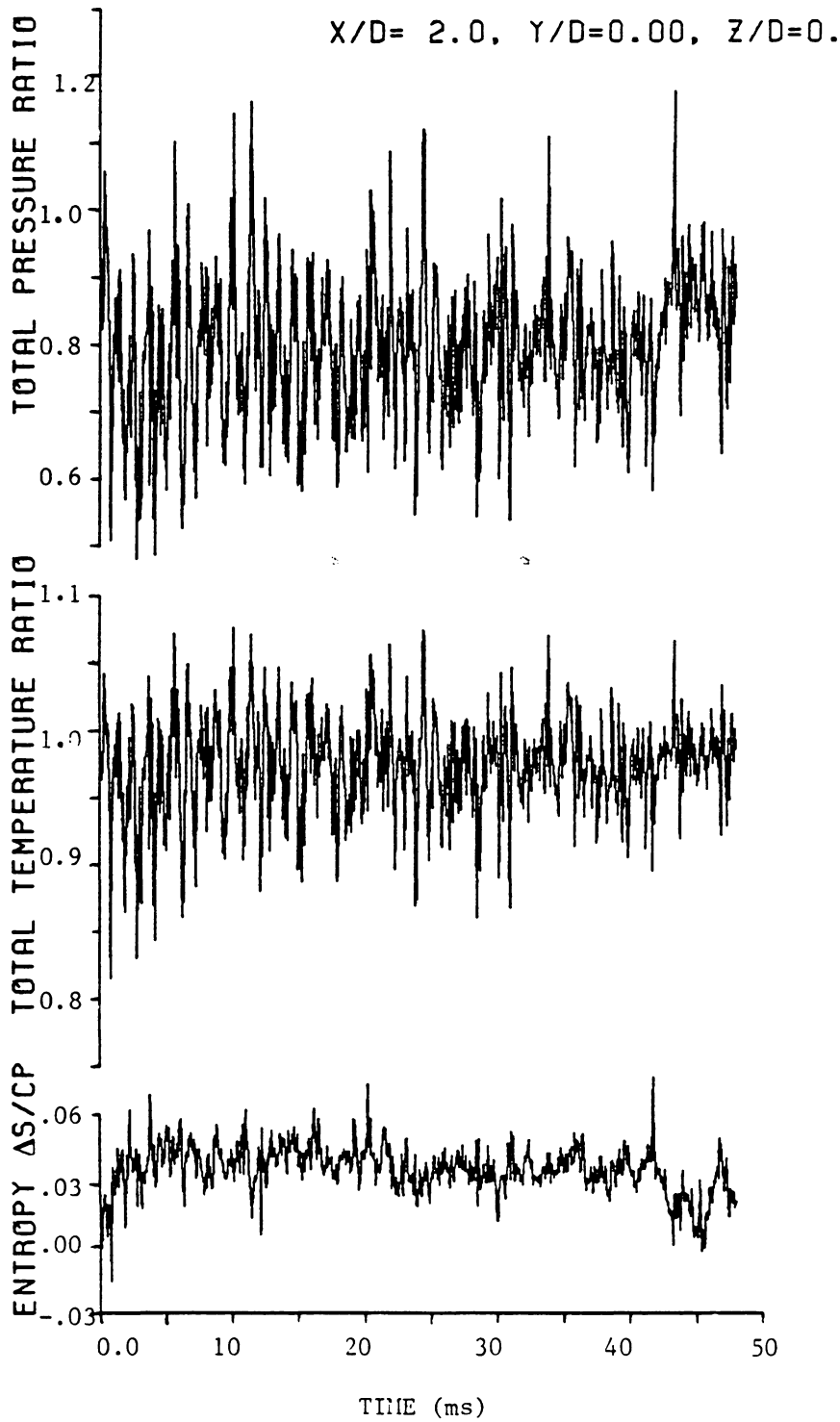

Figure 14a. Time-Resolved Stagnation Pressure, Stagnation Temperature and Entropy at X/D = 2, Y/D = 0.0, and Z/D = 0.0; Uniform Flow, Complete Time Trace.

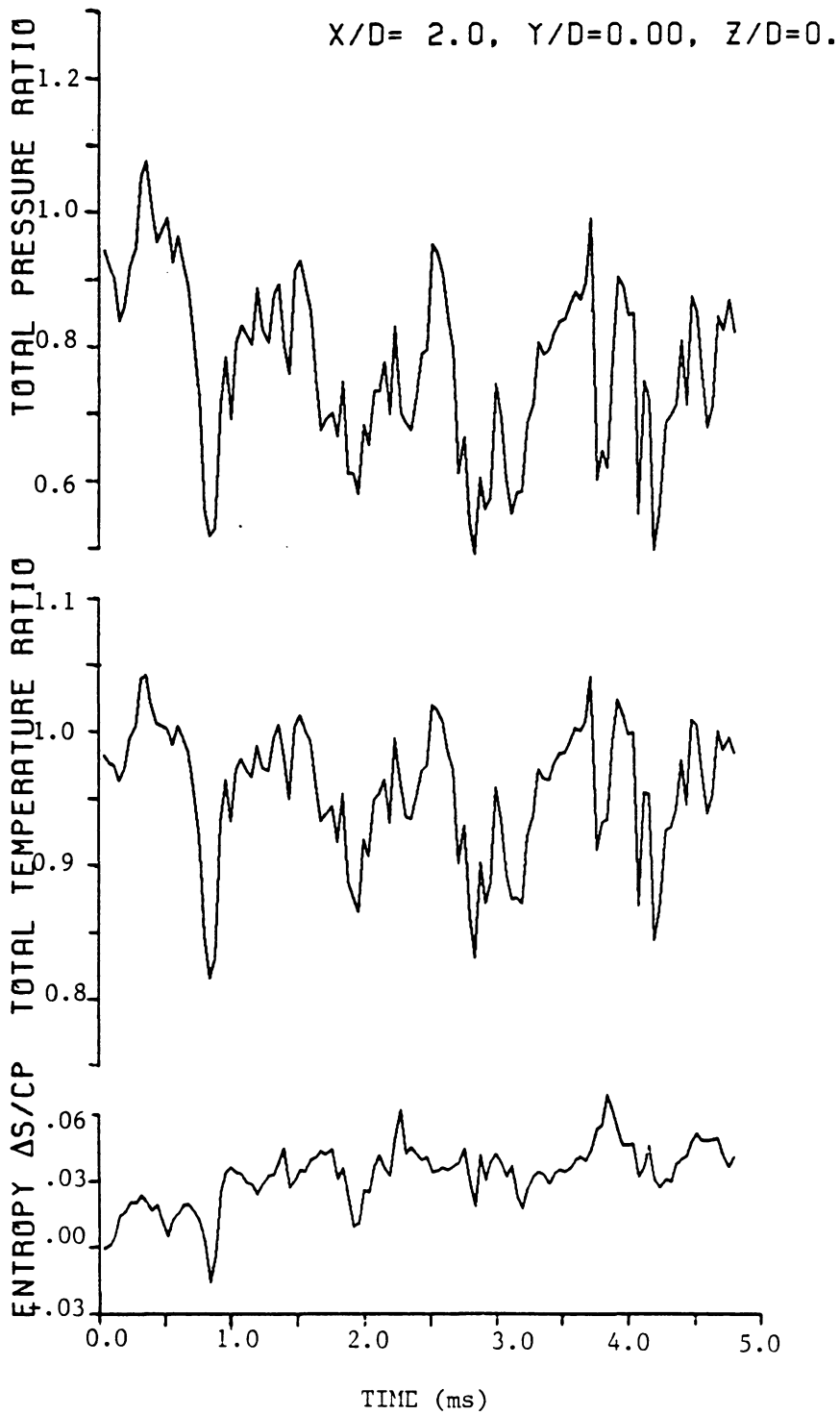

Figure 14b. Time-Resolved Stagnation Pressure, Stagnation Temperature and Entropy at X/D = 2, Y/D = 0.0, and Z/D = 0.0; Uniform Flow, Expanded Time Scale.

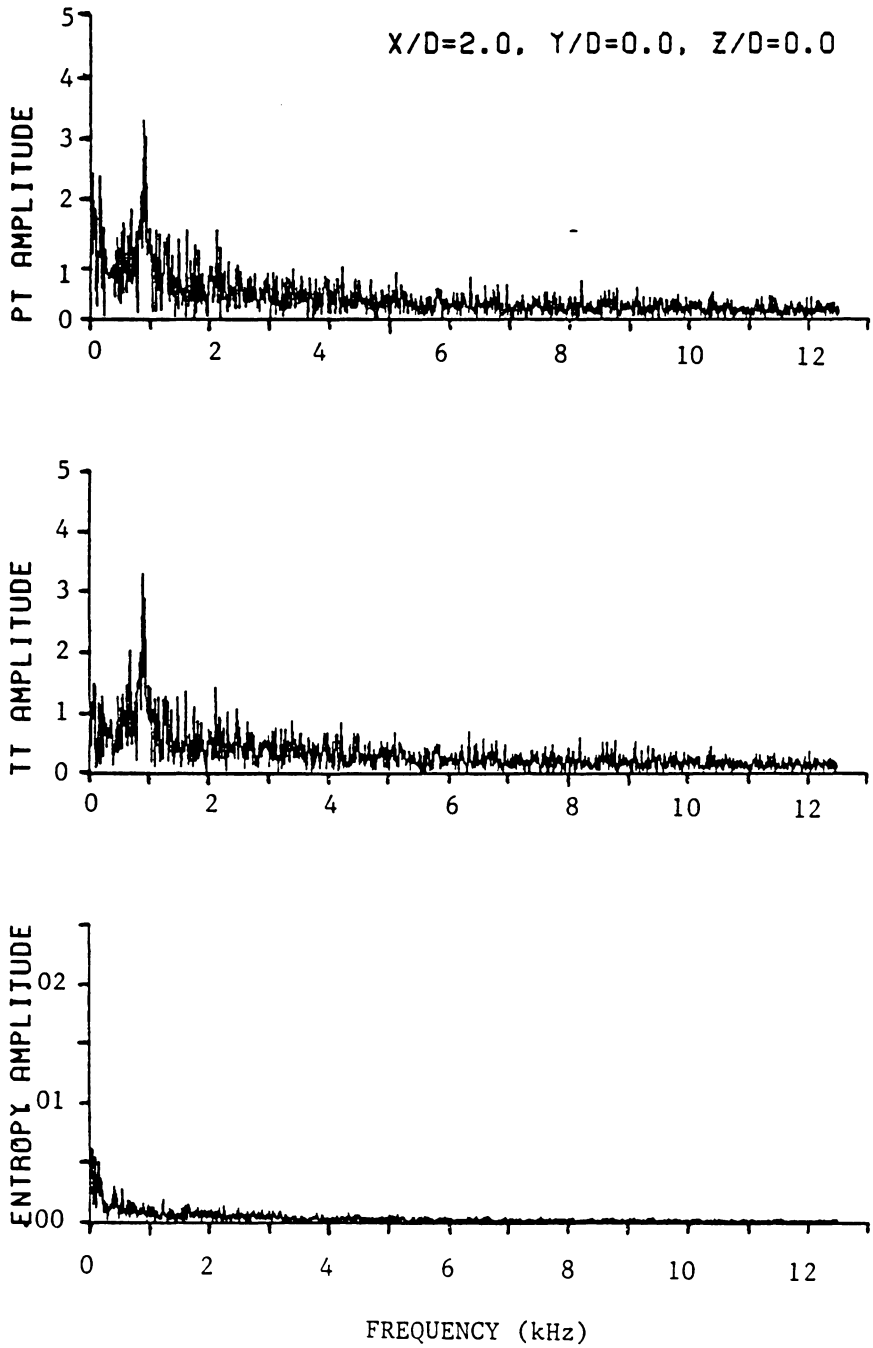

Figure 14c. Time-Resolved Stagnation Pressure, Stagnation Temperature and Entropy at X/D = 2, Y/D = 0.0, and Z/D = 0.0; Uniform Flow, Frequency Spectra.

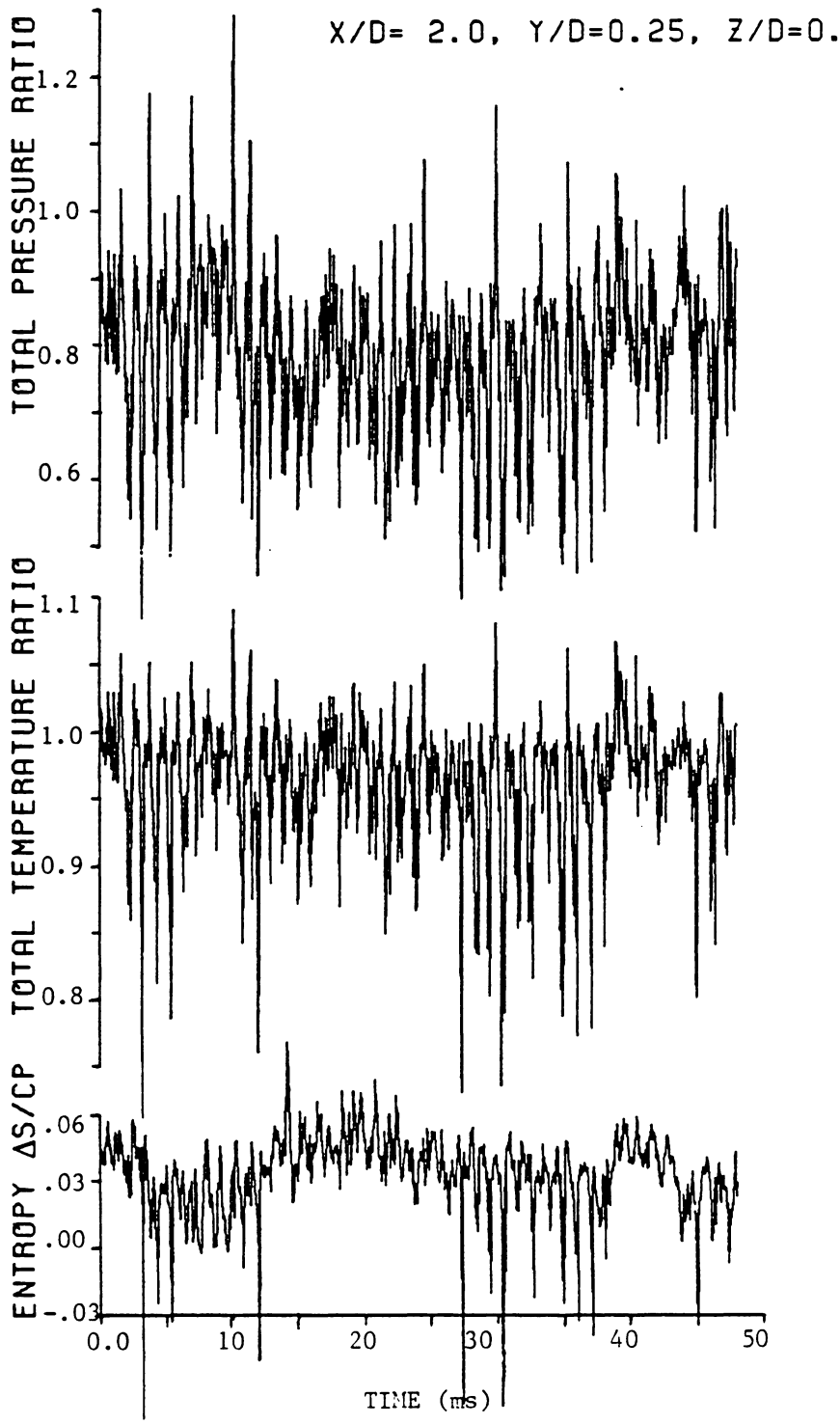

Figure 15a. Time-Resolved Stagnation Pressure, Stagnation Temperature and Entropy at X/D = 2, Y/D = 0.25, and Z/D = 0.0; Uniform Flow, Complete Time Trace.

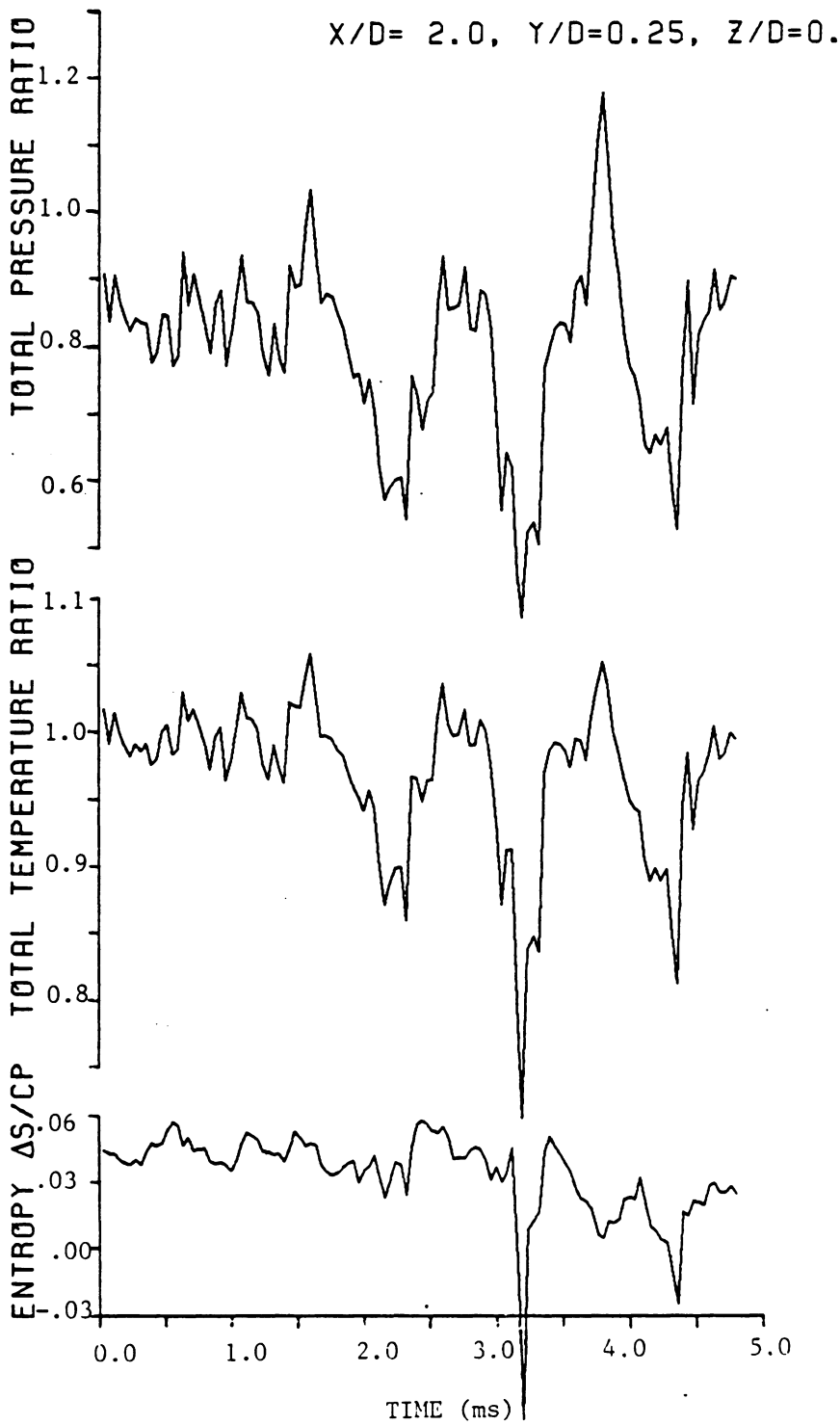

Figure 15b. Time-Resolved Stagnation Pressure, Stagnation Temperature Entropy at X/D = 2, Y/D = 0.25, and Z/D = 0.0; Uniform Flow, Expanded Time Scale.

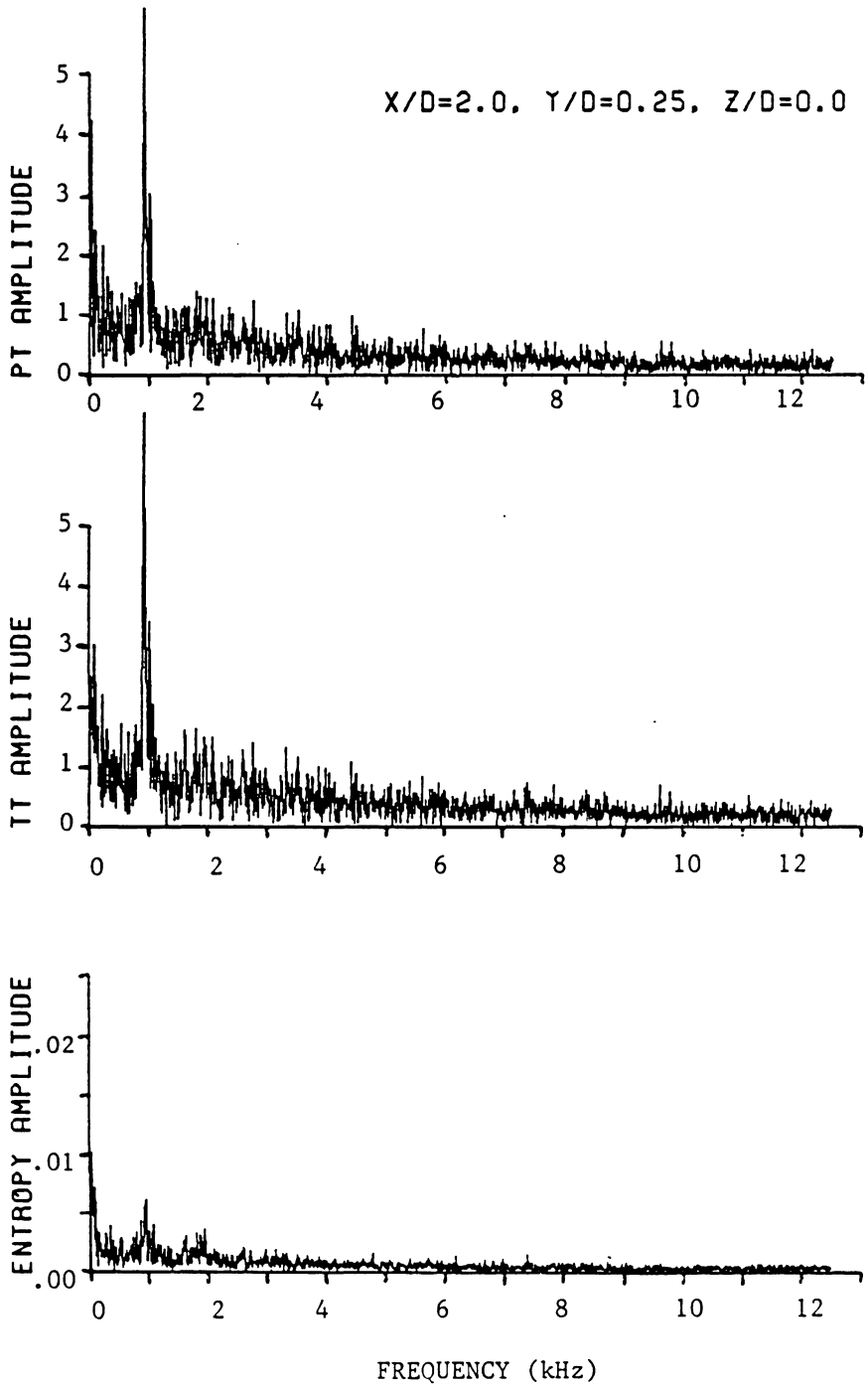

Figure 15c. Time-Resolved Stagnation Pressure, Stagnation Temperature Entropy at X/D = 2, Y/D = 0.25, and Z/D = 0.0; Uniform Flow, Frequency Spectra.

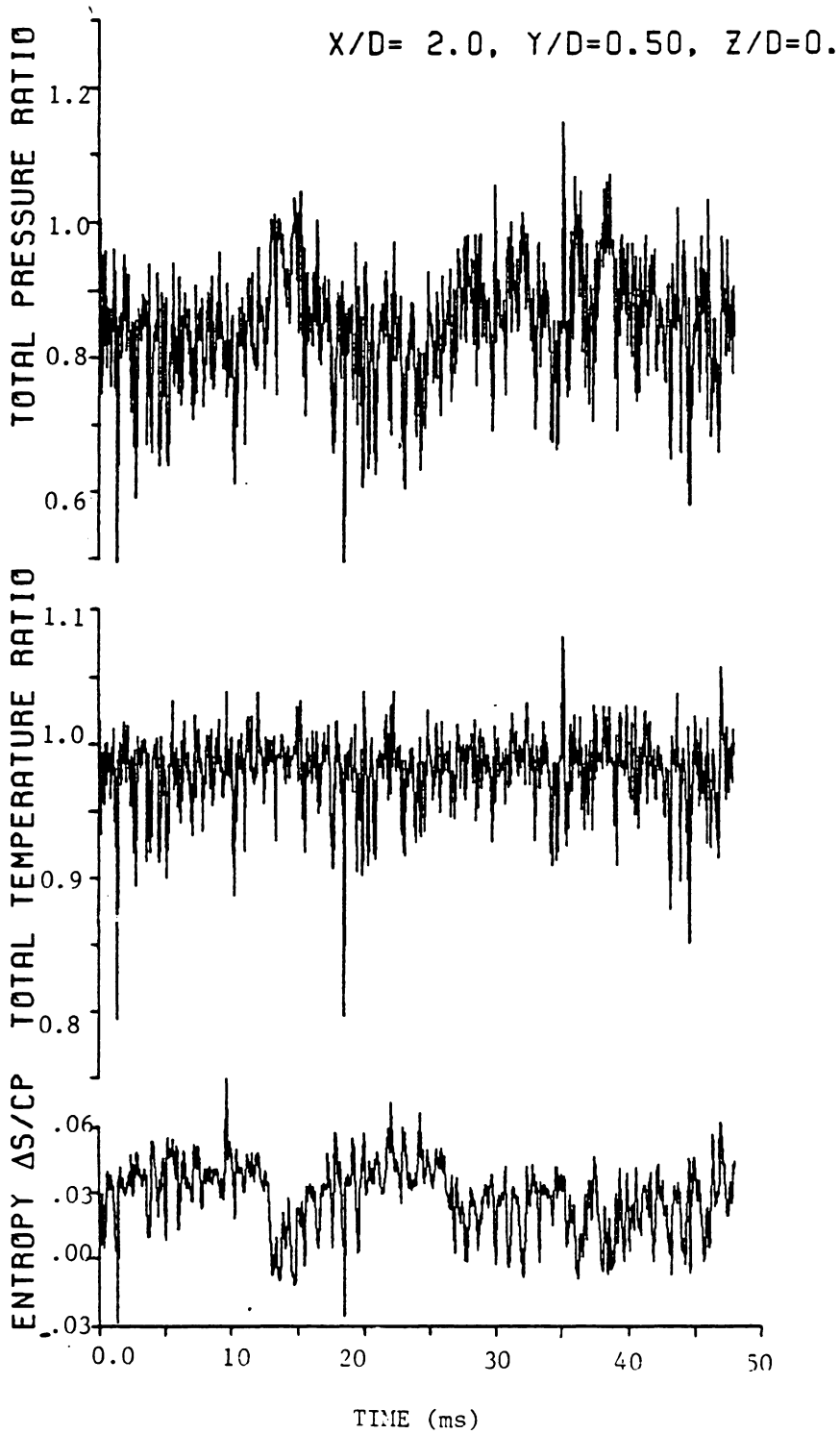

Figure 16a. Time-Resolved Stagnation Pressure, Stagnation Temperature and Entropy at X/D = 2, Y/D = 0.50, and Z/D = 0.0; Uniform Flow, Complete Time Trace.

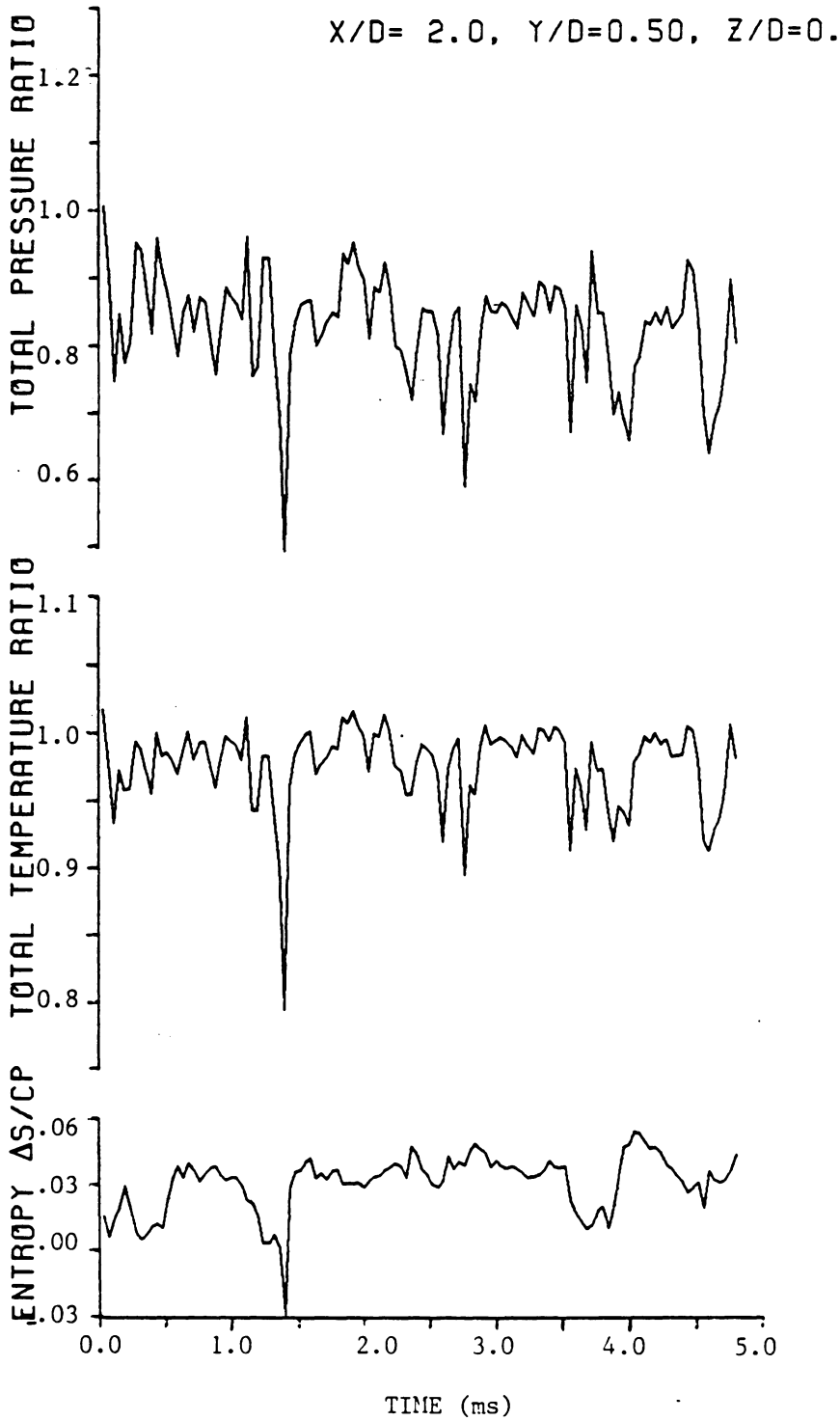

Figure 16b. Time-Resolved Stagnation Pressure, Stagnation Temperature and Entropy at X/D = 2, Y/D = 0.50, and Z/D = 0.0; Uniform Flow, Expanded Time Scale.

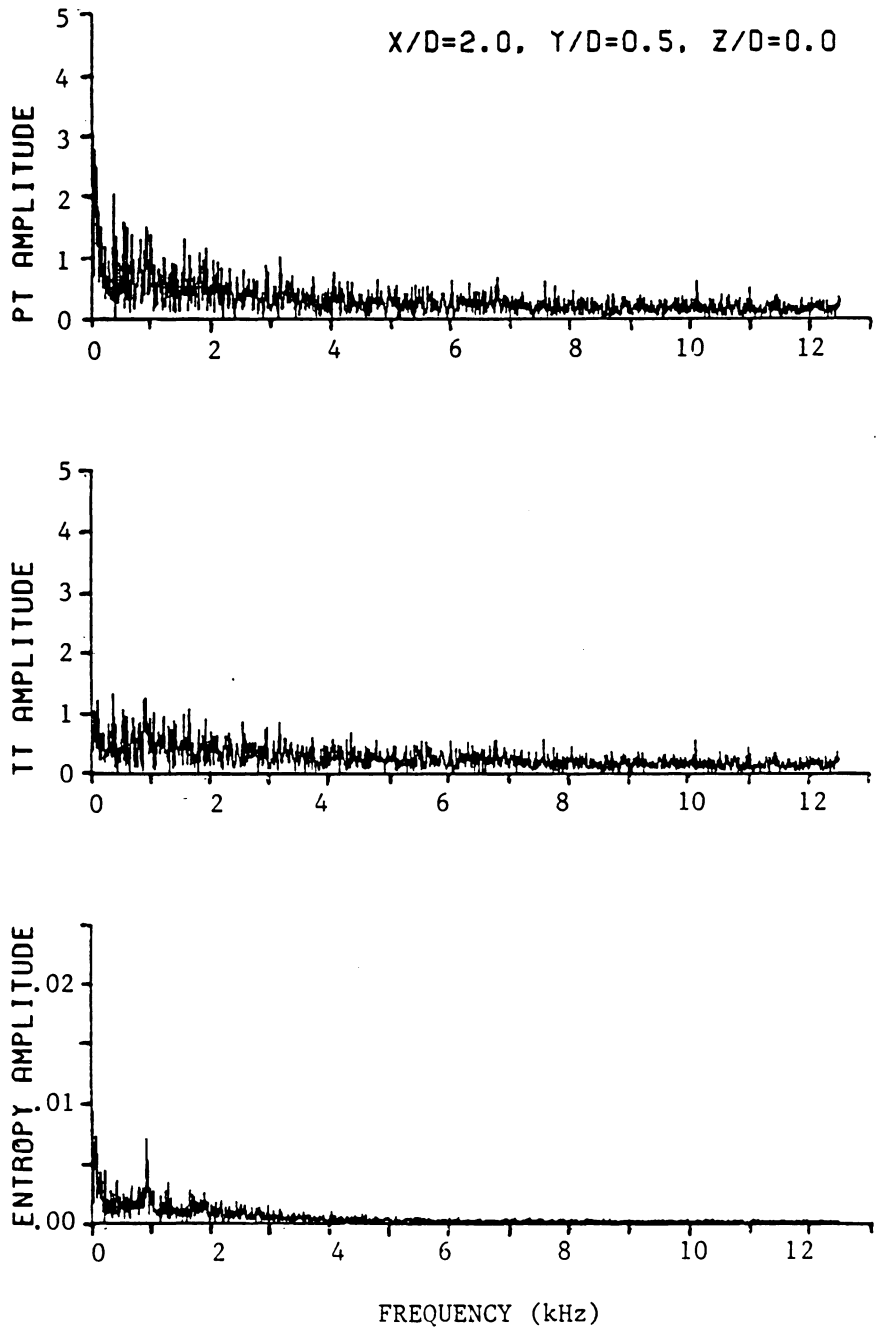

Figure 16c. Time-Resolved Stagnation Pressure, Stagnation Temperature and Entropy at X/D = 2, Y/D = 0.50, and Z/D = 0.0; Uniform Flow, Frequency Spectra.

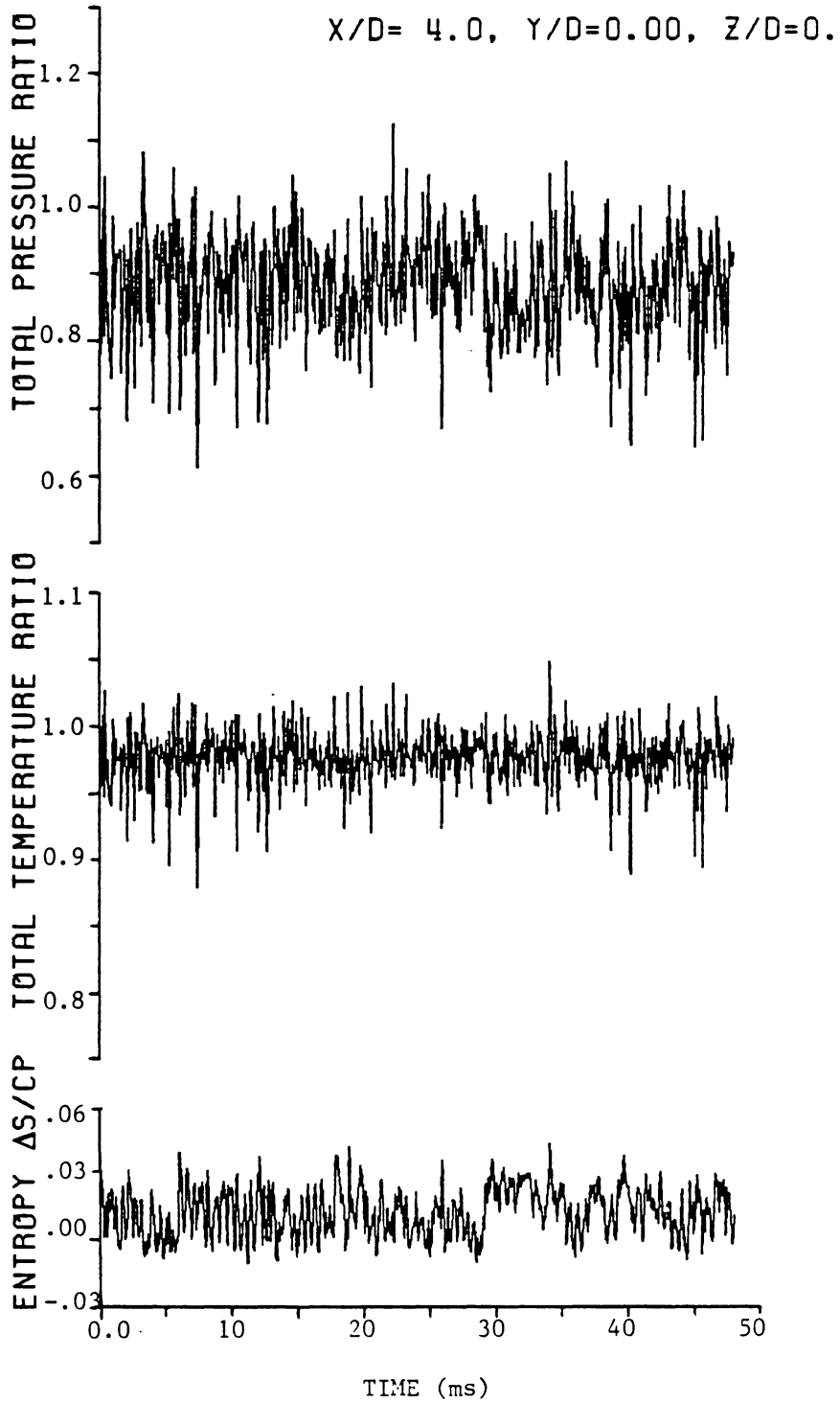

Figure 17a. Time-Resolved Stagnation Pressure, Stagnation Temperature and Entropy at X/D = 4, Y/D = 0.0, and Z/D = 0.0; Uniform Flow, Complete Time Trace.

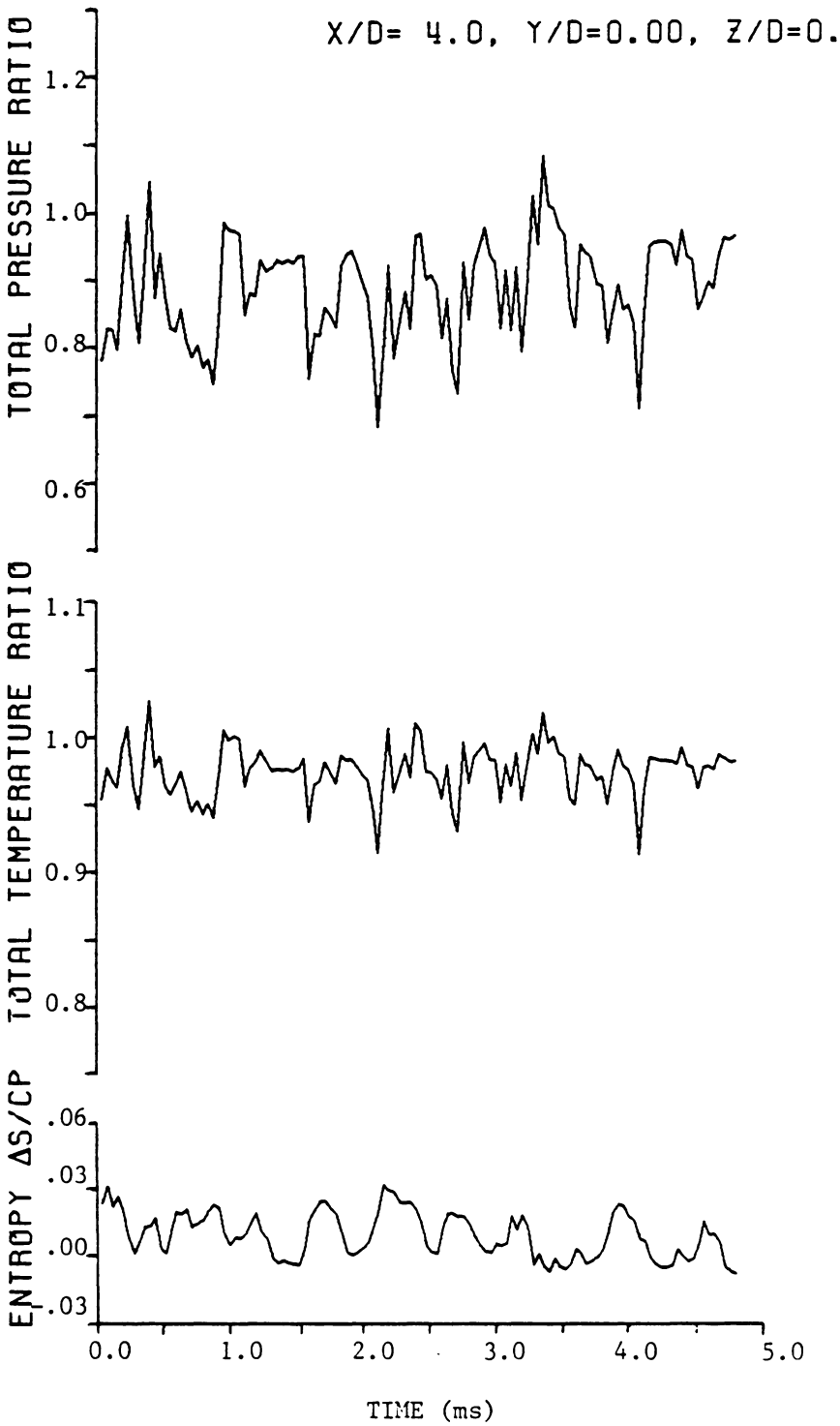

Figure 17b. Time-Resolved Stagnation Pressure, Stagnation Temperature and Entropy at X/D = 4, Y/D = 0.0, and Z/D = 0.0; Uniform Flow, Expanded Time Scale.

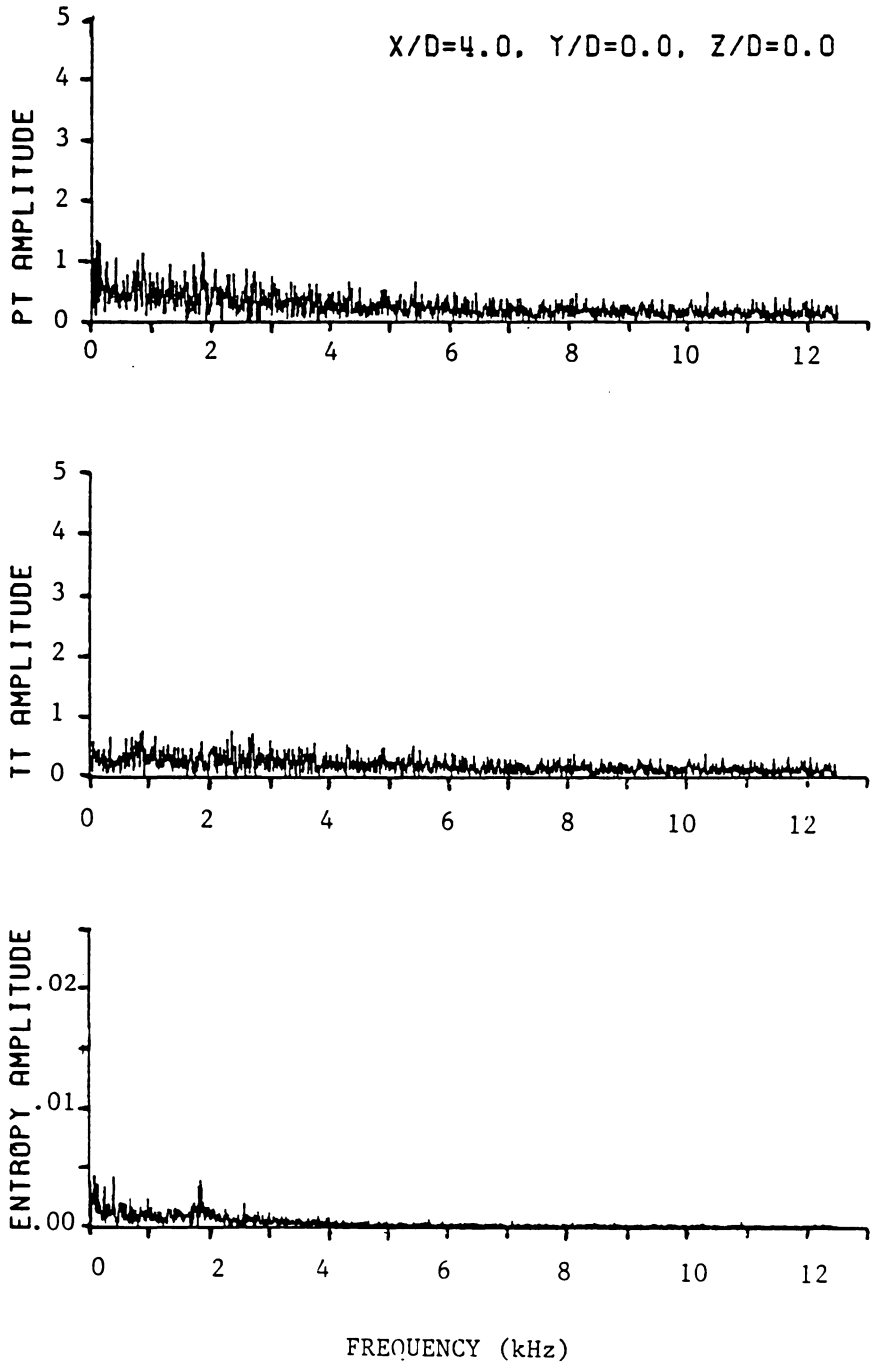

Figure 17c. Time-Resolved Stagnation Pressure, Stagnation Temperature and Entropy at X/D = 4, Y/D = 0.0, and Z/D = 0.0; Uniform Flow, Frequency Spectra.

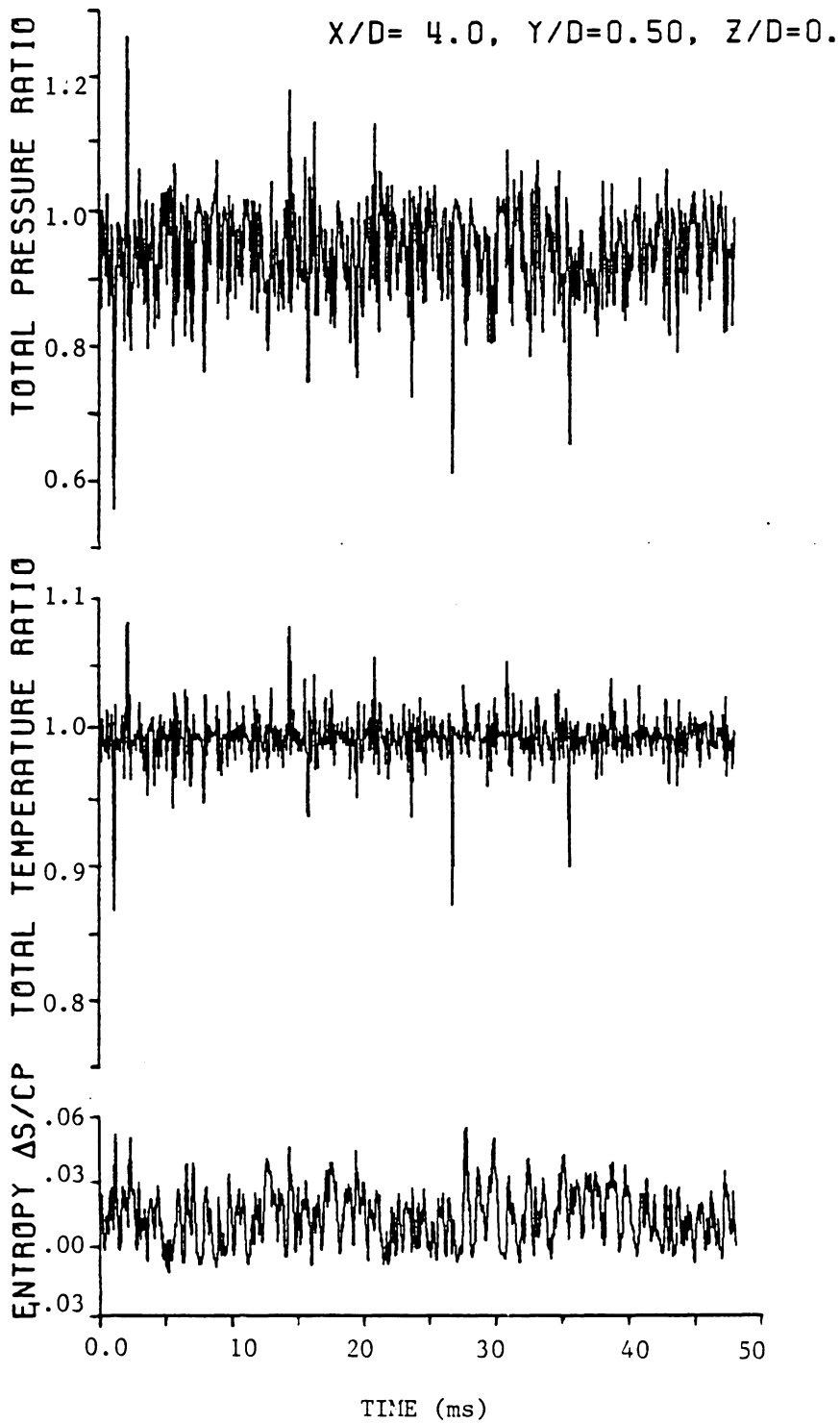

Figure 18a. Time-Resolved Stagnation Pressure, Stagnation Temperature and Entropy at X/D =4, Y/D = 0.5, and Z/D = 0.0; Uniform Flow, Complete Time Trace.

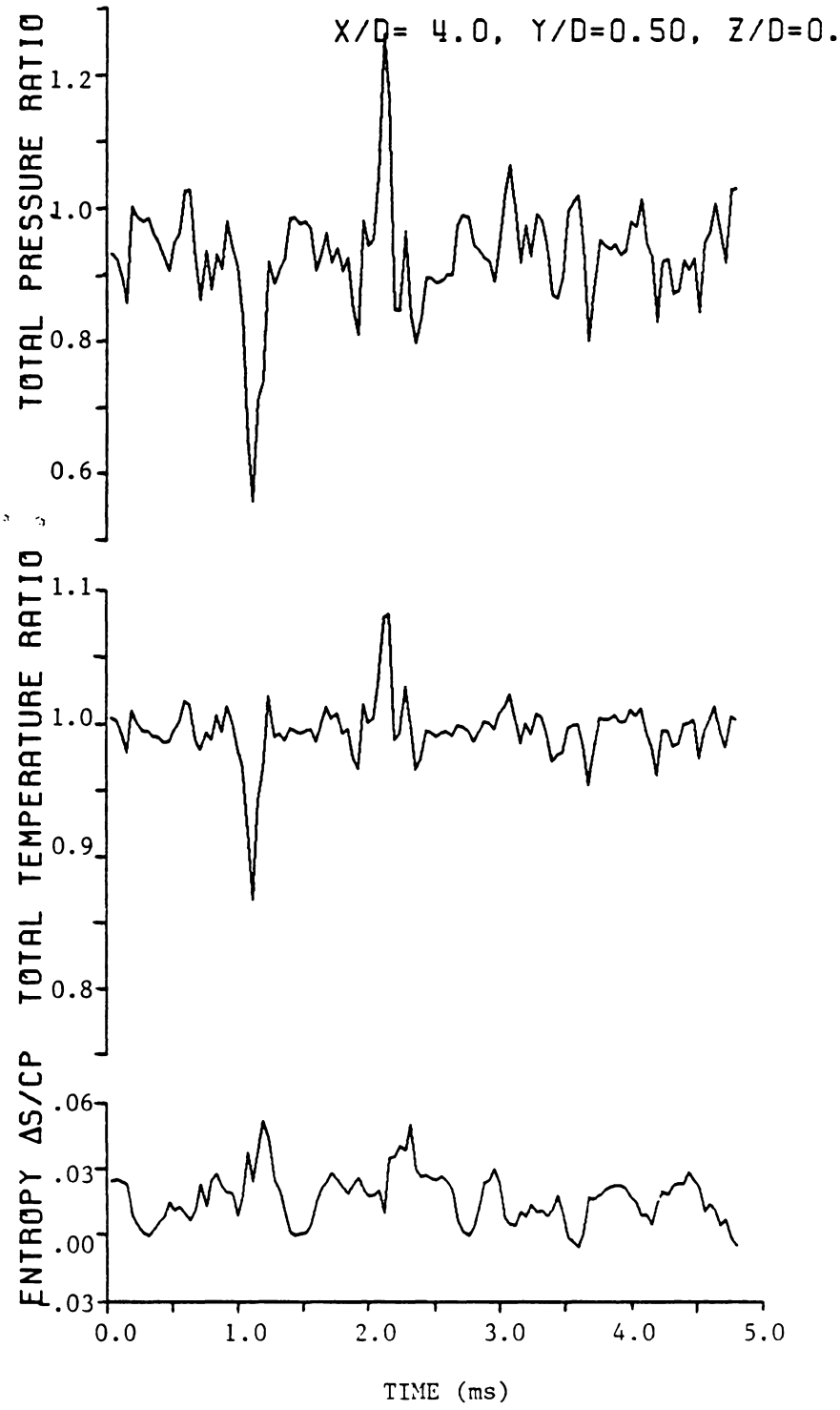

Figure 18b. Time-Resolved Stagnation Pressure, Stagnation Temperature and Entropy at X/D = 4, Y/D = 0.5, and Z/D = 0.0; Uniform Flow, Expanded Time Scale.

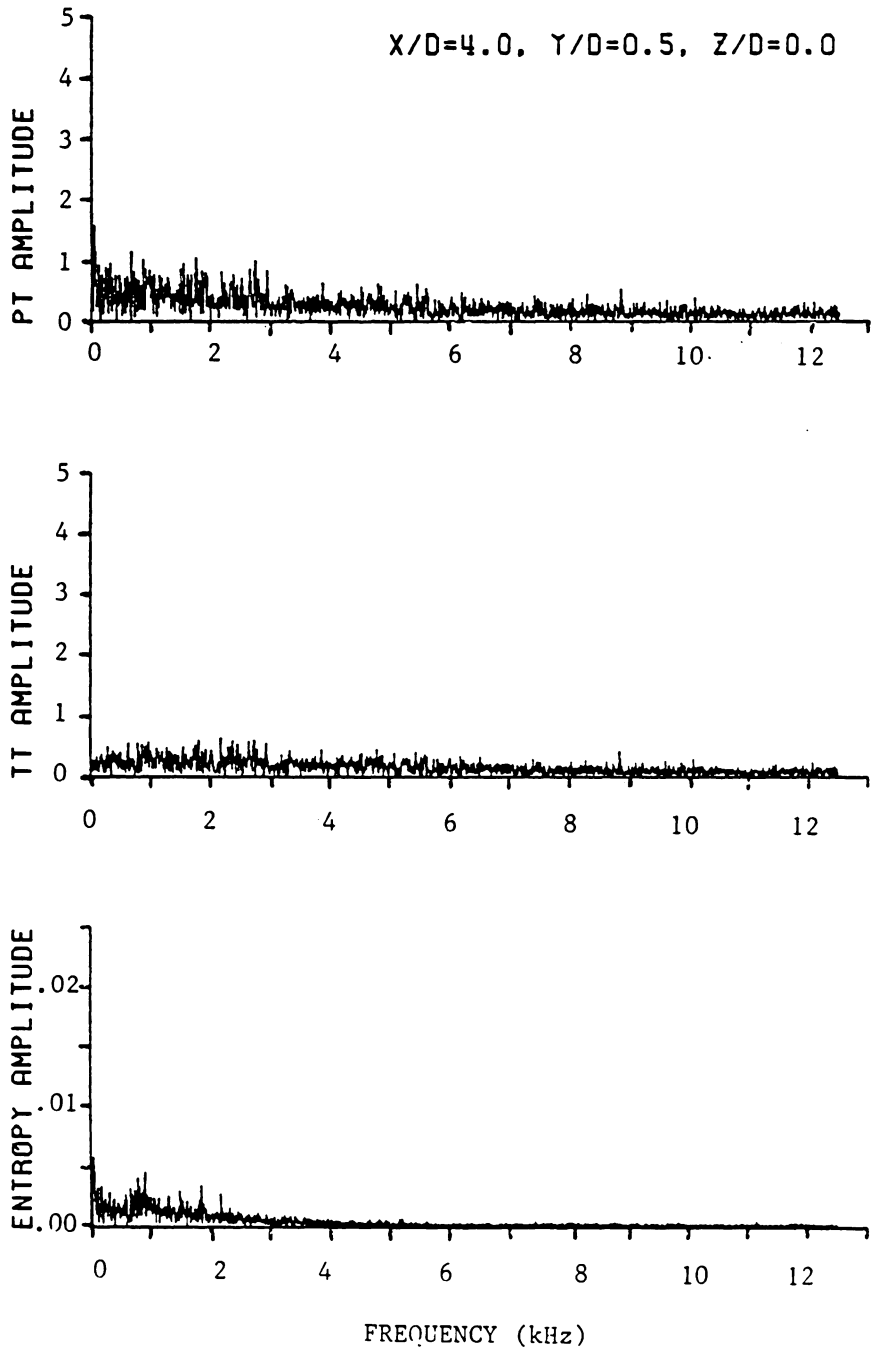

Figure 18c. Time-Resolved Stagnation Pressure, Stagnation Temperature and Entropy at X/D = 4, Y/D = 0.5, and Z/D = 0.0; Uniform Flow, Frequency Spectra.

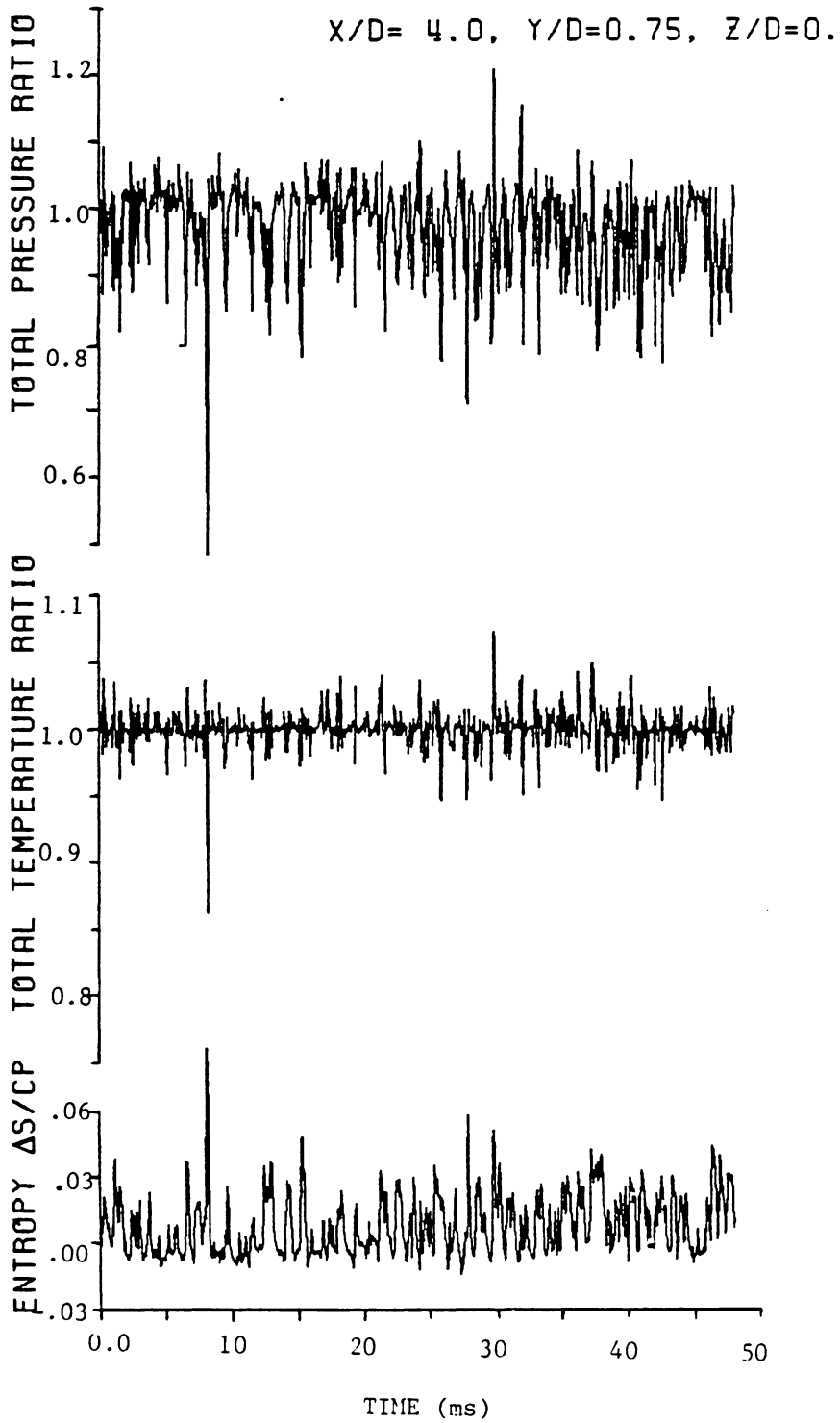

Figure 19a. Time-Resolved Stagnation Pressure, Stagnation Temperature and Entropy at X/D = 4, Y/D = 0.75, Z/D = 0.0; Uniform Flow, Complete Time Trace.

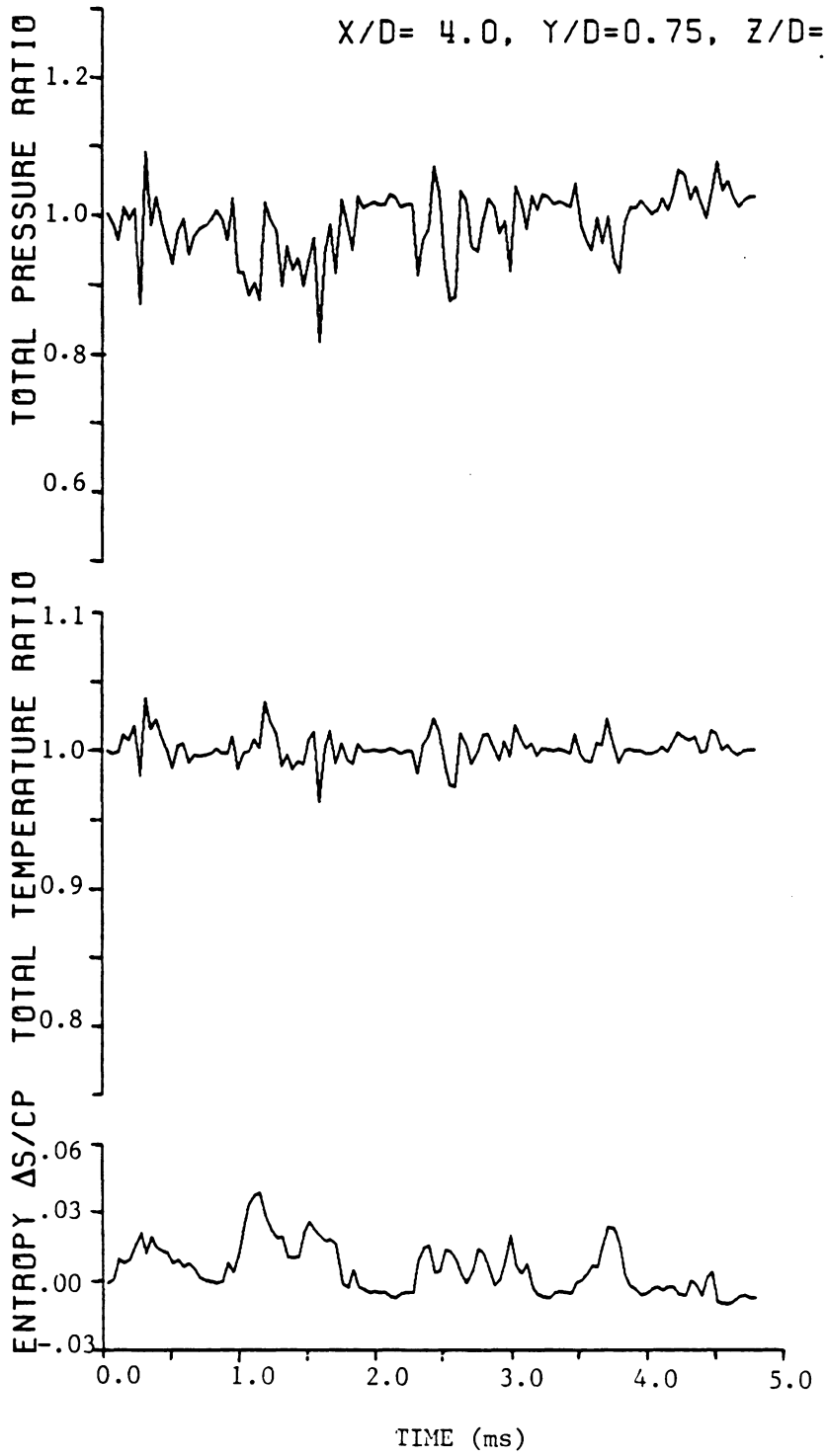

Figure 19b. Time-Resolved Stagnation Pressure, Stagnation Temperature and Entropy at X/D = 4, Y/D = 0.75, and Z/D = 0.0; Uniform Flow, Expanded Time Scale.

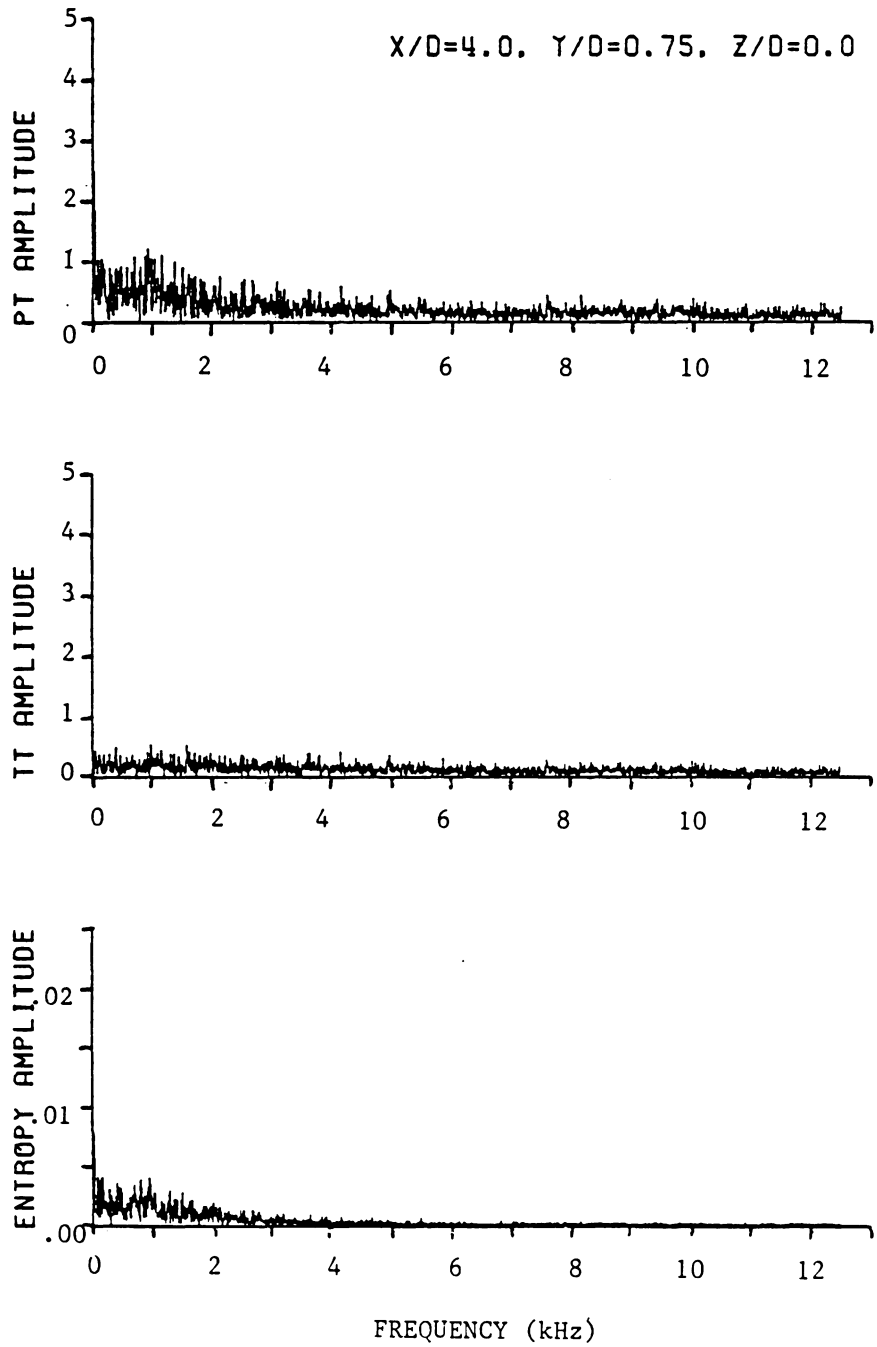

Figure 19c. Time-Resolved Stagnation Pressure, Stagnation Temperature and Entropy at X/D = 4, Y/D = 0.75, and Z/D = 0.0; Uniform Flow, Frequency Spectra.

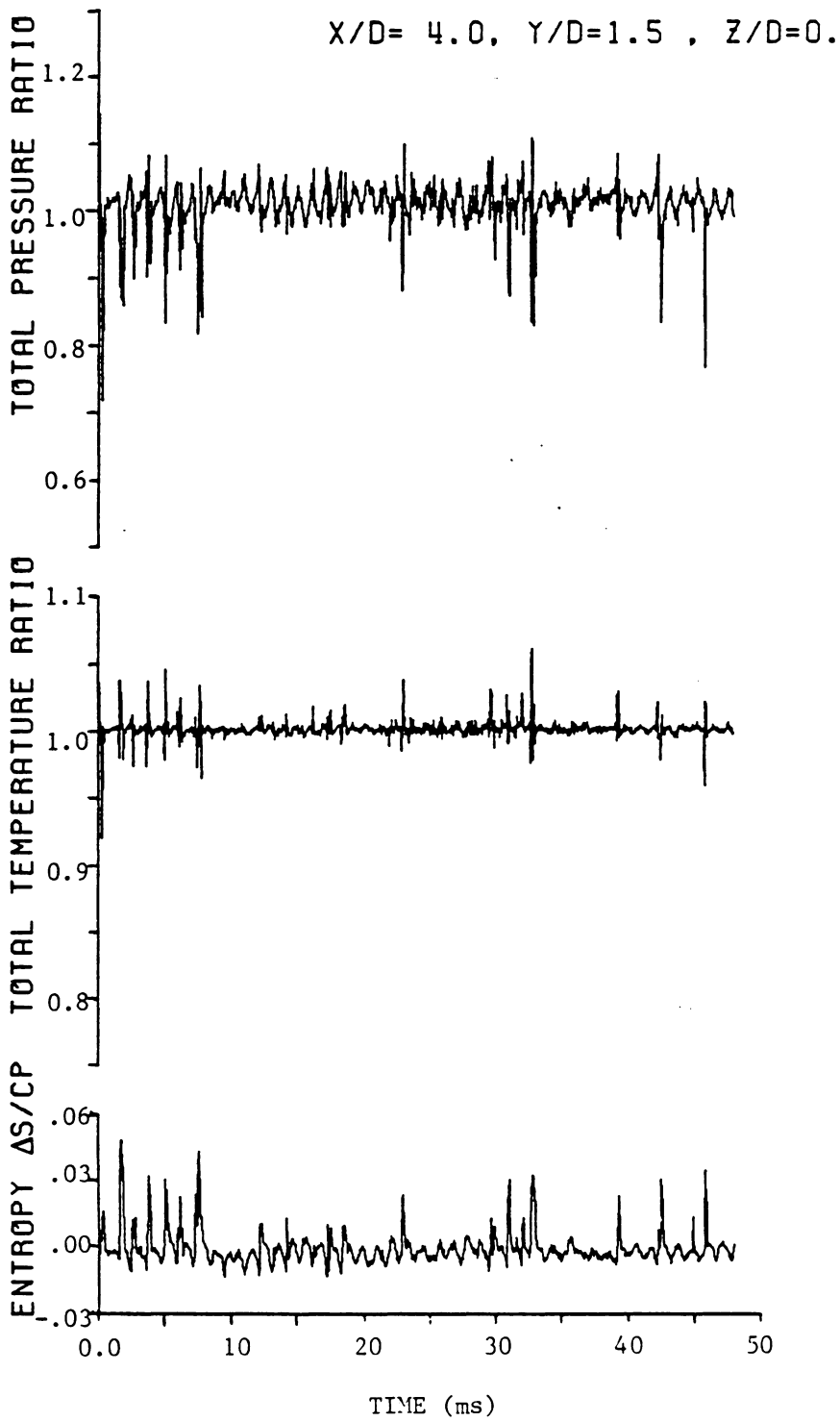

Figure 20a. Time-Resolved Stagnation Pressure, Stagnation Temperature and Entropy at X/D = 4, Y/D = 1.5, and Z/D = 0.0; Uniform Flow, Complete Time Trace.

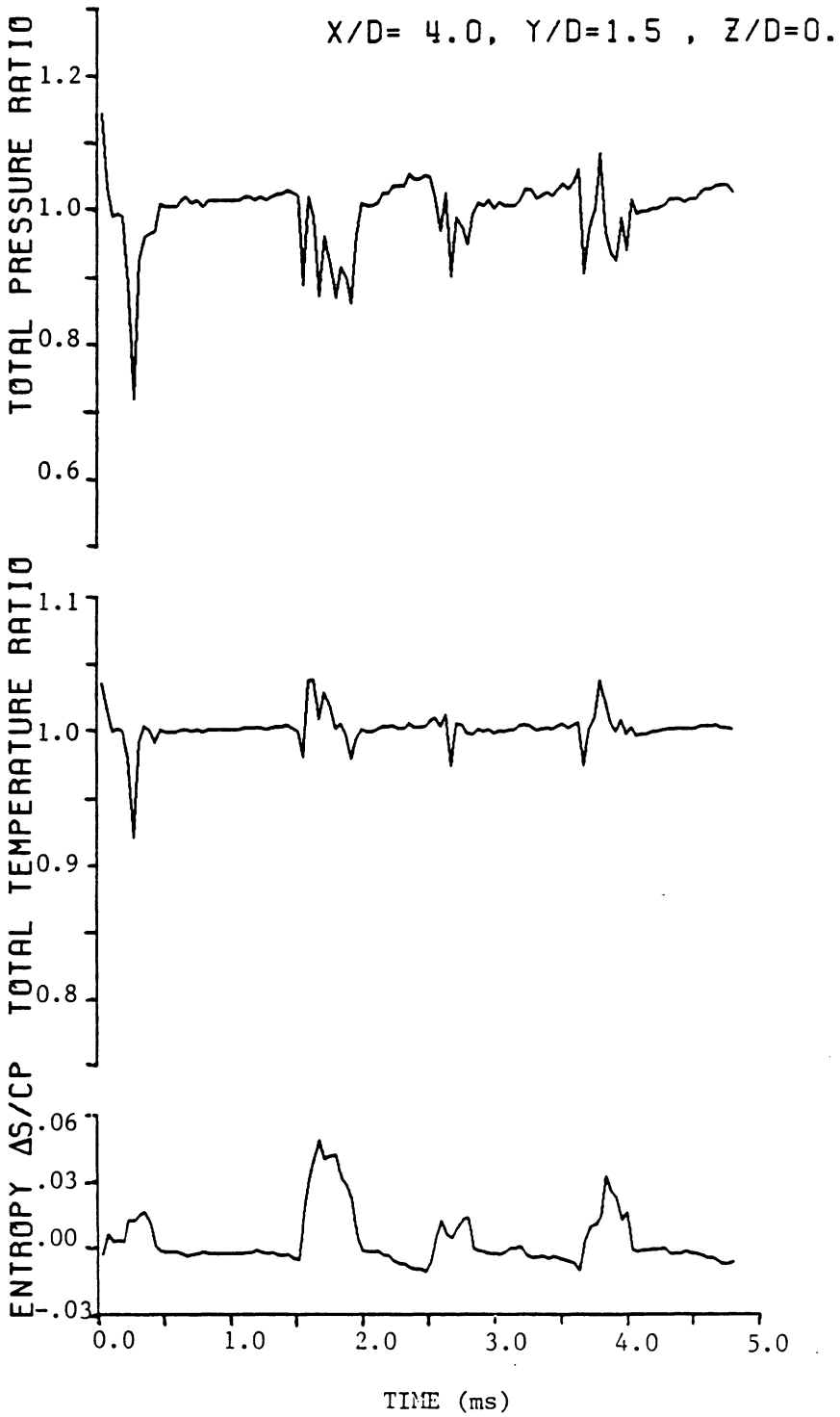

Figure 20b. Time-Resolved Stagnation Pressure, Stagnation Temperature and Entropy at X/D = 4, Y/D = 1.5, and Z/D = 0.0; Uniform Flow, Expanded Time Scale.

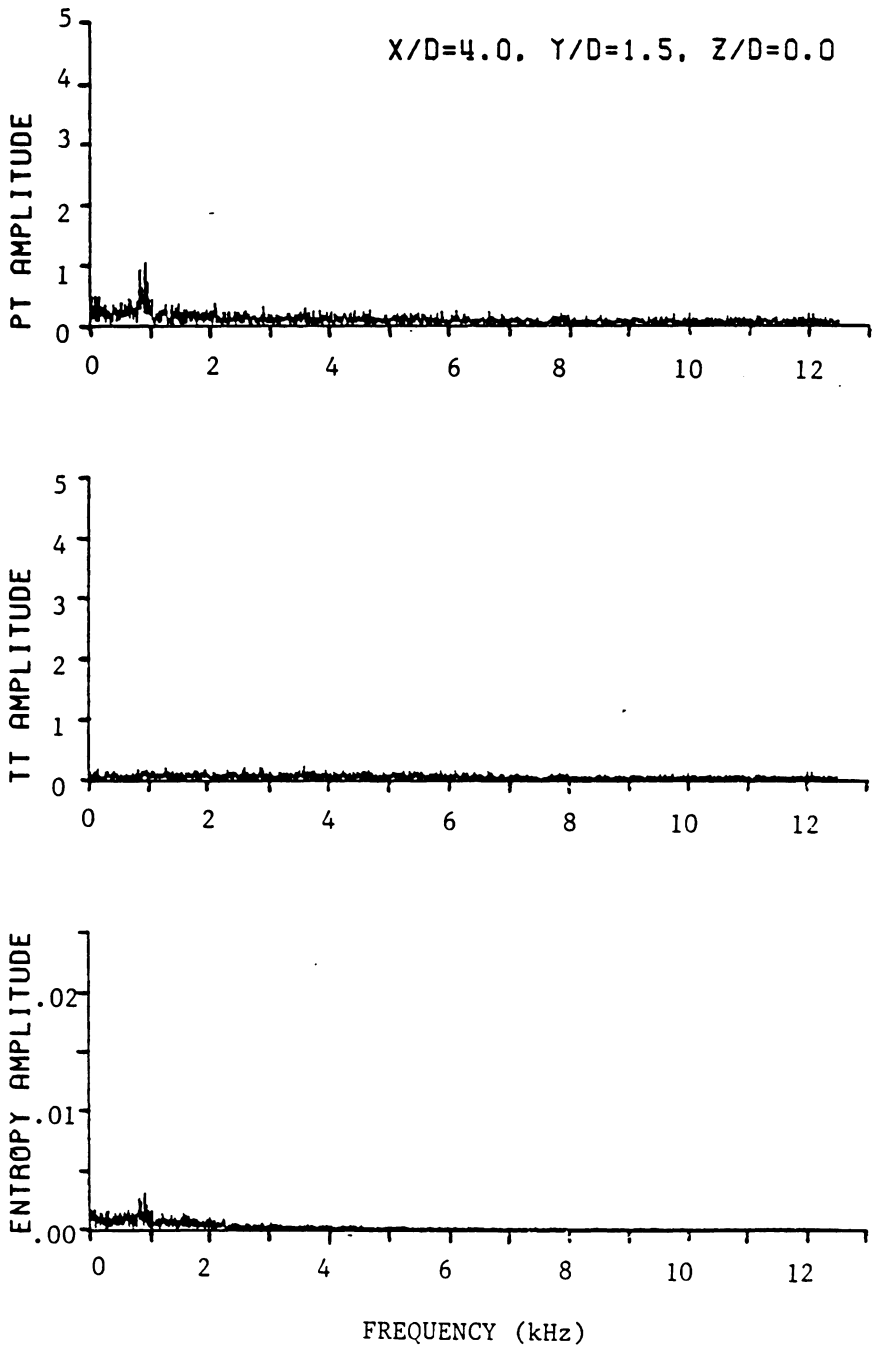

Figure 20c. Time-Resolved Stagnation Pressure, Stagnation Temperature and Entropy at X/D = 4, Y/D = 1.5, and Z/D = 0.0; Uniform Flow, Frequency Spectra.

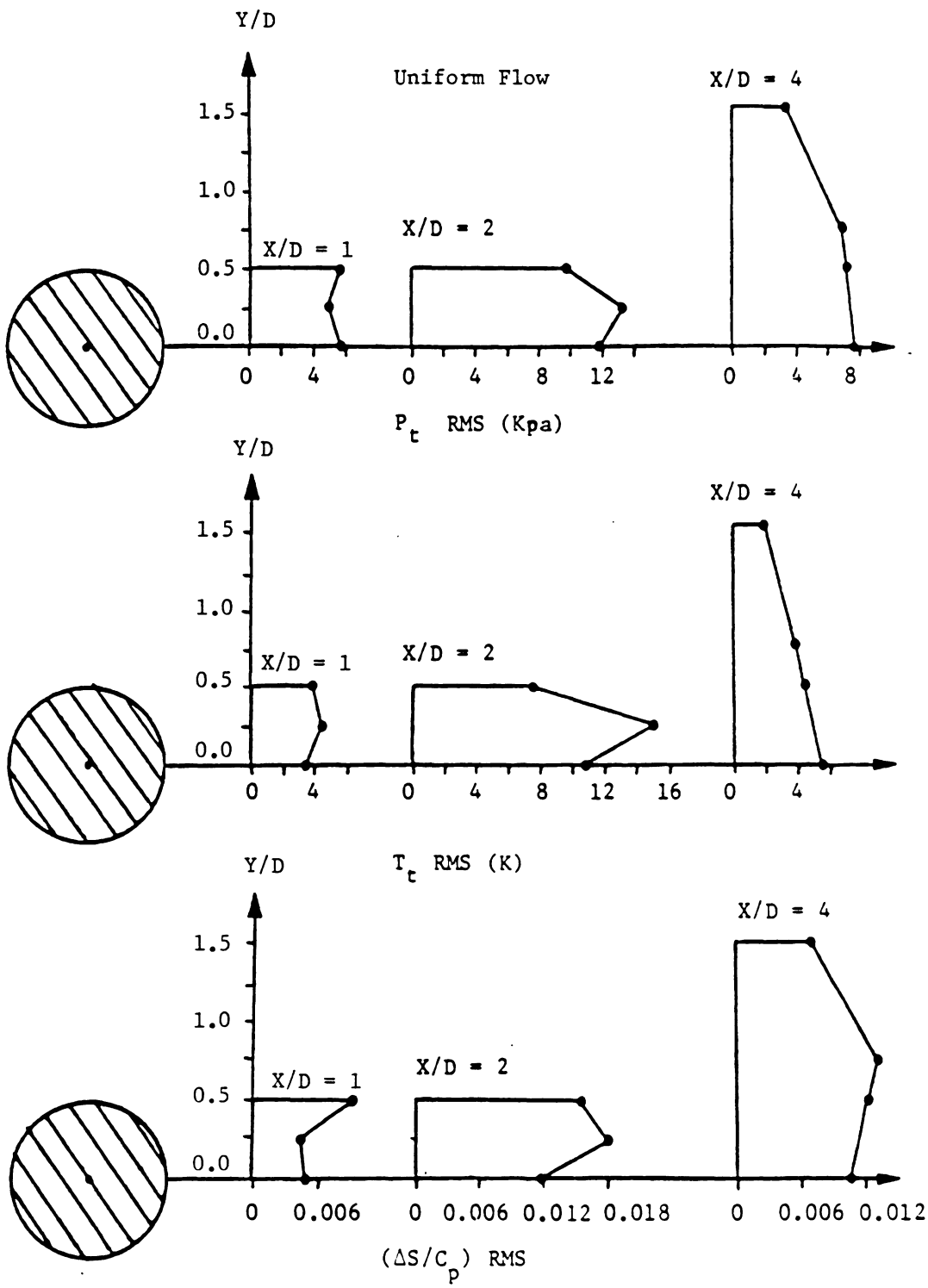

Figure 21. Root-Mean-Square (RMS) Values of the Stagnation Pressure, Stagnation Temperature and Nondimensionalized Entropy ($\Delta S/C_p$) at X/D = 1,2, and 4; uniform flow.

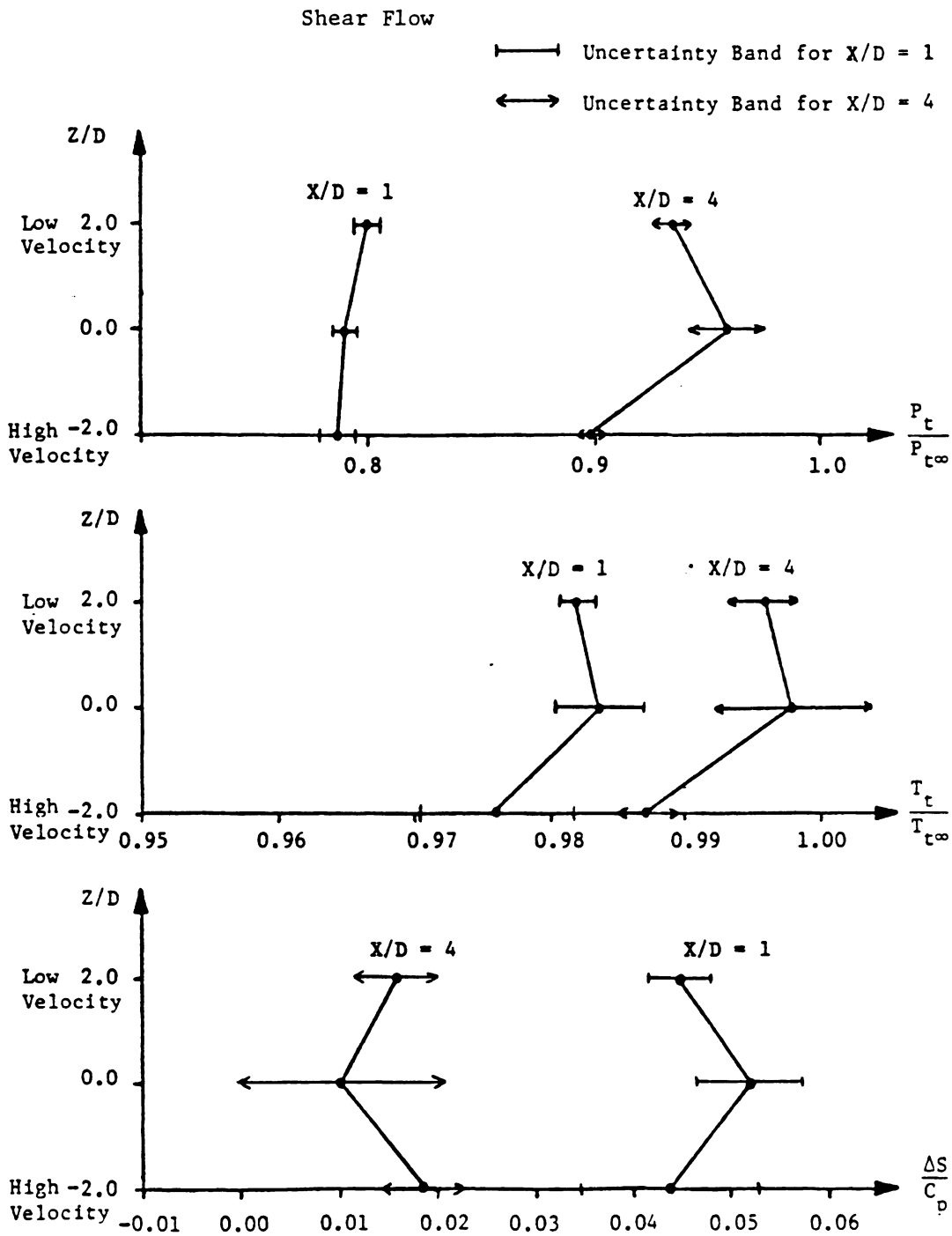

Figure 22. dc-Values for the Nondimensionalized Stagnation Pressure ($P_t/P_{t\infty}$), Stagnation Temperature ($T_t/T_{t\infty}$) and entropy ($\Delta S/C_p$) at X/D = 1 and 4; shear flow.

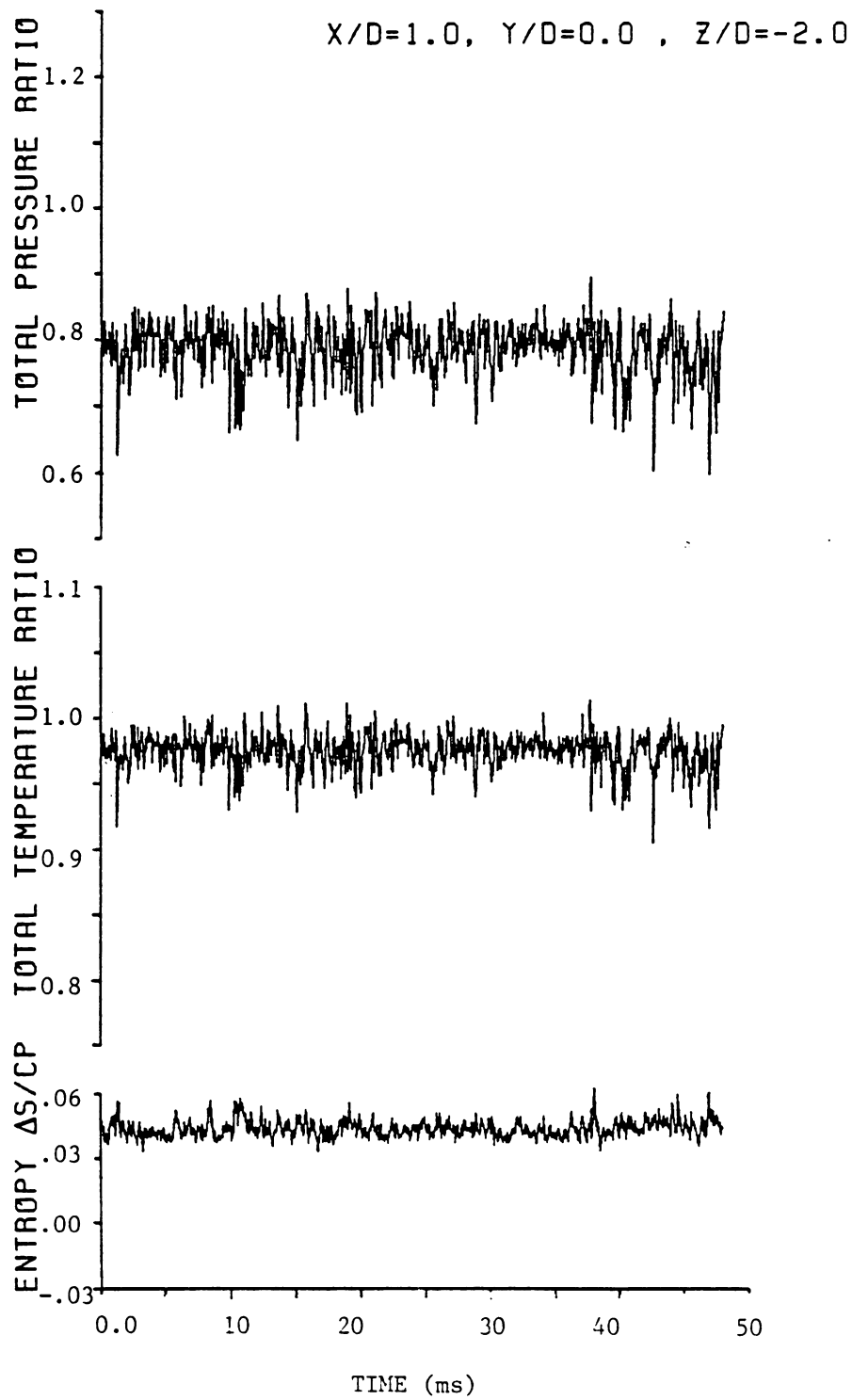

Figure 23a. Time-Resolved Stagnation Pressure, Stagnation Temperature and Entropy of X/D = 1.0, Y/D = 0.0 and Z/D = -2.0; shear flow, Complete Time Trace.

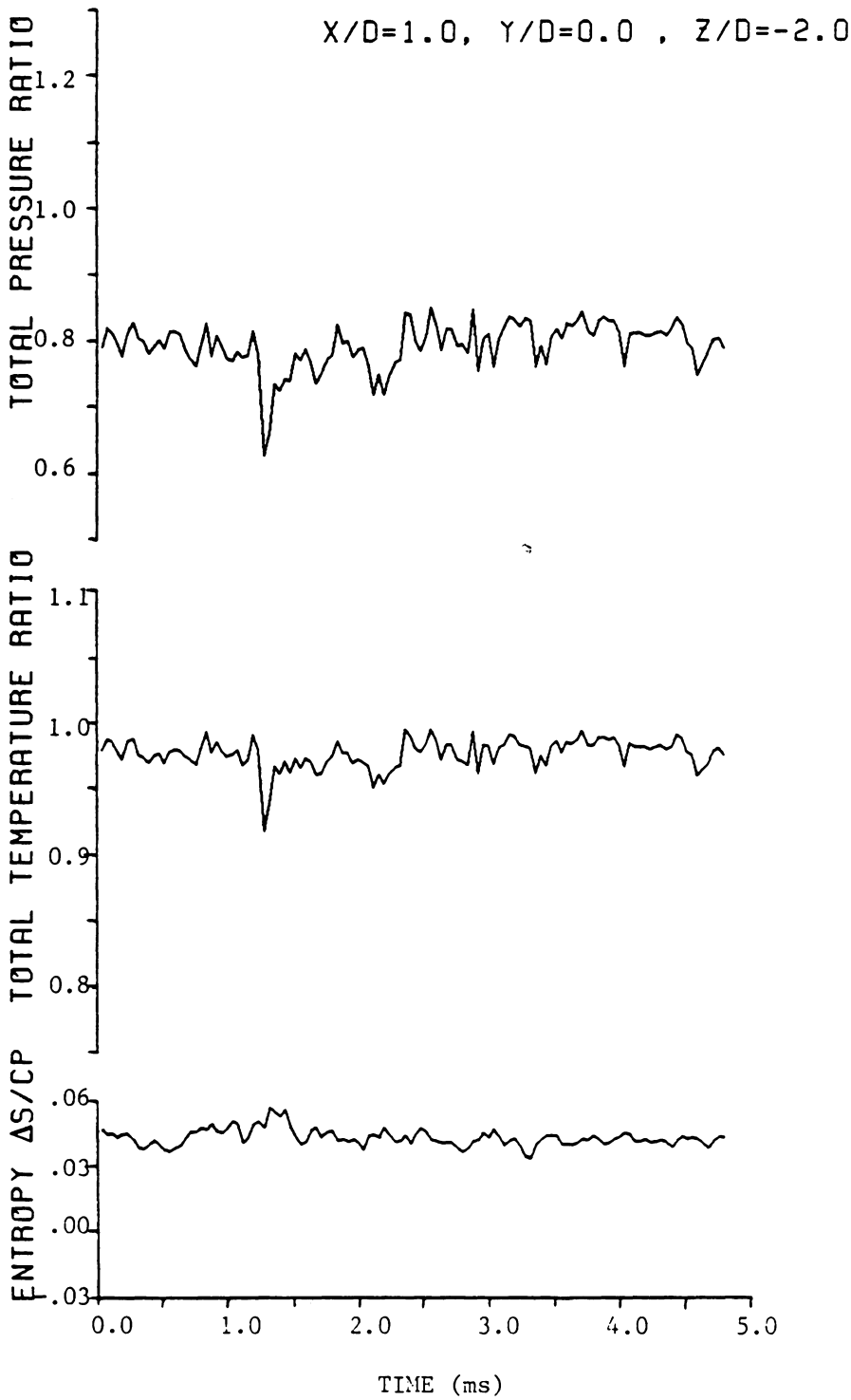

Figure 23b. Time-Resolved Stagnation Pressure, Stagnation Temperature and Entropy at X/D = 1.0, Y/D = 0.0, and Z/D = -2.0; Shear Flow, Expanded Time Scale.

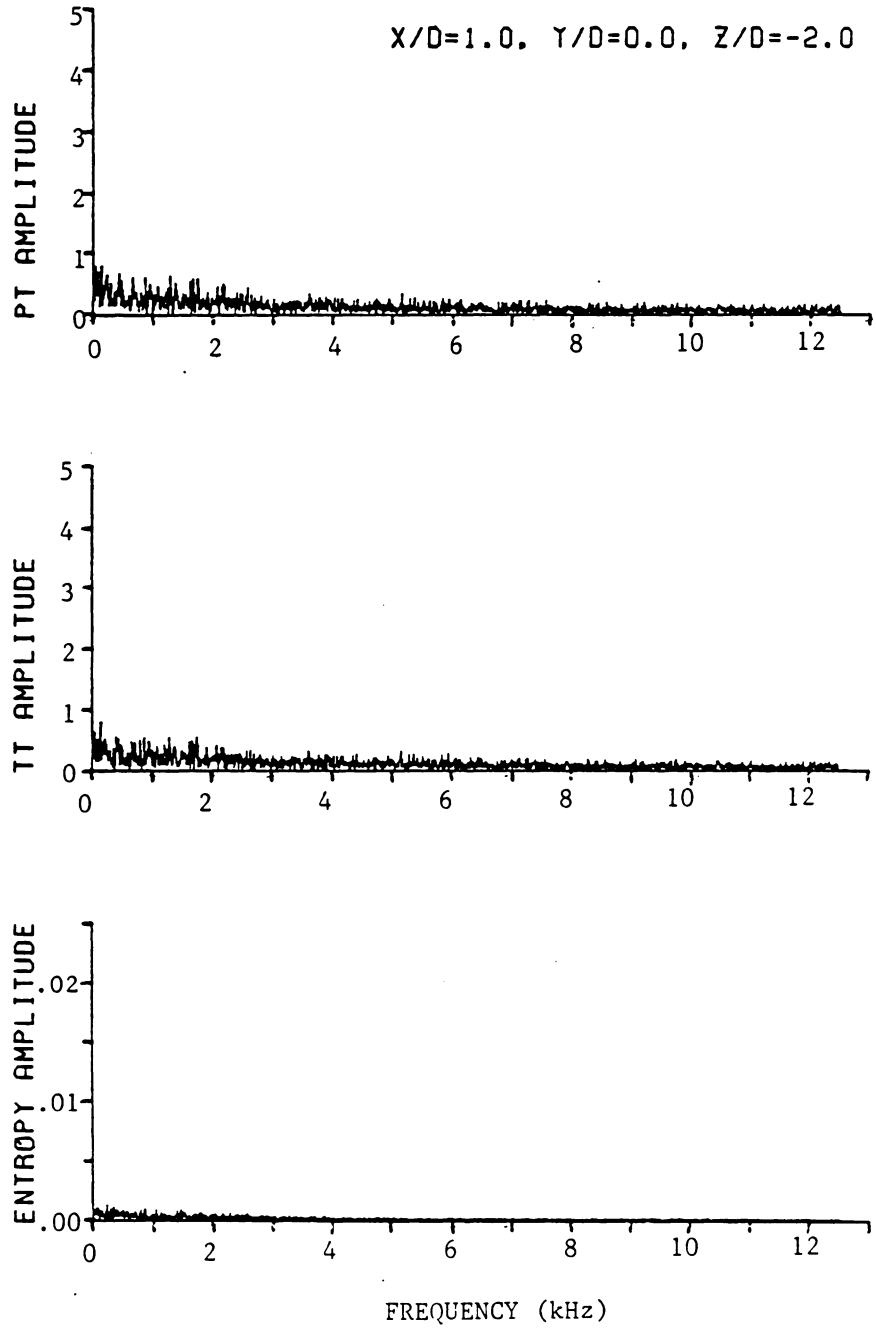

Figure 23c. Time-Resolved Stagnation Pressure, Stagnation Temperature and Entropy at X/D = 1.0, Y/D = 0.0 and Z/D = -2.0; Shear Flow, Frequency Spectra.

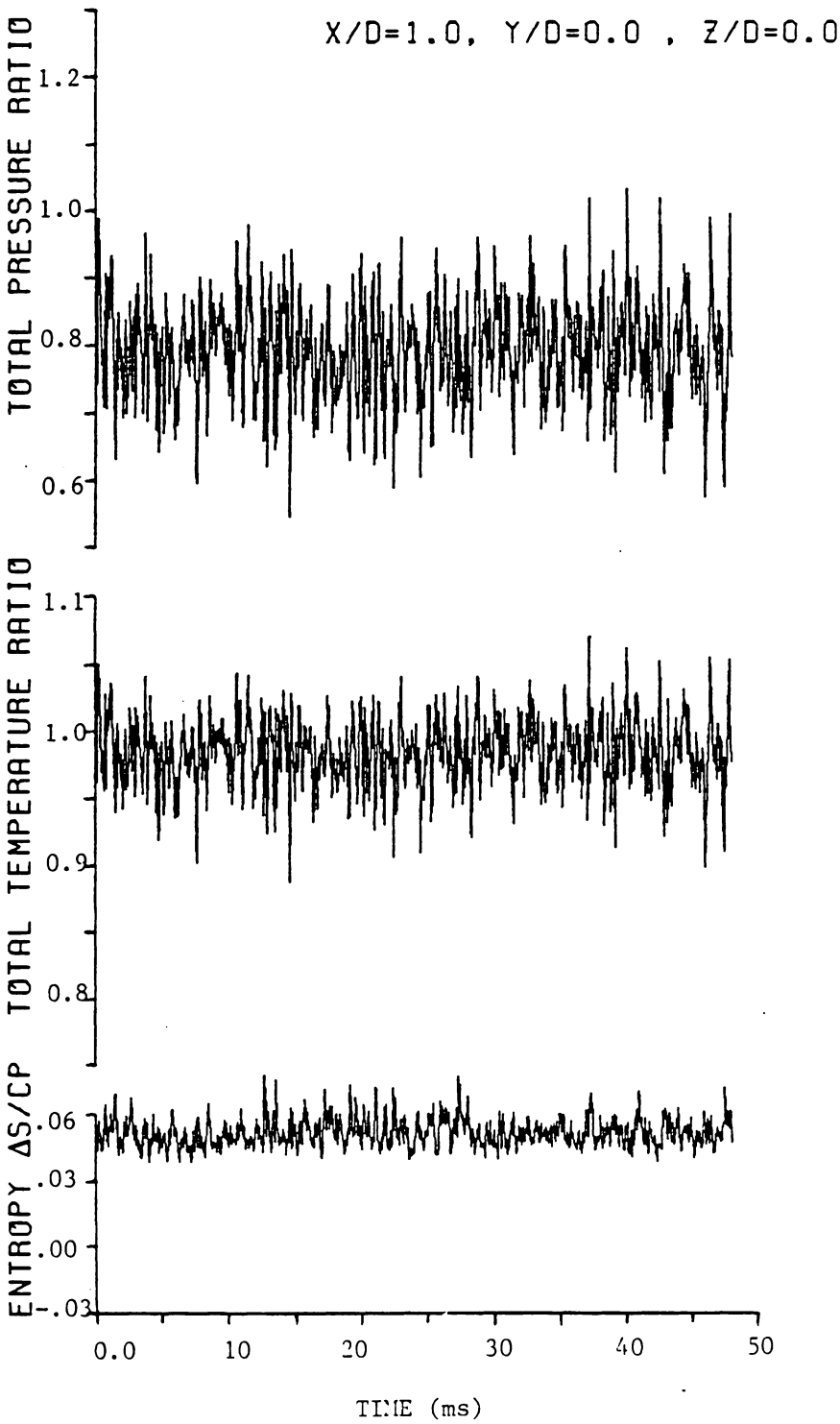

Figure 24a. Time-Resolved Stagnation Pressure, Stagnation Temperature and Entropy at X/D = 1.0, Y/D = 0.0 and Z/D = 0.0; Shear Flow, Complete Time Trace.

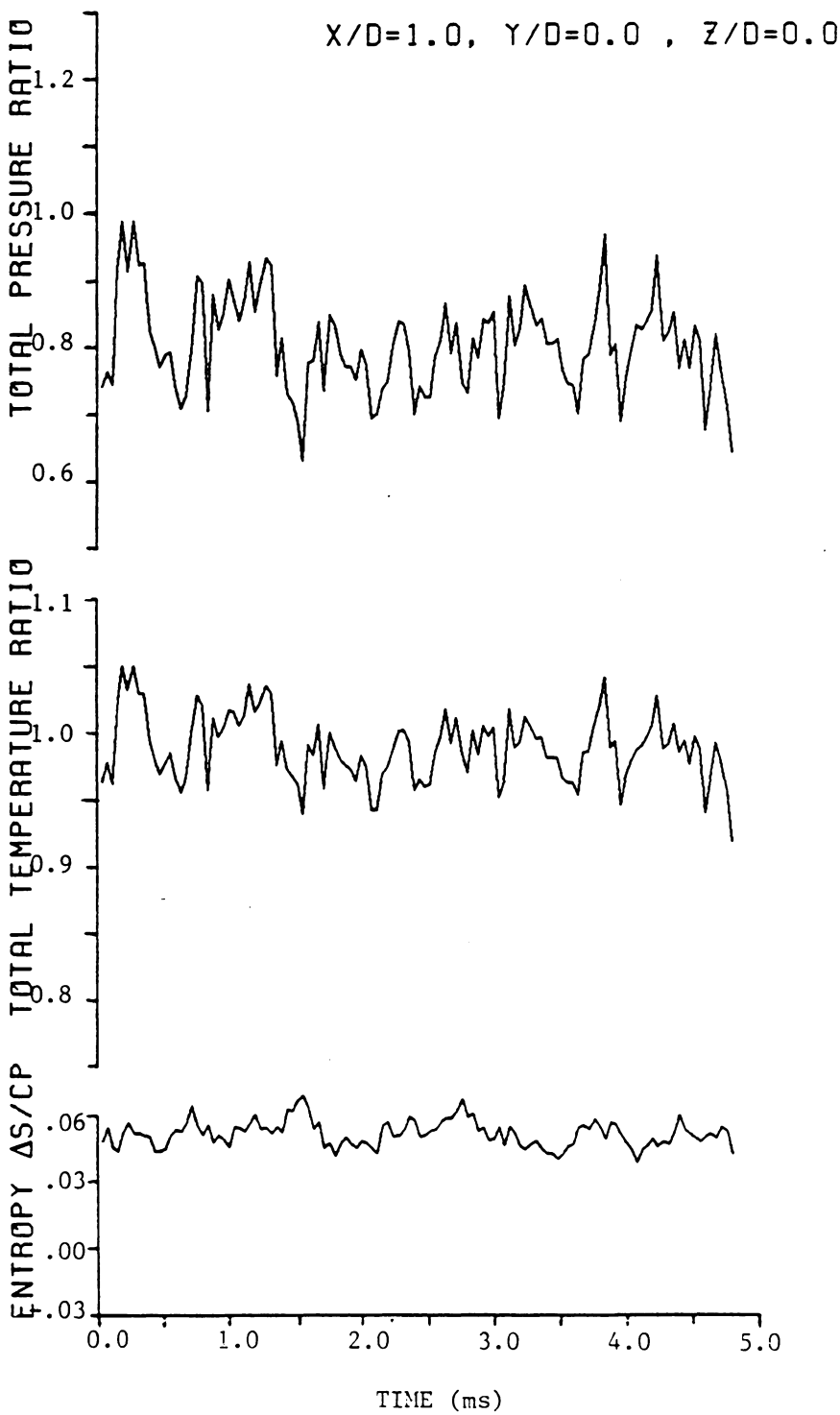

Figure 24b. Time-Resolved Stagnation Pressure, Stagnation Temperature and Entropy at X/D = 1.0, Y/D = 0.0 and Z/D = 0.0; Shear Flow, Expanded Time Scale.

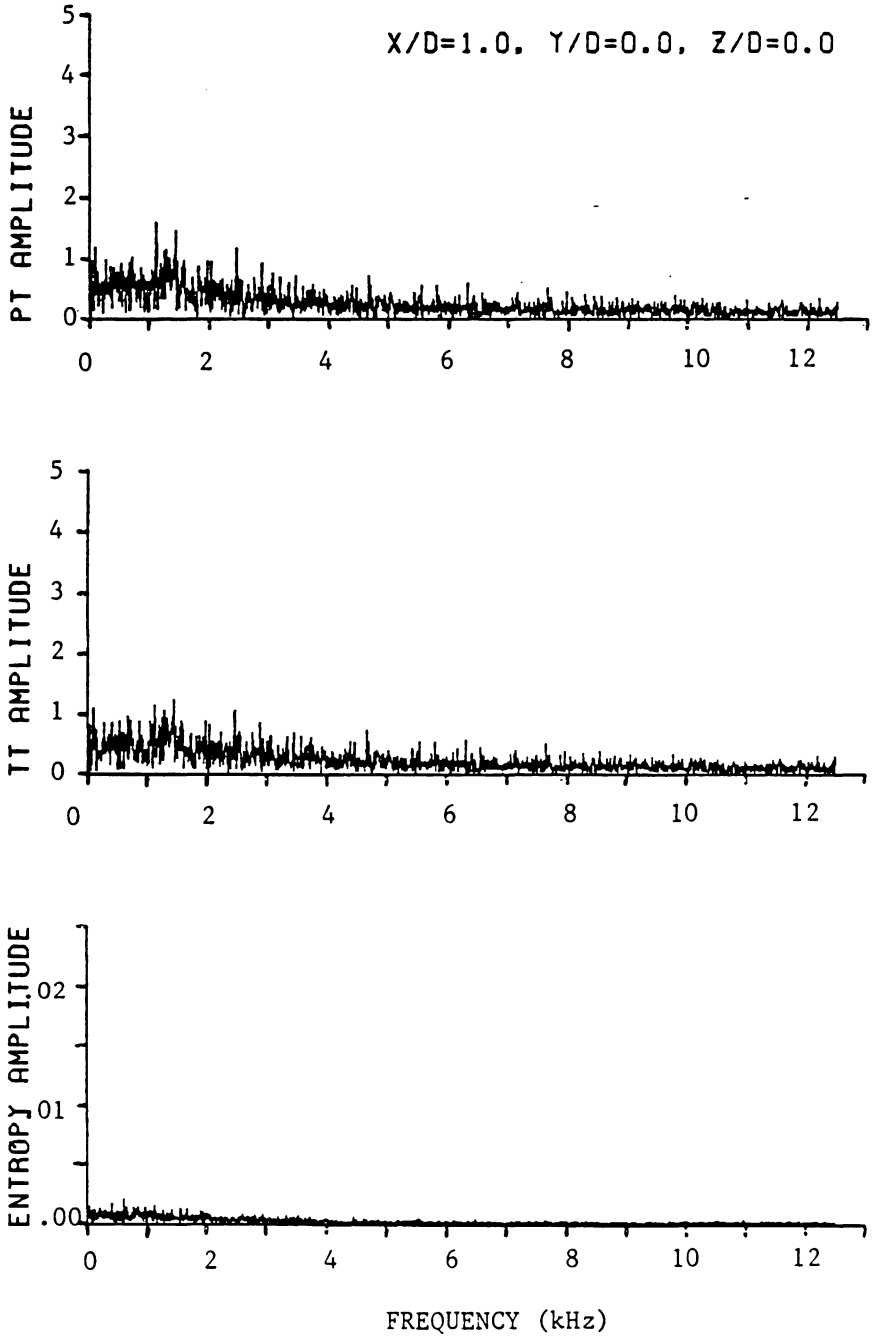

Figure 24c. Time-Resolved Stagnation Pressure, Stagnation Temperature and Entropy at X/D = 1.0, Y/D = 0.0 and Z/D = 0.0; Shear Flow, Frequency Spectra.

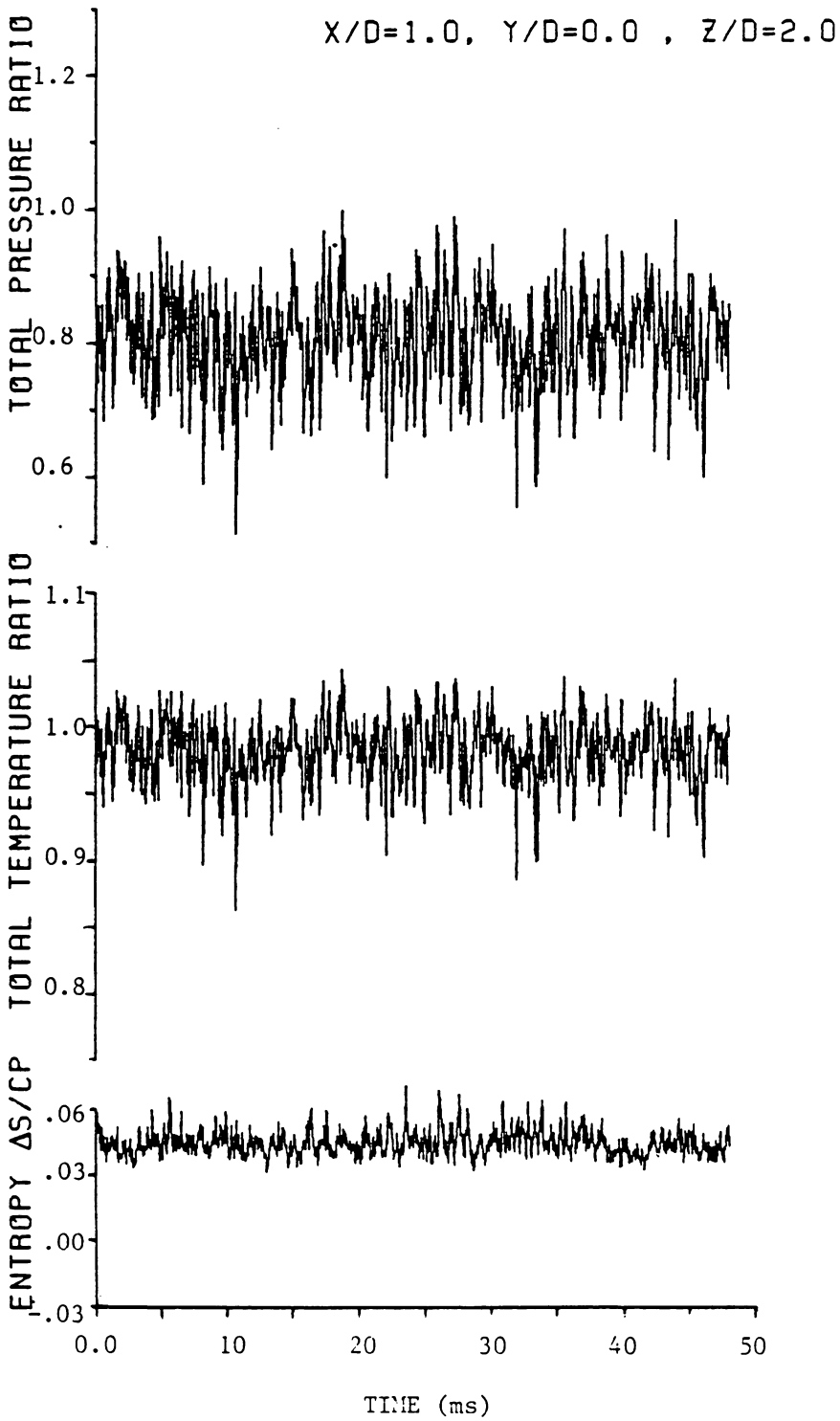

Figure 25a. Time-Resolved Stagnation Pressure, Stagnation Temperature and Entropy at X/D = 1.0, Y/D = 0.0, Z/D = 2.0; Shear Flow, Complete Time Trace.

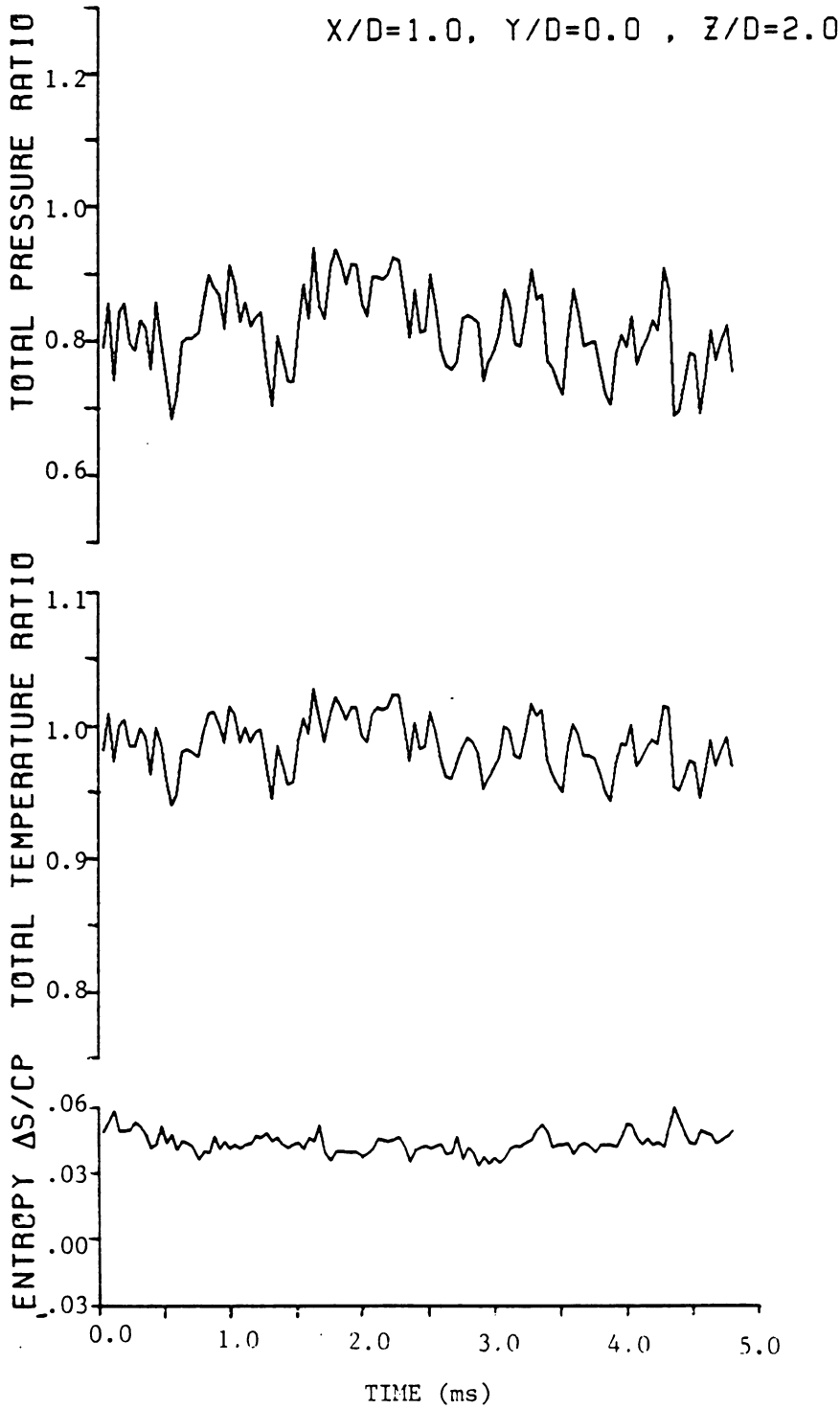

Figure 25b. Time-Resolved Stagnation Pressure, Stagnation Temperature and Entropy at X/D = 1.0, Y/D = 0.0 and Z/D = 2.0; Shear Flow, Expanded Time Scale.

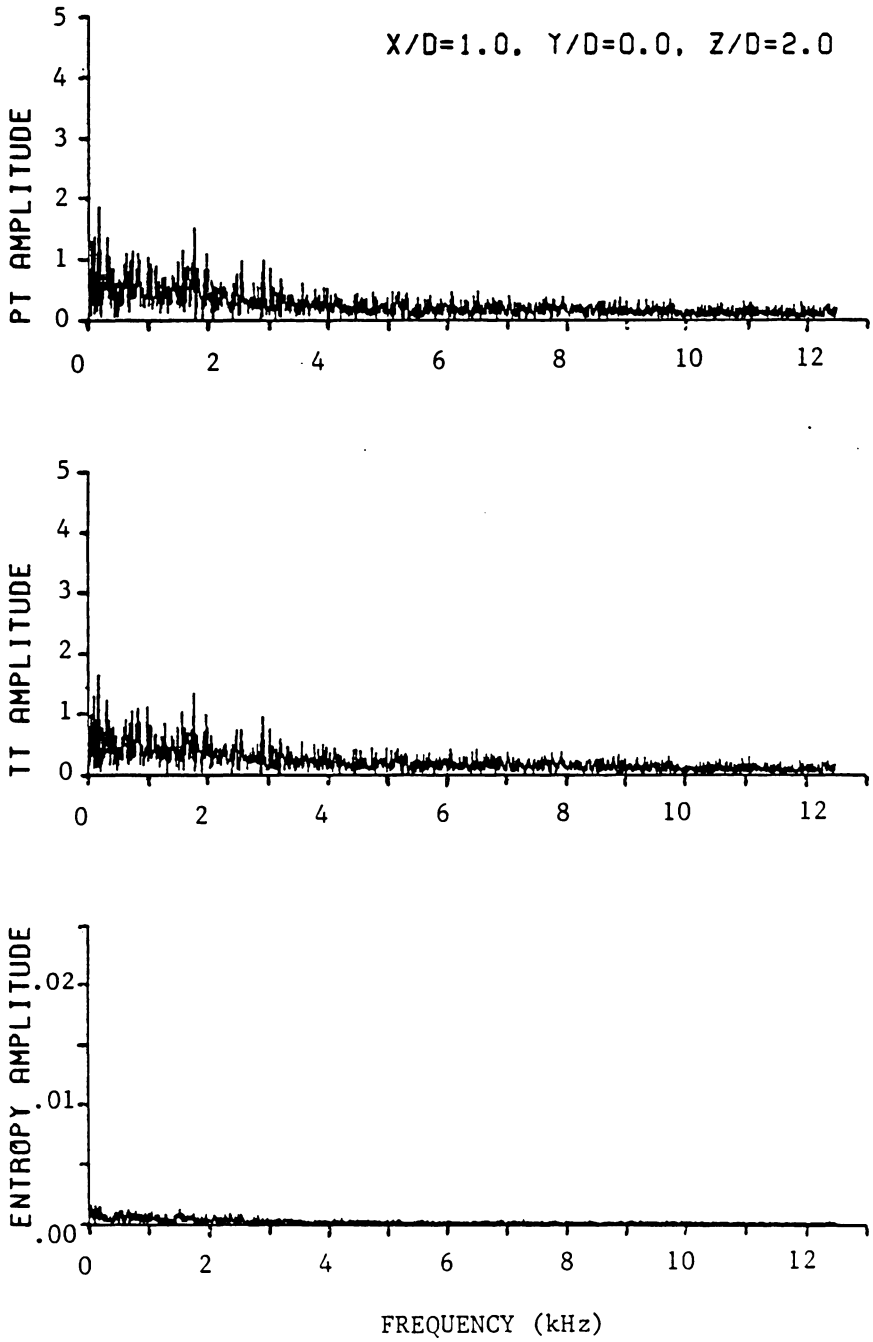

Figure 25c. Time-Resolved Stagnation Pressure, Stagnation Temperature and Entropy at X/D = 1.0, Y/D = 0.0 and Z/D = 2.0; Shear Flow, Frequency Spectra.

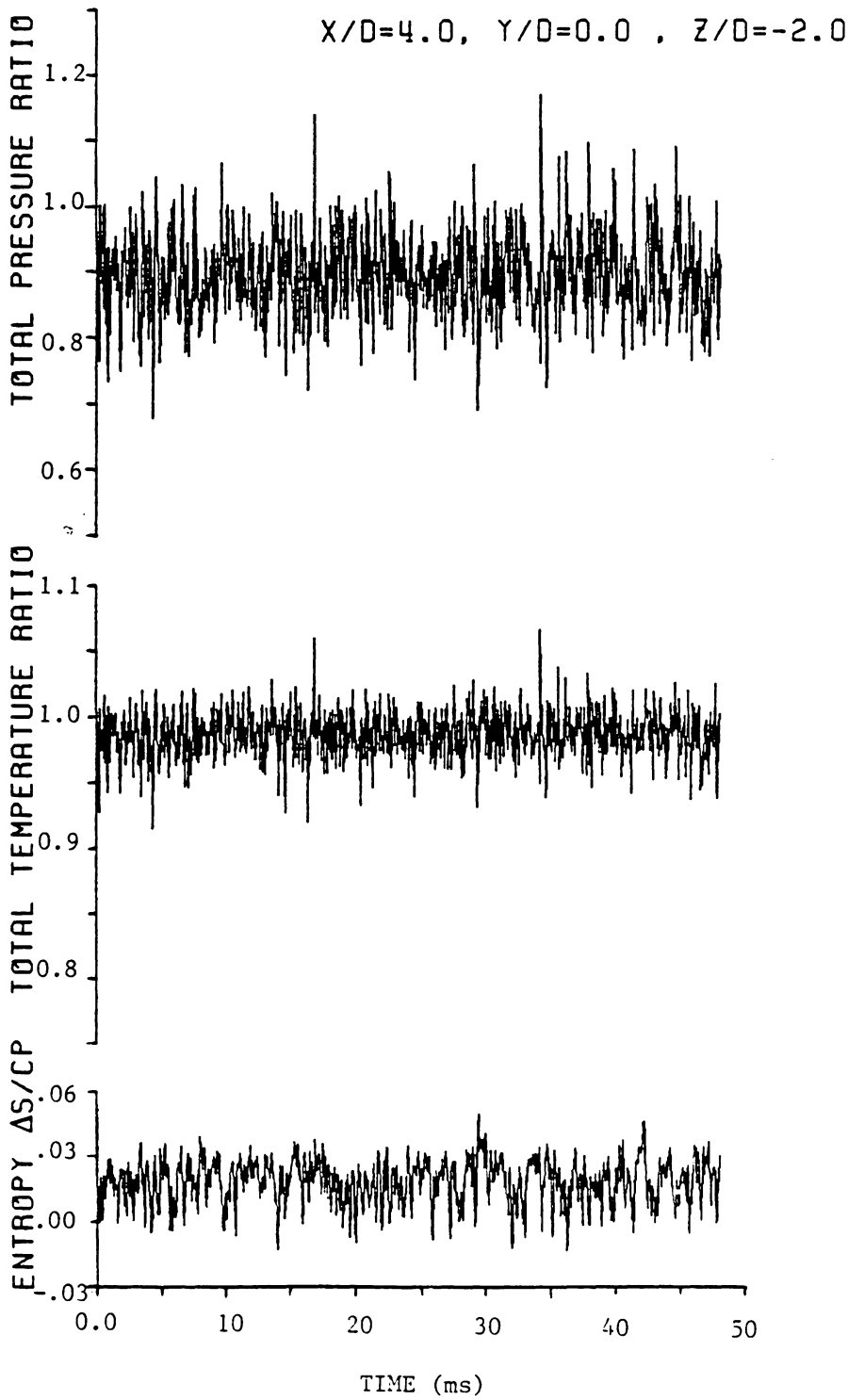

Figure 26a. Time-Resolved Stagnation Pressure, Stagnation Temperature and Entropy at X/D = 4, Y/D = 0.0 and Z/D = -2.0; Shear Flow, Complete Time Trace.

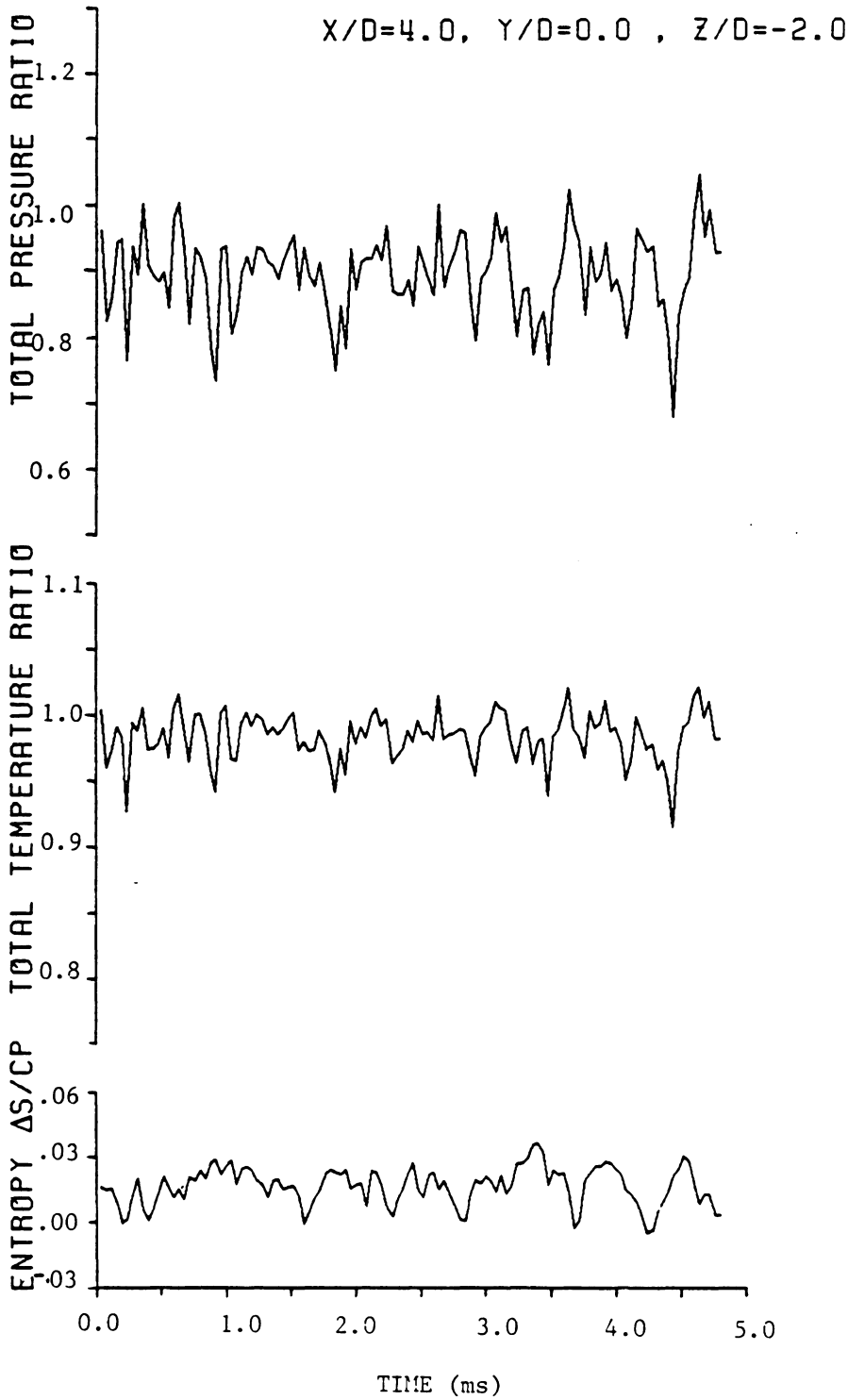

Figure 26b. Time-Resolved Stagnation Pressure, Stagnation Temperature and Entropy at X/D = 4, Y/D = 0.0 and Z/D = -2.0; Shear Flow, Expanded Time Scale.

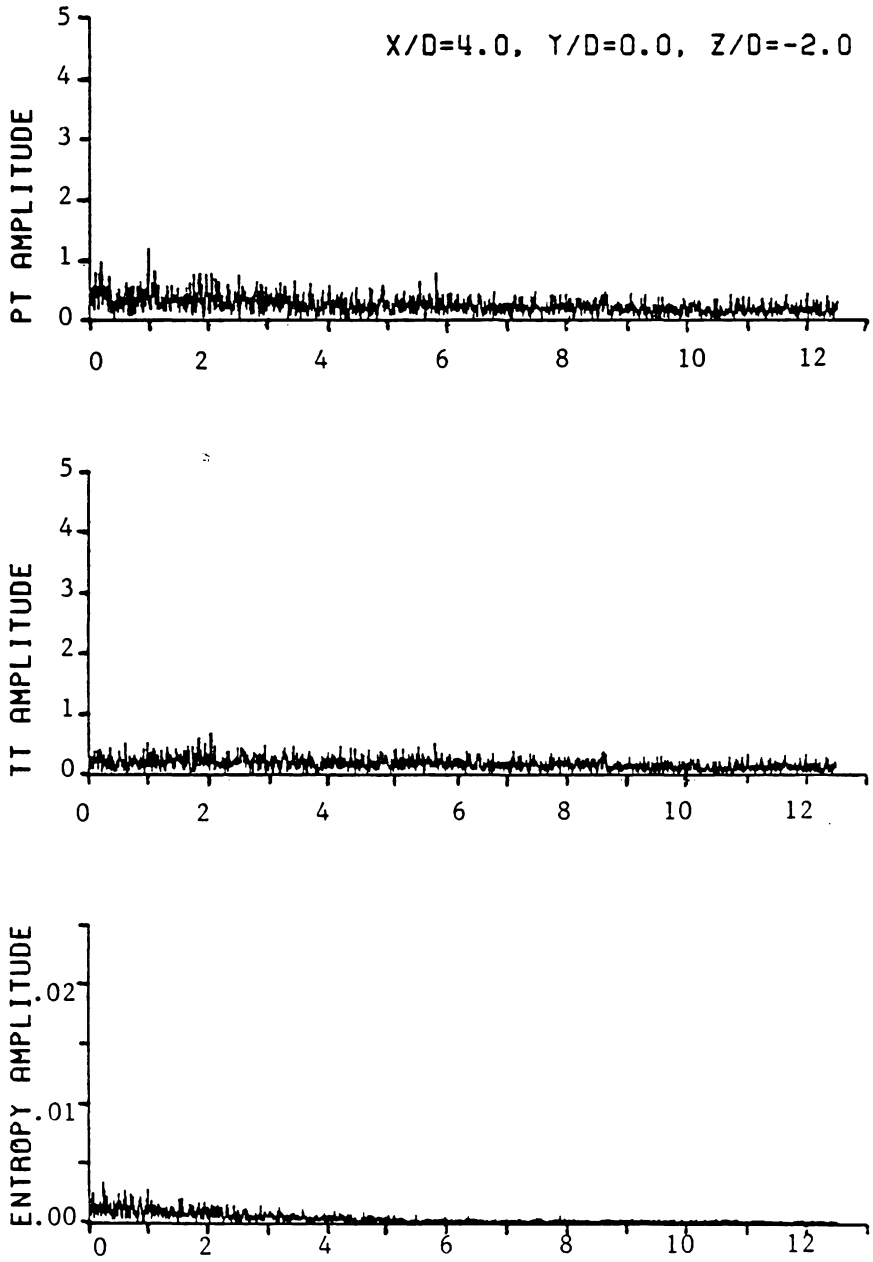

Figure 26c. Time-Resolved Stagnation Pressure, Stagnation Temperature and Entropy at X/D = 4, Y/D = 0.0 and Z/D = -2.0; Shear Flow, Frequency Spectra.

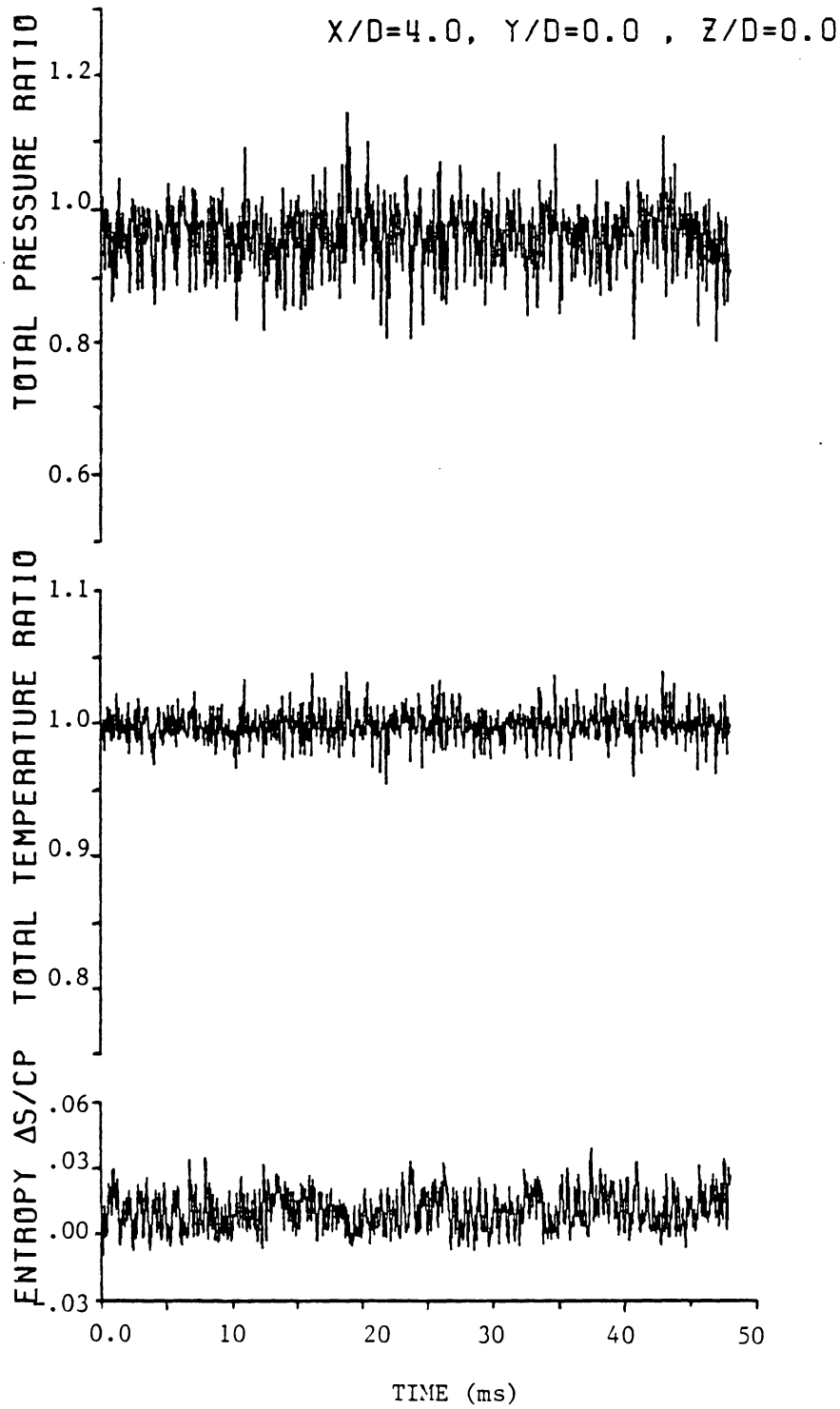

Figure 27a. Time-Resolved Stagnation Pressure, Stagnation Temperature and Entropy at X/D = 4, Y/D = 0.0, and Z/D = 0.0; Shear Flow, Complete Time Trace.

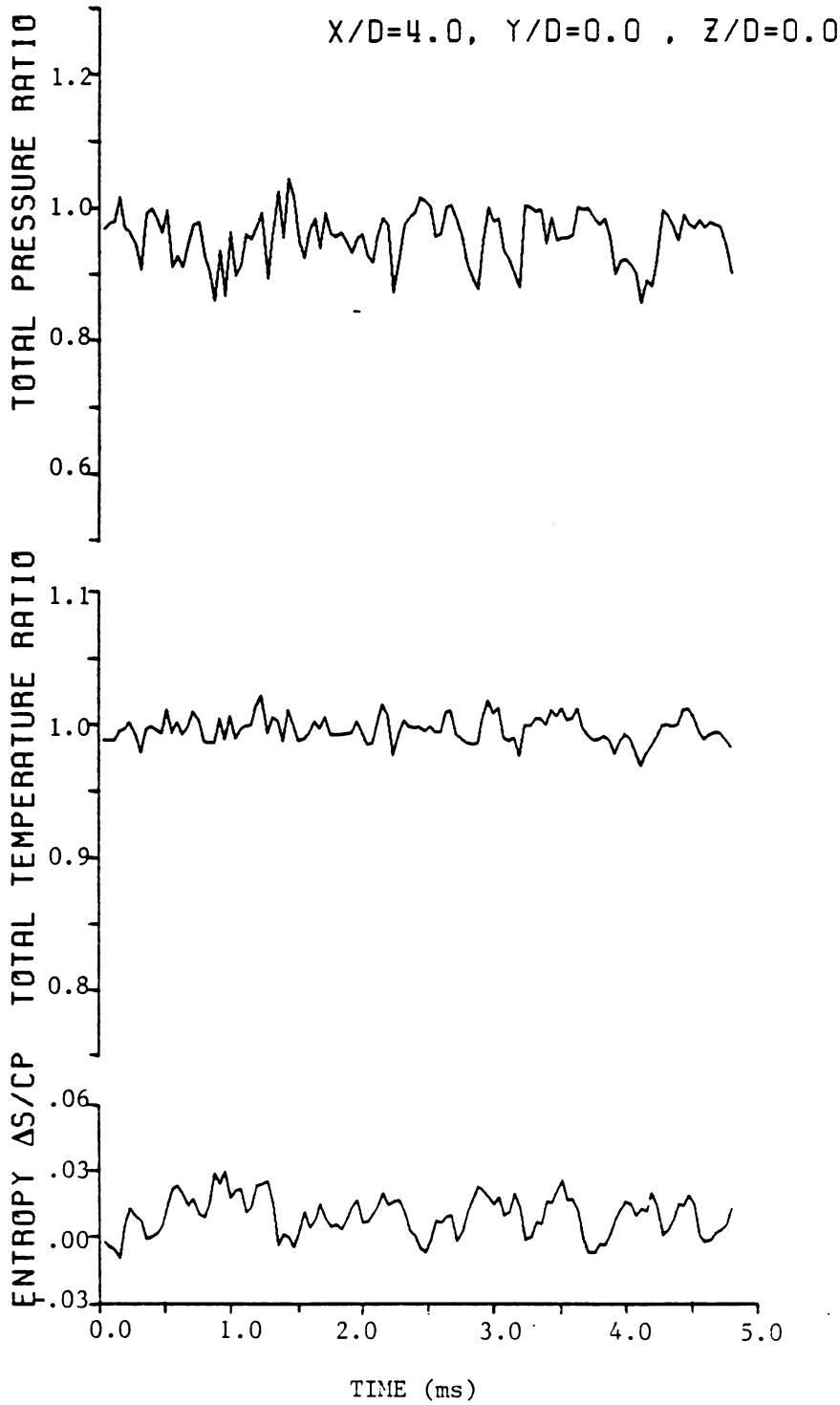

Figure 27b. Time-Resolved Stagnation Pressure, Stagnation Temperature and Entropy at X/D = 4, Y/D = 0.0 and Z/D = 0.0; Shear Flow, Expanded Time Scale.

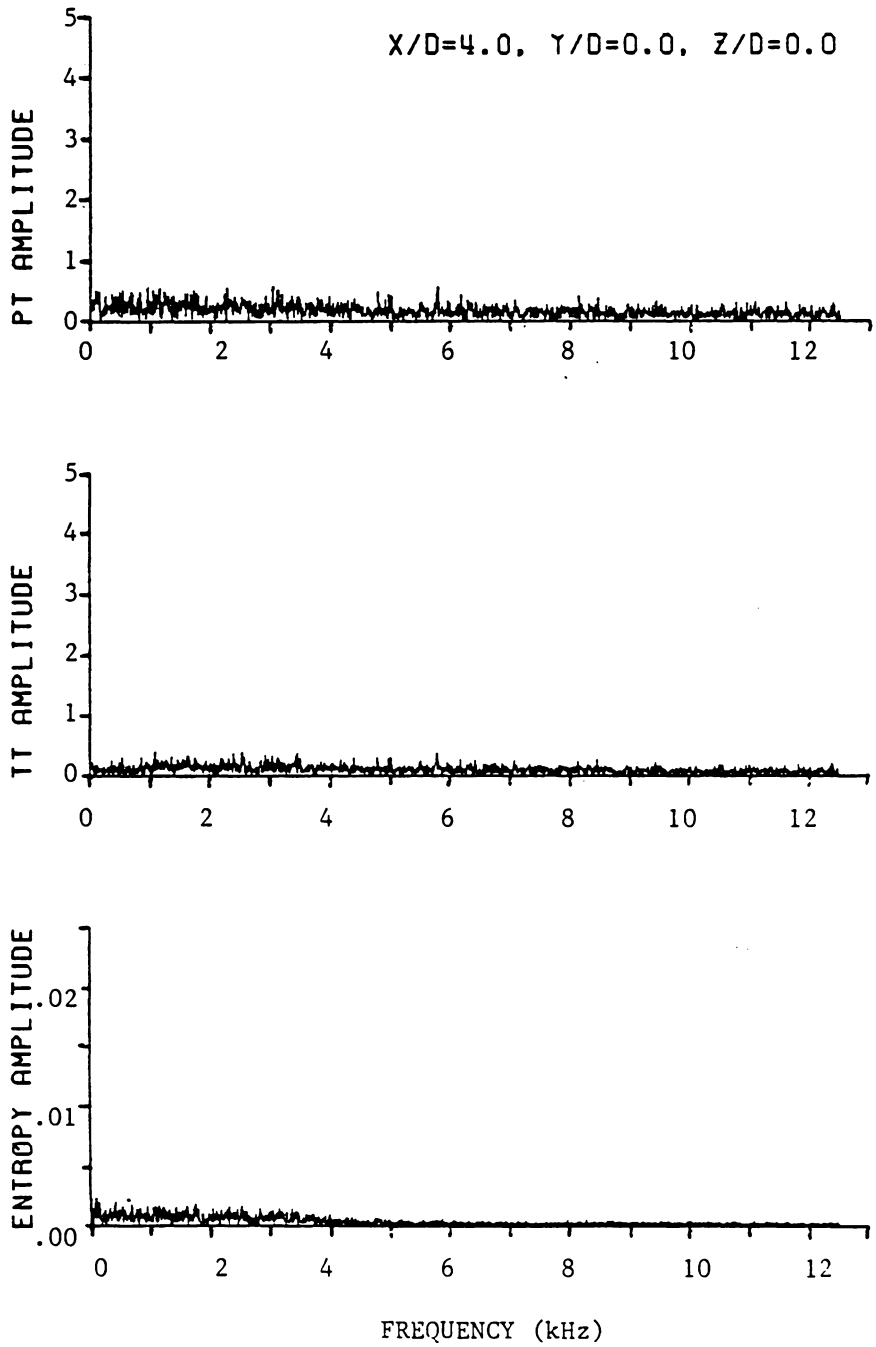

Figure 27c. Time-Resolved Stagnation Pressure, Stagnation Temperature and Entropy at X/D = 4, Y/D = 0.0 and Z/D = 0.0; Shear Flow, Frequency Spectra.

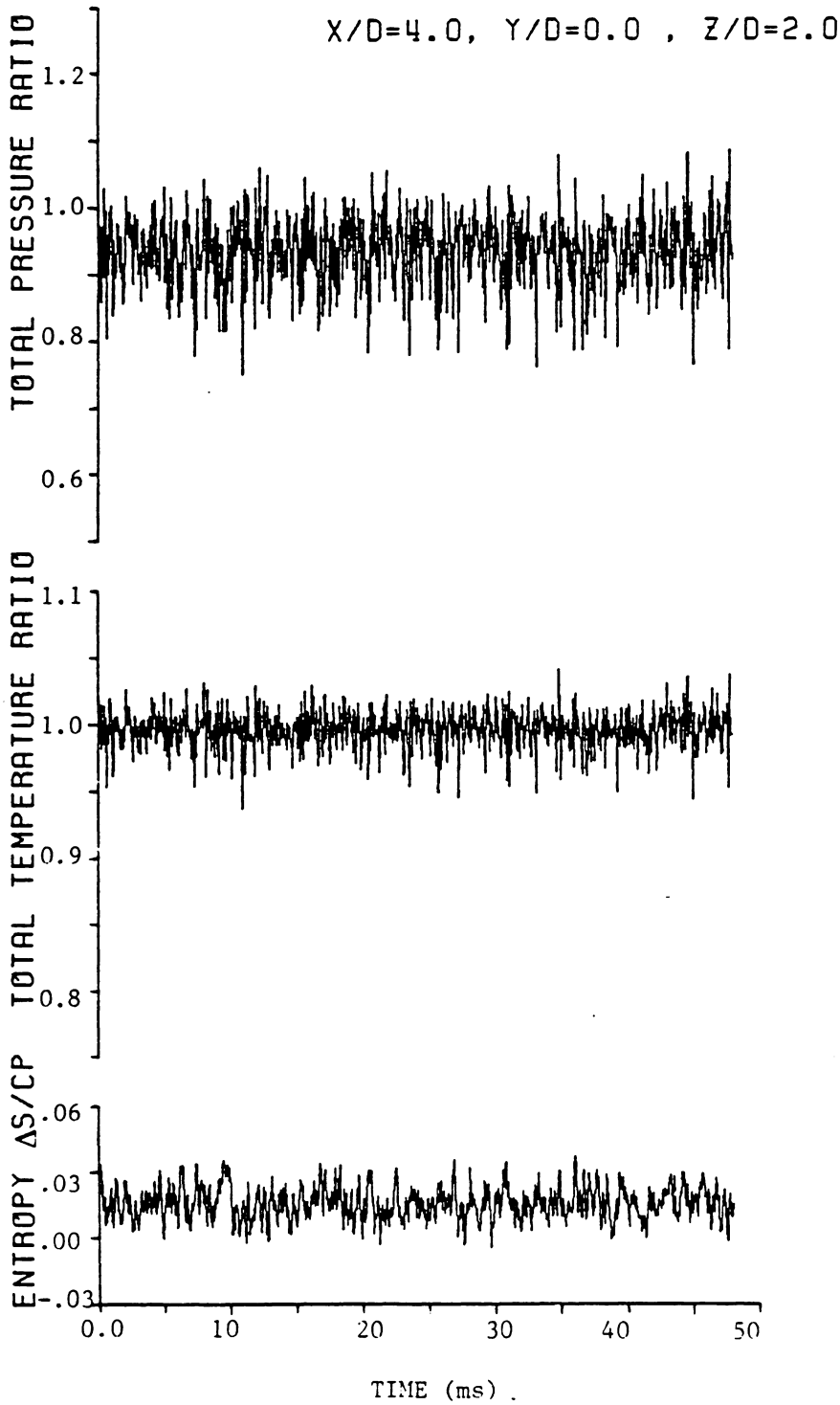

Figure 28a. Time-Resolved Stagnation Pressure, Stagnation Temperature and Entropy at X/D = 4, Y/D = 0.0 and Z/D = 2.0; Shear Flow, Complete Time Trace.

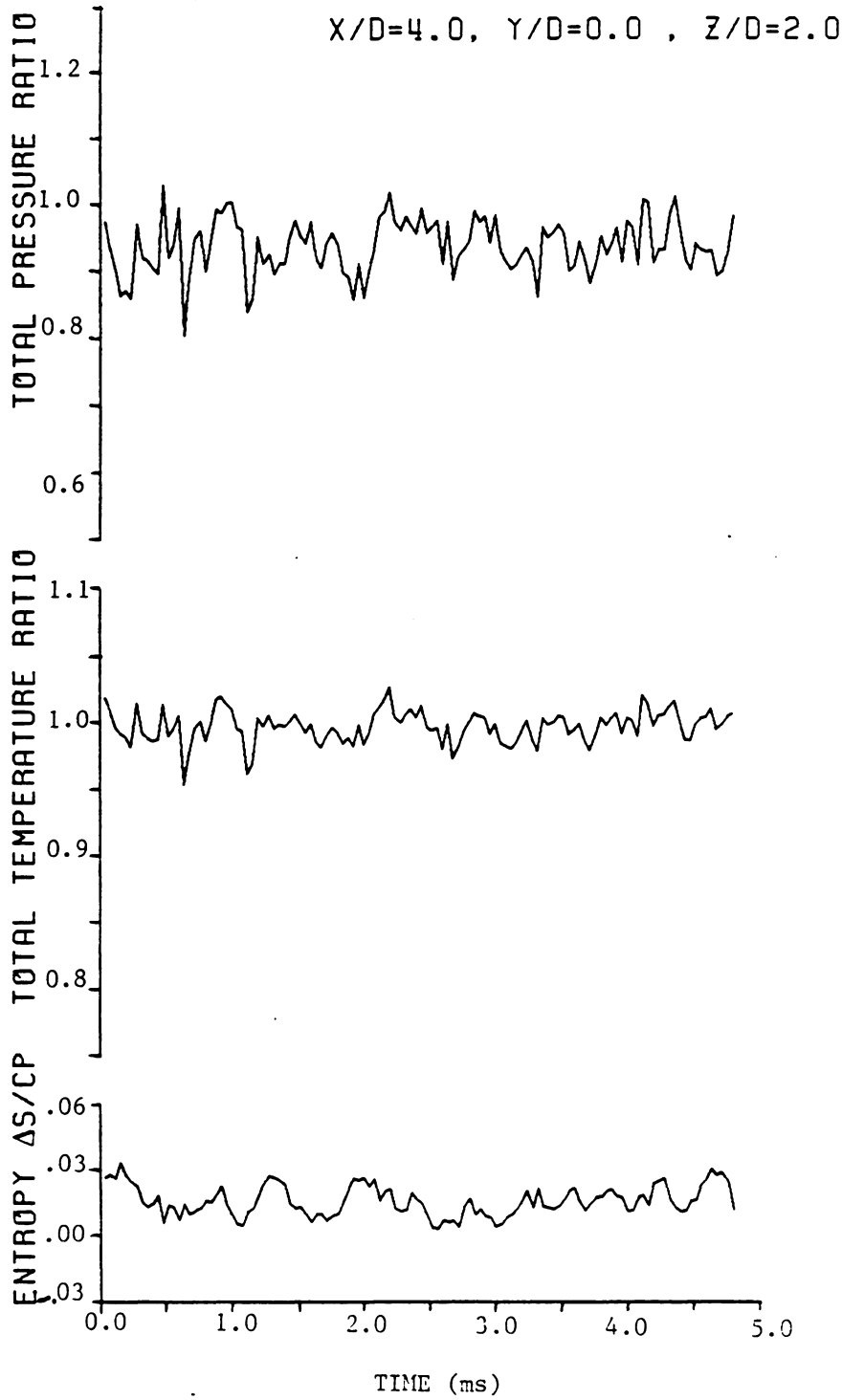

Figure 28b. Time-Resolved Stagnation Pressure, Stagnation Temperature and Entropy at X/D = 4, Y/D = 0.0 and Z/D = 2.0: Shear Flow, Expanded Time Scale.

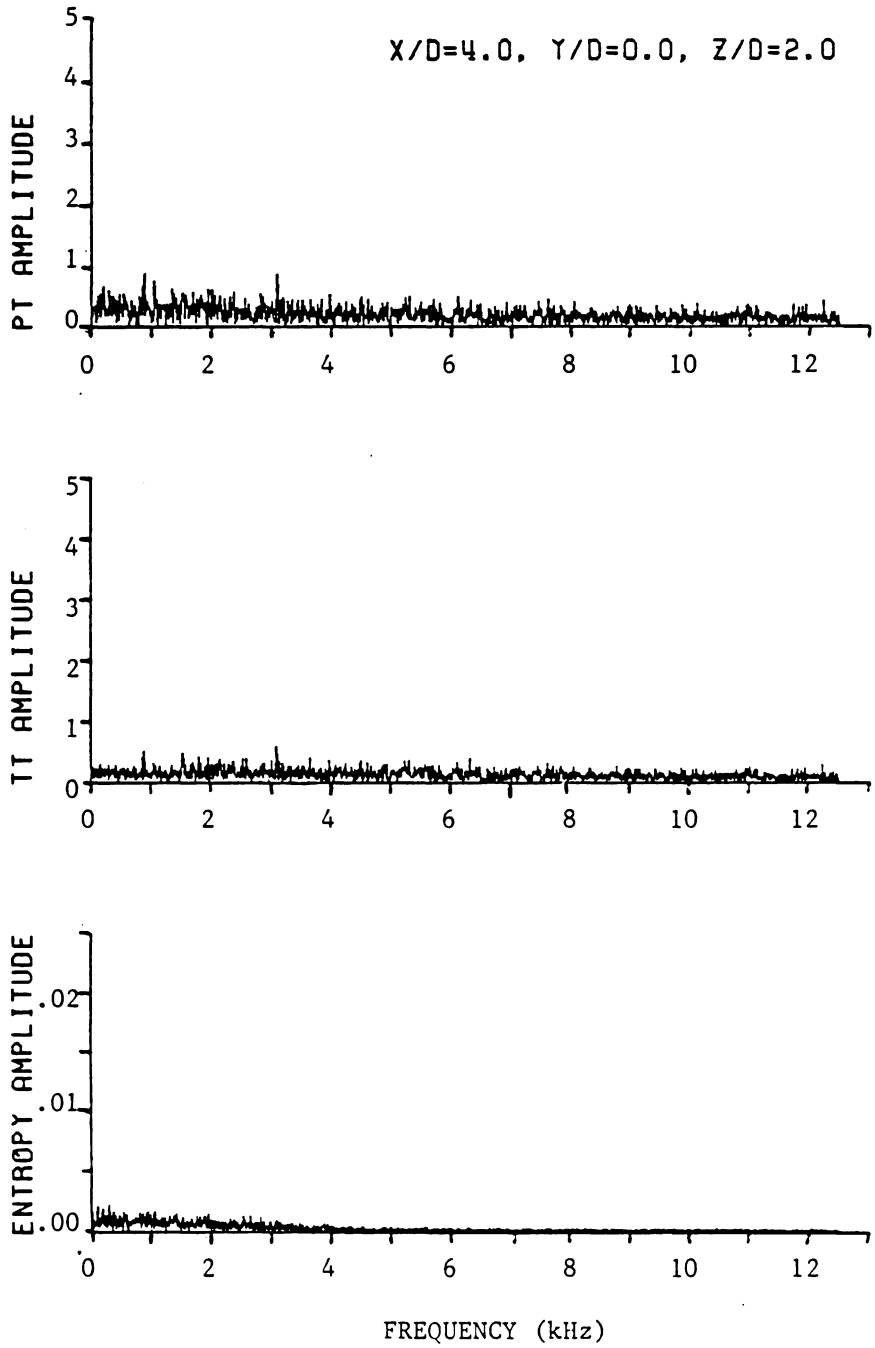

Figure 28c. Time-Resolved Stagnation Pressure, Stagnation Temperature and Entropy at X/D = 4, Y/D = 0.0 and Z/D = 2.0; Shear Flow, Frequency Spectra.

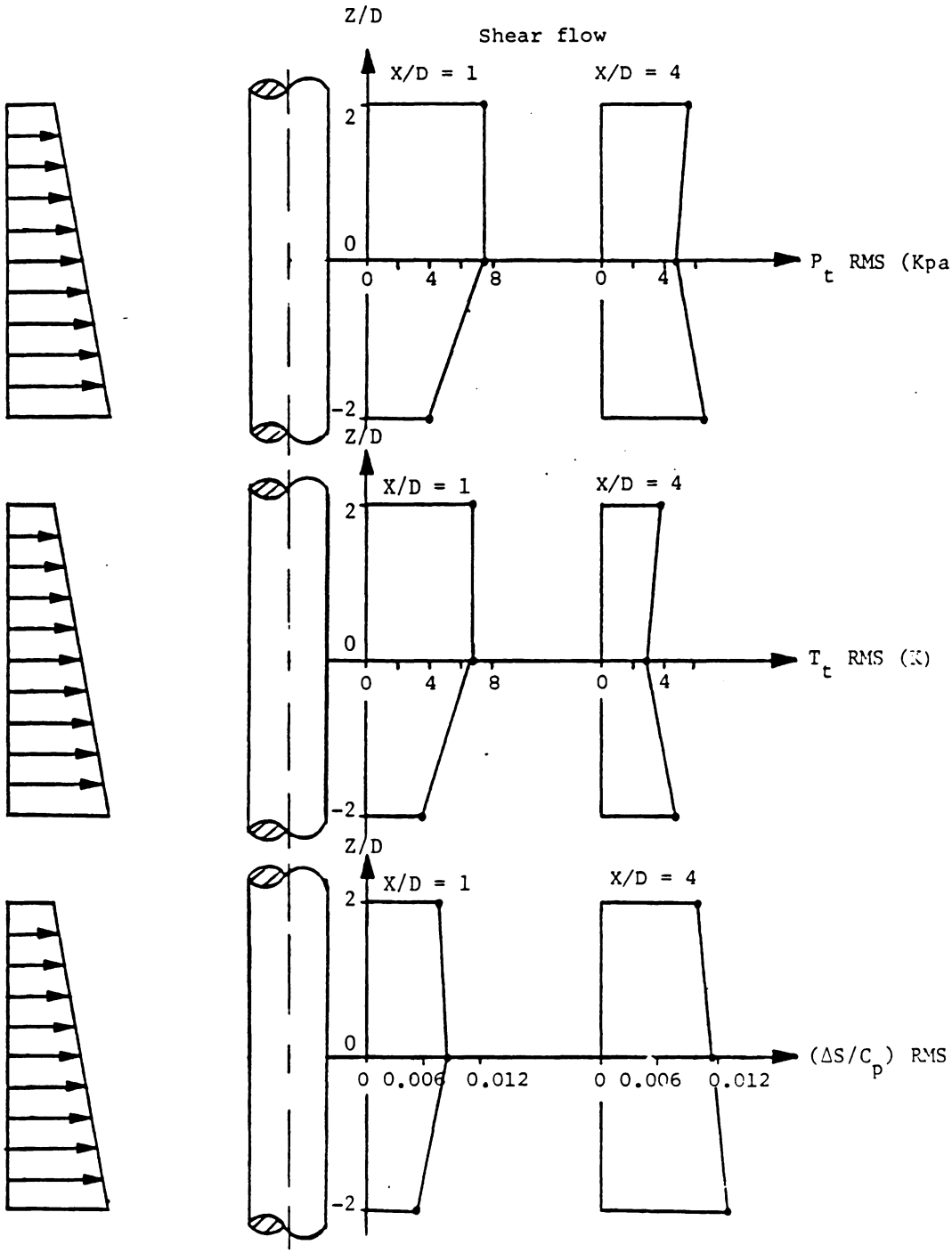

Figure 29. Root-Mean-Square (RMS) Values of the Stagnation Pressure, Stagnation Temperature and Nondimensionalized Entropy ($\Delta S/C_p$) at X/D = 1 and 4; shear flow.

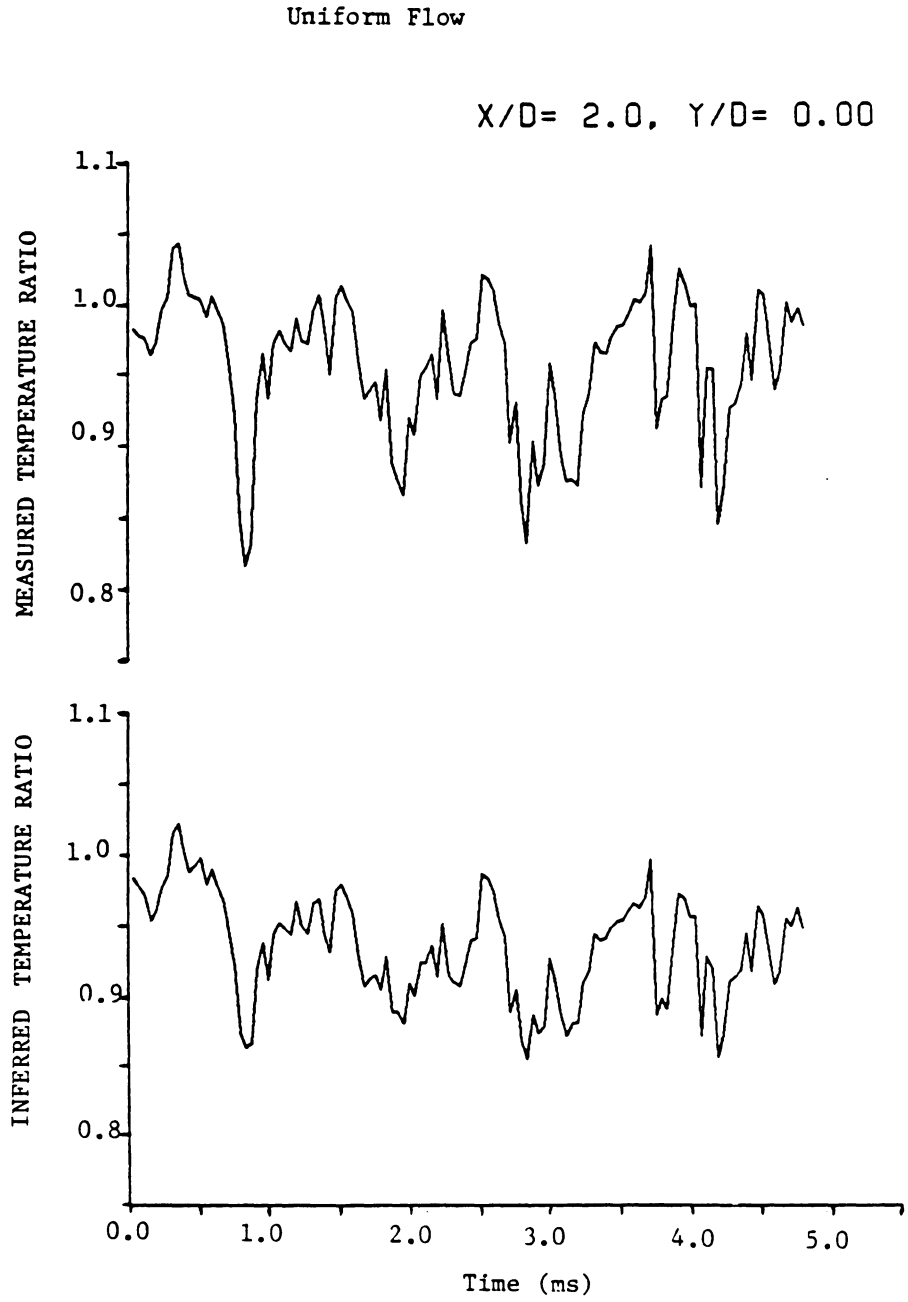

Figure 30. Comparison Between Measured and Inferred Stagnation Temperature ($T_t/T_{t\infty}$) at X/D = 2.0 and Y/D = 0.0.

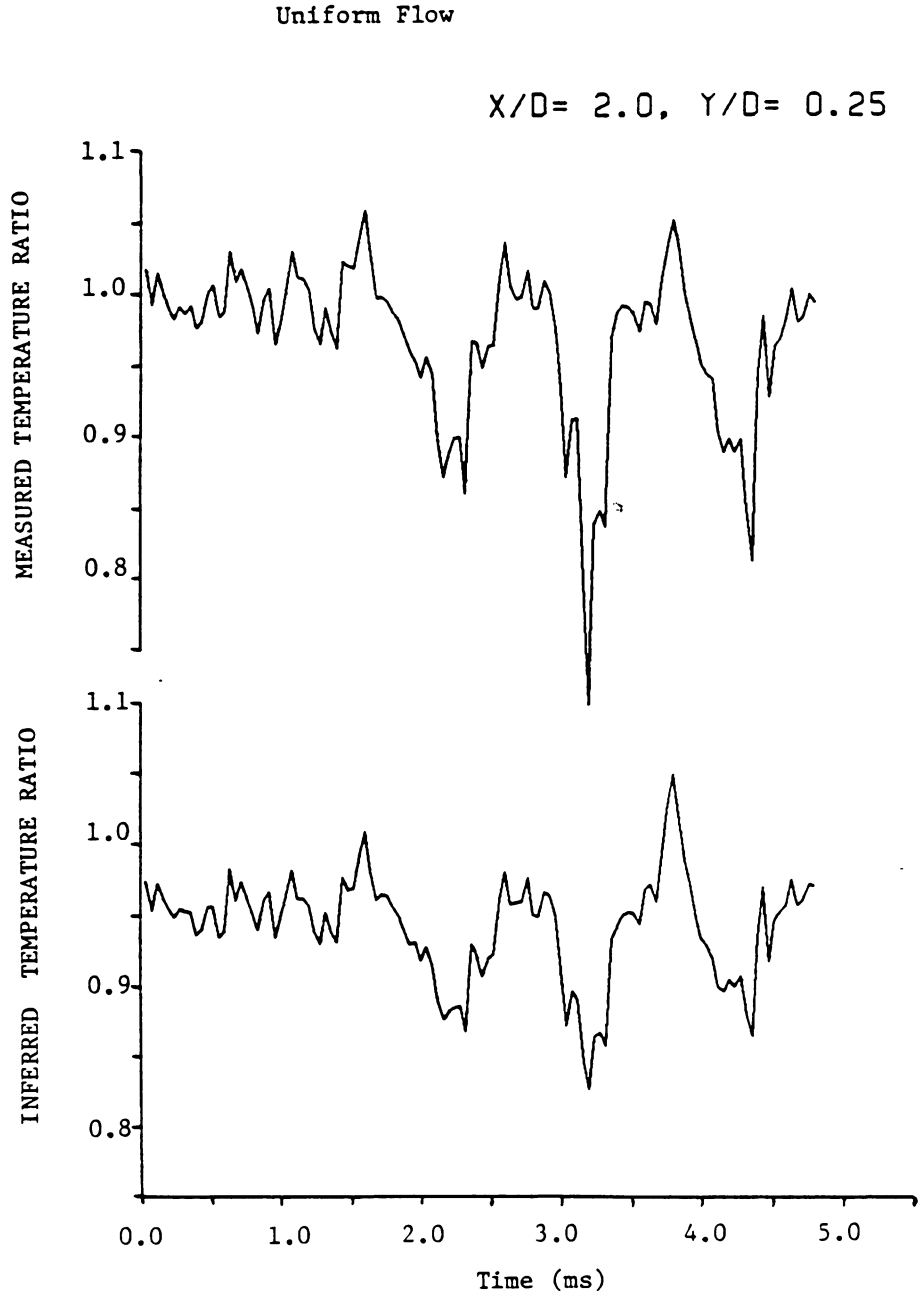

Figure 31. Comparison Between Measured and Inferred Stagnation Temperature ($T_t/T_{t\infty}$) at X/D = 2.0 and Y/D = 0.25.

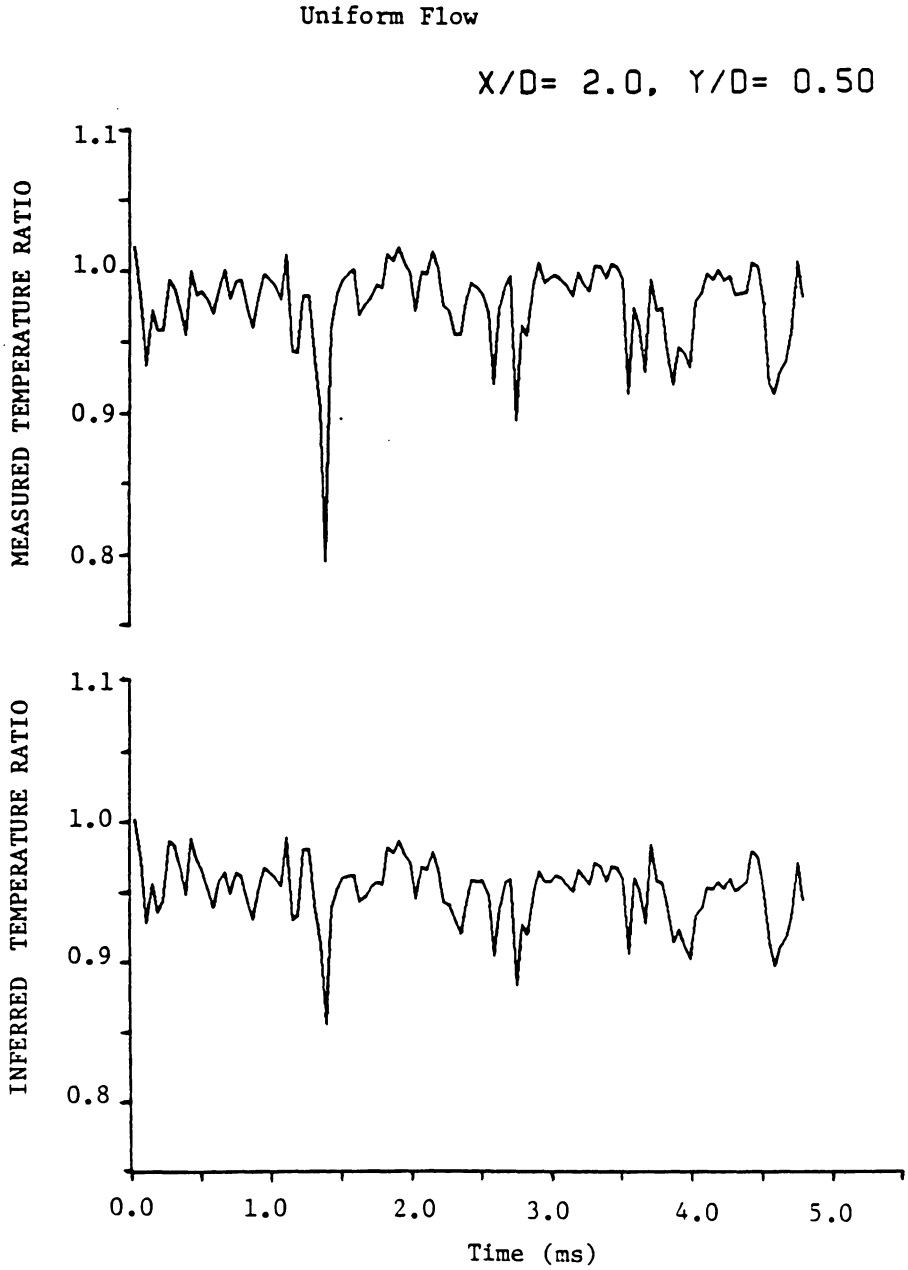

Figure 32. Comparison Between Measured and Inferred Stagnation Temperature ($T_t/T_{t\infty}$) at X/D = 2.0 and Y/D = 0.5.

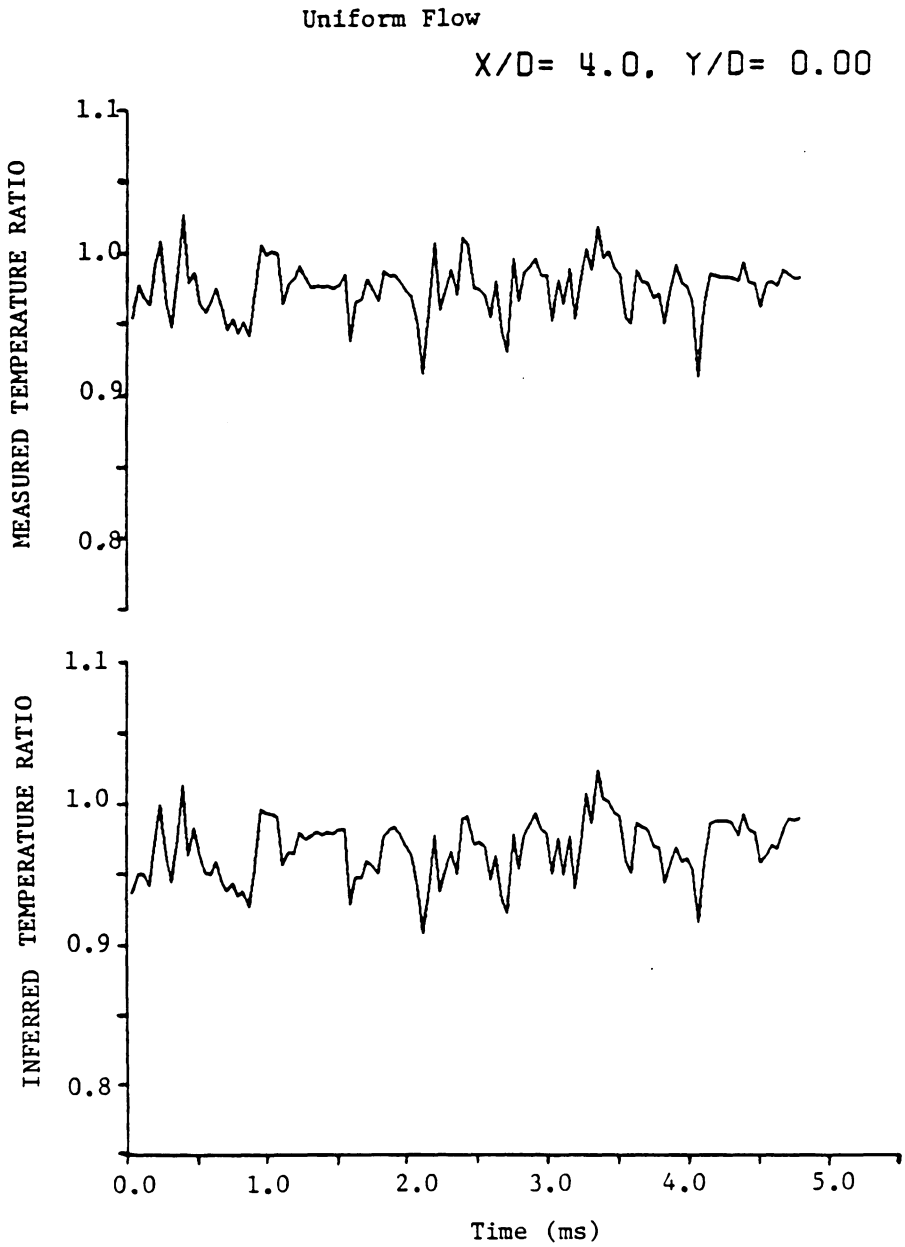

Figure 33. Comparison Between Measured and Inferred Stagnation Temperature ($T_t/T_{t\infty}$) at X/D = 4.0 and Y/D = 0.0.

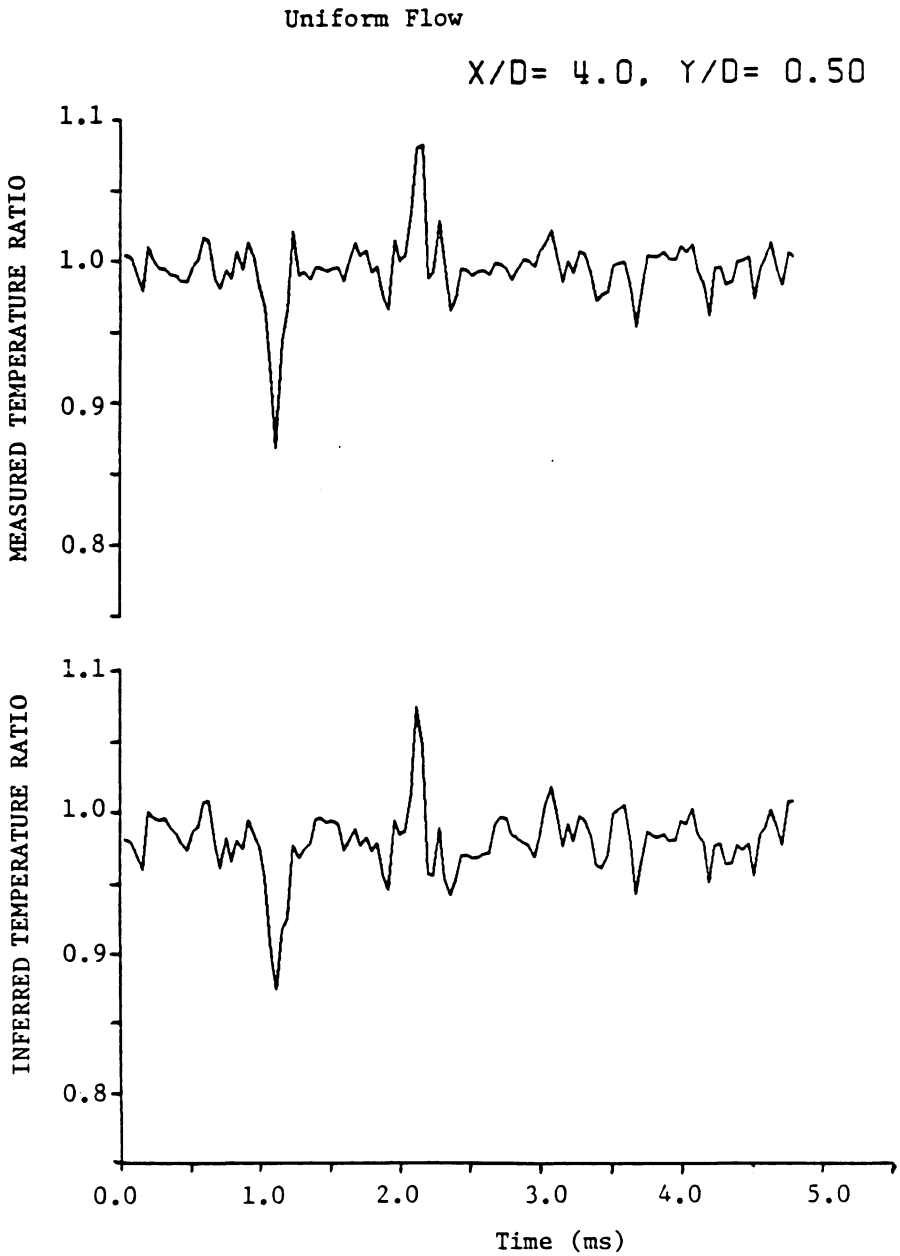

Figure 34. Comparison Between Measured and Inferred Stagnation Temperature ($T_t/T_{t\infty}$) at X/D = 4.0 and Y/D = 0.5.

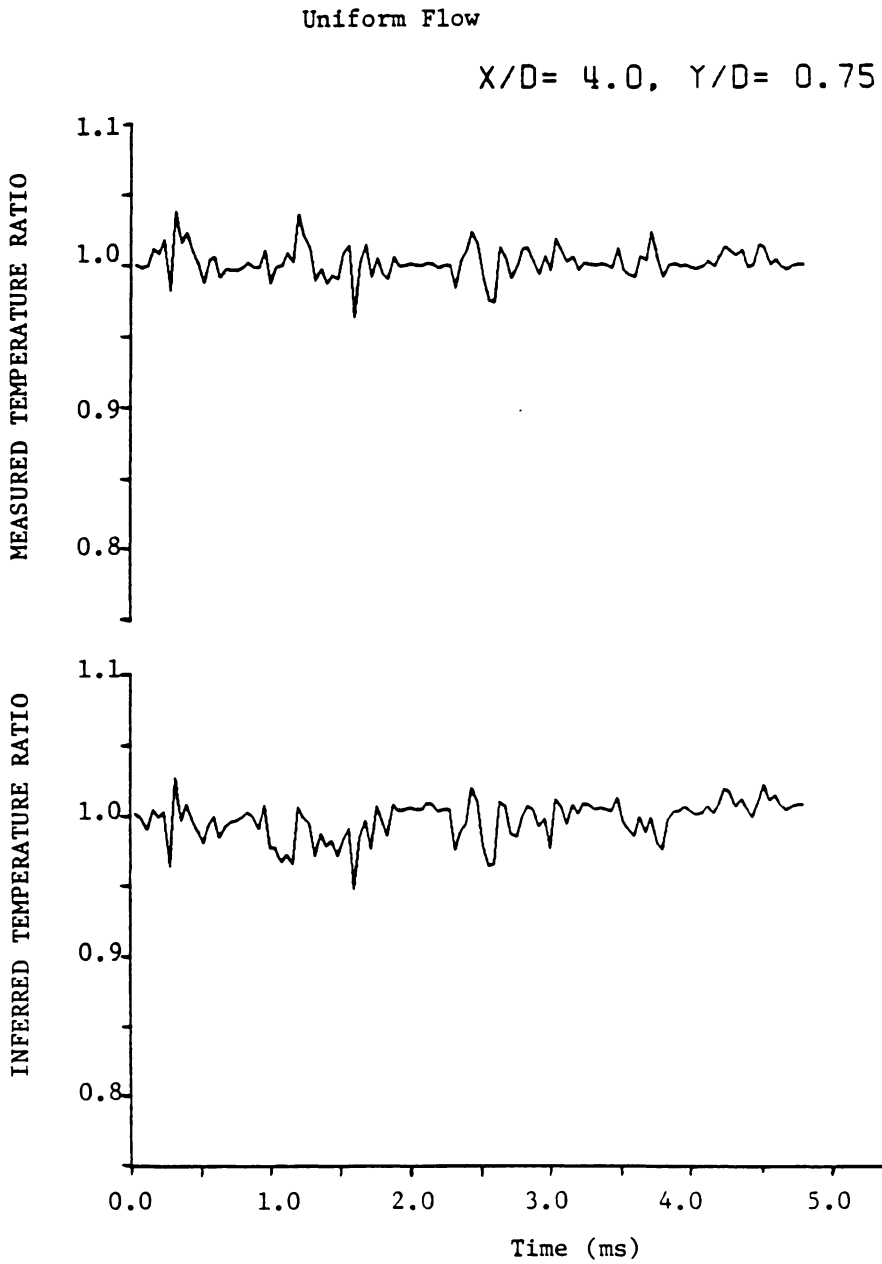

Figure 35. Comparison Between Measured and Inferred Stagnation Temperature ($T_t/T_{t\infty}$) at X/D = 4.0 and Y/D = 0.75.

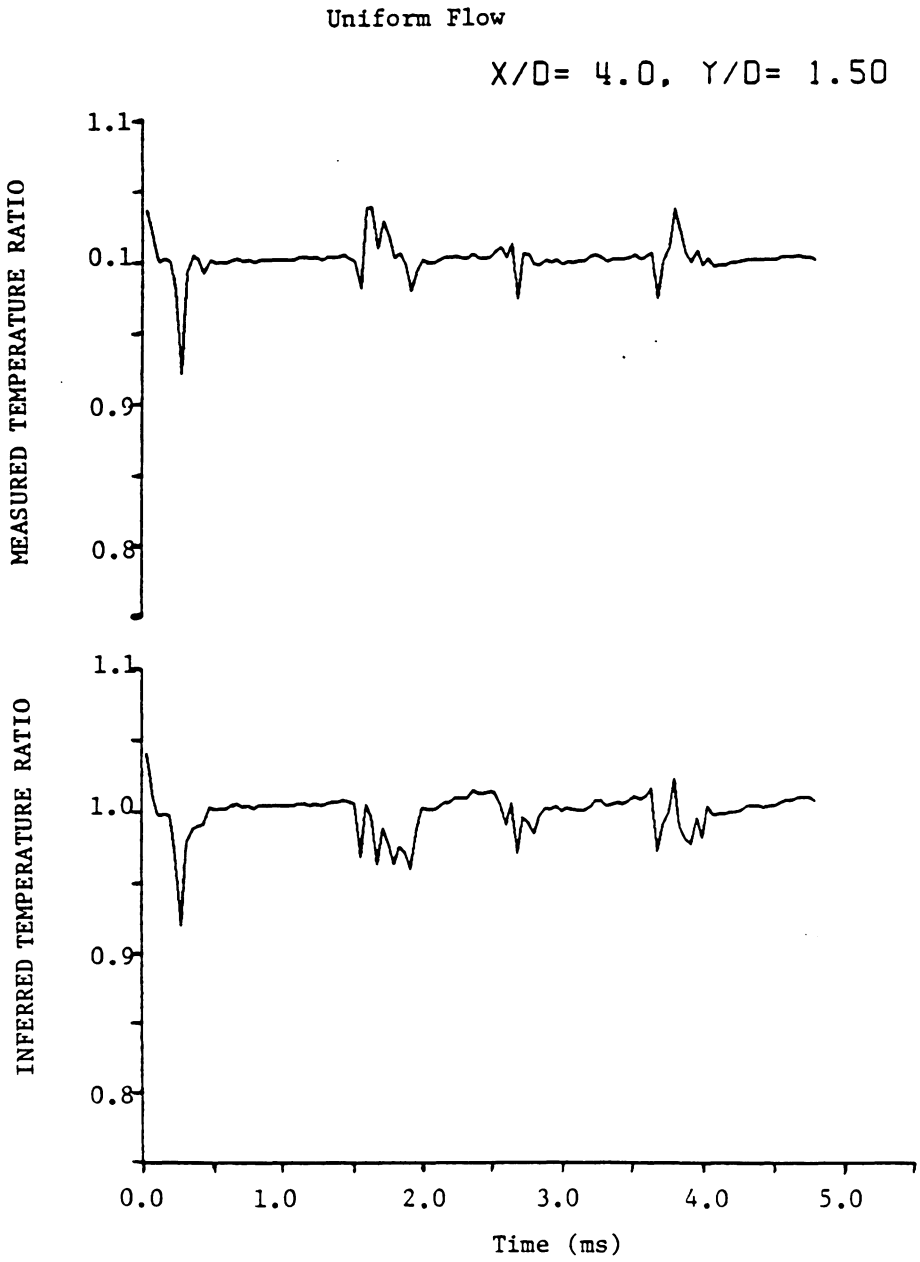

Figure 36. Comparison Between Measured and Inferred Stagnation Temperature ($T_t/T_{t\infty}$) at X/D = 4.0 and Y/D = 1.5.

The vita has been removed from the scanned document